Appearance Changes
due to
Light Exposure

by

Bradley W. Kimmel

A thesis

presented to the University of Waterloo

in fulfillment of the

thesis requirement for the degree of

Doctor of Philosophy

in

Computer Science

Waterloo, Ontario, Canada, 2017

I hereby declare that I am the sole author of this thesis. This is a true copy of the thesis, including any required final revisions, as accepted by my examiners.

I understand that my thesis may be made electronically available to the public.

Abstract

The fading of materials due to light exposure over time is a major contributor to the overall aged appearance of man-made objects. Although much attention has been devoted to the modeling of aging and weathering phenomena over the last decade, comparatively little attention has been paid to fading effects. In this dissertation, we present a theoretical framework for the physically-based simulation of time-dependent spectral changes induced by absorbed radiation. This framework relies on the general volumetric radiative transfer theory, and it employs a physicochemical approach to account for variations in the absorptive properties of colourants. Employing this framework, a layered fading model that can be readily integrated into existing rendering systems is developed using the Kubelka-Munk theory. We evaluate its correctness through comparisons of measured and simulated fading results. Challenges in the acquisition of reliable measurements are discussed. The performance characteristics of the proposed model are analysed, and techniques for improving the runtime cost are outlined. Finally, we demonstrate the effectiveness of this model through renderings depicting typical fading scenarios.

Acknowledgements

I would like to thank my advisor, Prof. Gladimir Baranoski, for his encouragement throughout my graduate career. I also thank committee members, Prof. Peter Forsyth and Prof. Paulo Alencar, for their input during the course of this research, as well as Prof. Pierre Poulin and Prof. Sander Rhebergen for their valuable feedback.

Special thanks also go to Tenn Francis Chen, Erik Miranda, and Daniel Yim for their contributions to the ACM Transactions on Graphics paper which constitutes a key part of this research. I would also like to thank all of my colleagues from the Natural Phenomena Simulation Group for their helpful insights.

I am grateful to Prof. Ellsworth LeDrew of the Department of Geography, University of Waterloo, for his support and for lending us the spectrophotometer used for early experiments as part of this work.

I am also grateful to my parents, Bill and Gail, for their support in this endeavour, and to my daughter, Alexa, who inspires me to keep going. Finally, I would like to thank my wife, Erin, and for her immeasurable love and ongoing support, without which this would not have been possible.

Table of Contents

List of Tables

List of Figures

xiii

List of Symbols

xvii

Chapter 1

Introduction

Computer generated images usually depict settings devoid of signs of wear and tear. The appearance of real-world materials, however, varies over time due to a myriad of aging and weathering phenomena. Arguably light exposure is among the main environmental factors responsible for such time-dependent variations. A few examples of material appearance changes caused by light exposure are depicted in Figure 1.1. For instance, a corkboard or stained wood flooring may fade in areas where it is exposed to sunlight from a nearby window. This fading may be lacking in areas that were once covered with photographs or posters. A painting on a wall may lose some of its colours after being excessively exposed to light, with some colours fading more readily than others. Accounting for these effects provides the viewer with important visual cues, significantly improving the perceived realism of a given scene.

In this dissertation, we introduce a novel theoretical framework for the analysis and simulation of material appearance changes over time due to light exposure. This framework is based on the general formulation for light transport within a medium [3]. It employs a physicochemical approach that accounts for the kinetics of pigment and dye fading processes as well as variations in exposure level with depth in samples of arbitrary thickness. We describe in detail the application of this framework using the Kubelka-Munk (K-M) theory [63], and evaluate its fidelity through comparisons of measured and simulated reflectance curves resulting from different periods of fading. We

1

also illustrate the effectiveness of the model derived from this framework through the rendering of scenes depicting material appearance changes over time.

Besides the contribution to realistic image synthesis, the physically-based simulation of fading effects described here has also important cultural and industrial applications. For example, museums are interested in the long term effects of light exposure on their art collections [47, 91]. Hence, a compromise must be reached that minimizes damage caused by light exposure, while still allowing enough light for public viewing. In this context, damage caused by visible light is of primary concern, as ultraviolet light may usually be filtered out without affecting viewing by means of a glass case. By taking a physicochemical approach, the proposed framework is able to simulate the fading of objects under experimental and hypothetical conditions. This would allow a conservator to evaluate the use of various filters, coverings, illumination conditions and lighting policies. In the multi-billion dollar manufacturing sector, one is interested in extending the life of surface finishes such as paints and stains [44]. Accordingly, in recent years, substantial research efforts [67] have been directed toward this goal. Viewed in this context, a framework for simulating the long term effects of light exposure can be used by industry researchers to determine how various additives or varnishes affect the lightfastness of surface finishes, *i.e.*, their resistance to alterations due to light exposure. These investigations, in turn, would allow for the manufacturing of products that can maintain their original colours for longer periods of time.

1.1 Summary of Original Contributions

In this dissertation, we endeavor to demonstrate that:

> *Introducing* time *into the traditional rendering equation provides a framework which enables the development of computational techniques aimed at simulating the effects of light exposure on material appearance.*

In support of this, the contributions of this work are as follows.

1. **A theoretical framework for the physically-based simulation of time-dependent spectral appearance changes induced by absorbed radiation.**

   We explore the ramifications of adding time to each of the components of the general volumetric rendering equation. Furthermore, we provide analyses specifically for the cases of single-flux and dual-flux light transport environments.

2. **The first model for simulating the effects of light exposure on spectral appearance over time [60].**

   As we shall see, even for these restricted light transport environments, the corresponding systems of equations will not be amenable to analytic solution. We develop numerical techniques for simulating the effects of light exposure on spectral appearance characteristics over extended periods of time. These techniques are evaluated through comparisons with measured fading rates for several material samples. We also provide an analysis of the performance characteristics of the proposed techniques as key parameters are varied [61].

3. **Measurements of the effects of light exposure on the spectral appearance characteristics of a particular selection of materials over time, along with an account of the challenges involved in acquiring reliable measurements with limited resources.**

   The progression of spectral reflectance curves are provided for several specimens exposed to an extended period of light exposure. Such data is not readily available in the literature. We describe the procedures and equipment employed in preparing these specimens, illuminating them over the duration of the experiment, and in measuring their spectral reflectance curves at set times during the course of exposure We outline the challenges involved in obtaining these measurements given the constrained set of resources at our disposal, and discuss the techniques we used to overcome these challenges.

1.2 Document Organization

The remainder of this document is organized as follows.

Chapter 2 provides the relevant background that serves as the foundation for the material presented in this dissertation. We first outline the main objectives of computer graphics. This involves generating representative images of a scene, given an accurate description of the geometry and materials comprising the environment. We discuss the nature of light and provide an overview of the relevant optical processes that contribute to the distribution of light in an environment. This includes emission, which adds light to the environment; absorption, which removes light from the environment; and scattering which redistributes light within the environment. We then outline how these processes are accounted for within computer graphics in order to render a particular scene. This may be partitioned into the simulation of global illumination and of local illumination. The former refers to simulating the distribution of light throughout the entire scene. The latter relates to the interactions of light with particular materials in the environment, which is described by the *measurement of appearance*. We discuss the importance of predictive simulation in all aspects of the rendering pipeline.

Chapter 3 reviews the literature related to the topics discussed in this dissertation. Aging phenomena, such as fading and yellowing, resulting from exposure to light over an extended periods of time, is the main focus of this research. We therefore begin by providing an overview of the state of the art with regard to the simulation of the broader class of aging and weathering phenomena in computer graphics. This includes methods developed at simulating particular processes, such as the formation of metallic patinas, as well as data-driven techniques aimed at reproducing a wider range of aging effects. Next, we review investigations into lightfastness of materials in the conservation literature, as well as methods aimed at digital restoration of faded artwork. We provide an overview of other uses of various techniques used throughout this work.

Chapter 4 introduces the theoretical framework for describing light-induced changes in material

appearance. The framework employs the volumetric radiative transfer equations as its basis. Time is introduced as a parameter. The resulting system accounts for the photochemical kinetics of pigment and dye fading processes. Based on this framework, a two-flux model is developed based on Kubelka-Munk theory.

Chapter 5 presents numerical algorithms suitable for simulating the effect of light exposure on material appearance. Models, such as the two-flux model developed in the previous chapter, derived from the temporal-volumetric radiative transfer framework often do not admit analytical solutions. It is therefore necessary to resort to numerical techniques for solving the resulting systems of equations. We describe these techniques in this chapter. This involves discretization of the problem in the temporal and spatial domains. The solution is then computed alternately in each domain.

Chapter 6 describes the procedures used to evaluate the effectiveness of the proposed algorithms. We conducted several sets of experiments in which we subjected various materials to light exposure over an extended period of time. The materials employed include newsprint, cork, and two dyes. Reflectance measurements were taken prior to exposure, and after several periods of exposure throughout the process.

Chapter 7 discusses the challenges involved in obtaining accurate measurements of the effects of light exposure on material appearance over an extended period of time.

Chapter 8 evaluates the predictive capability of the proposed algorithms. Results are presented depicting comparisons between simulations employing the numerical algorithms to measurements obtained using the procedures outlined in the previous chapter. We also assess the phenomenological characteristics of the proposed framework, drawing comparisons with accounts from the conservation literature. Finally, we demonstrate the applicability of the proposed techniques to computer graphics through several rendered scenes depicting the fading and yellowing of materials before and after extended periods of light exposure.

Chapter 9 discusses the performance characteristics of the algorithms presented in the preceding chapters. We analyse the influence of key parameters, including the number of layers and time steps, on the accuracy and run-time cost of the proposed techniques. The run-time, and the resulting spectral reflectance and colour characteristics resulting from the simulation obtained while varying these key parameters are compared with the results yielded by a reference simulation employing a large number of layers and time steps. Practical solutions are proposed allowing for the simulation of material appearance changes due to light exposure where higher performance is required.

Chapter 10 concludes the main body of this dissertation. Here, we summarize the contributions and discuss the limitations of this work. We also outline potential avenues for future research.

Finally, some additional details and data pertaining to the evaluation procedures used in this research are included in appendices following the main body of this work.

Appendix A describes how to estimate the absorption and scattering properties of a homogeneous medium from measurements of its reflectance over black and over white substrates.

Appendix B provides the data employed in our simulations in tabulated form. This includes the spectral irradiance of the illuminants used and the absorption and scattering characteristics of the materials.

Figure 1.1: Photographs depicting common materials subjected to fading due to light exposure. *Top Left*: An area rug has faded everywhere except where a couch had been placed. *Top Right*: A newspaper has turned yellow from many years of light exposure. *Middle*: Printed materials have been added and removed from a bulletin board over time, resulting in an irregular fading pattern. *Bottom*: Wood flooring darkened from light exposure except where covered by a rug.
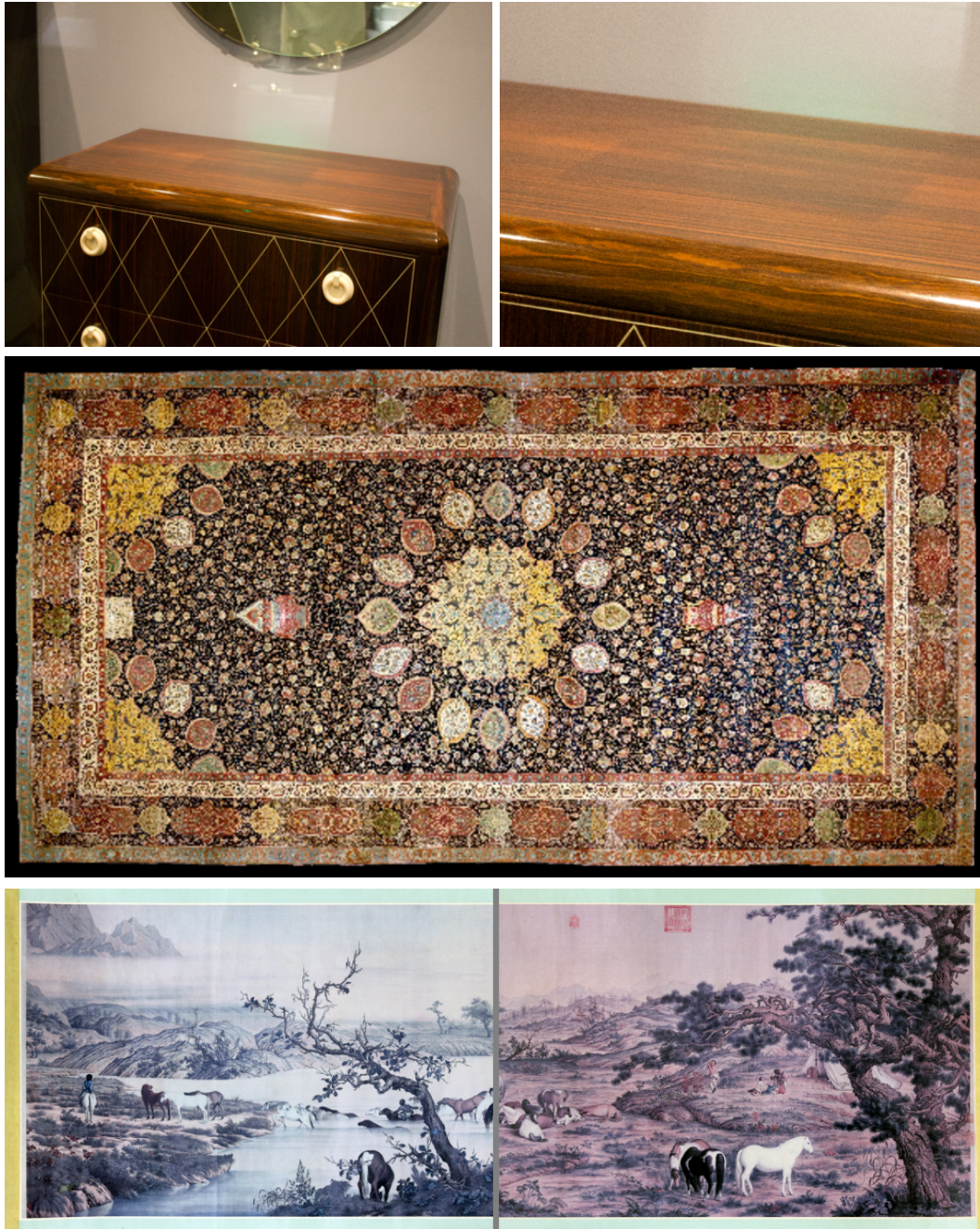
Figure 1.2: Photographs depicting artistic objects subjected to appearance changes induced by extended periods of light exposure. *Top*: The surface of an art nouveau table (c. 1900, on exhibit at the Royal Ontario Museum) has faded except where a lamp stood. *Middle*: A carpet that has faded due to many years of light exposure (on exhibit at the Victoria and Albert Museum). *Bottom*: The left end of a mural has been exposed to more light than the right, yielding uneven fading along its length. Photographs of the two ends are shown adjacent to one another so that the difference is clearly visible.

Chapter 2

Background

In this chapter, we provide the relevant background that serves as the foundation for the material presented in the remainder of this dissertation. Its contents are organized as follows. In Section 2.1, we outline the main objectives of computer graphics. This involves generating representative images of a scene, given an accurate description of the geometry and materials comprising the environment. In Section 2.2, we discuss the nature of light as an electromagnetic wave. In Section 2.3, we provide an overview of the relevant optical processes that contribute to the distribution of light in an environment. This includes emission, which adds light to the environment; absorption, which removes light from the environment; and scattering which redistributes light within the environment. In Section 2.4, we then outline how these processes are accounted for within computer graphics in order to render a particular scene. This process is governed by the *rendering equation*, which is discussed in Section 2.5. Rendering algorithms may be partitioned into the simulation of local illumination and of global illumination. These are discussed in Sections 2.7 and 2.8, respectively. The former relates to the interactions of light with particular materials in the environment, which is described by the *measurement of appearance*. The latter refers to simulating the distribution of light throughout the entire scene. In Section 2.9, we outline how radiometric quantities generated from the rendering equation are converted into colour. This involves modeling the human visual system. In Section 2.10, we discuss the importance of predictive simulation in all aspects of the rendering

pipeline.

2.1 Overview

One of the main objectives in computer graphics is the production of photorealistic images. This involves generating a two dimensional image from a model of a three dimensional scene. The scene is described by:

- the position and orientation of the *camera* within the scene,

- the *geometry* of the objects within the scene,

- the *materials* that describe the appearance (reflectance, glossiness, etc.) of objects within the scene,

- optionally, the *participating media* that describes how light interacts with the volume between objects within the scene.

The goal is to produce a rectangular array of colours (pixels) that represent the scene from the perspective of the camera. Here, the term *colour* is used in an abstract sense. This may be represented in terms of red, green, and blue quantities (RGB), or some other colour space. Alternatively, the pixels may be represented by a spectral power distribution.

2.2 Electromagnetic Spectrum

Light is an electromagnetic wave. As such, wavelength (or its reciprocal, frequency) is a fundamental property of light. The entire electromagnetic spectrum encompasses gamma rays, X-rays, etc., on the short wavelength (high frequency) end to microwaves and radio waves on the long wavelength (low frequency) end, as depicted in Figure 2.1. Human beings are only capable of seeing a small portion of the total electromagnetic spectrum, ranging in wavelength from approximately
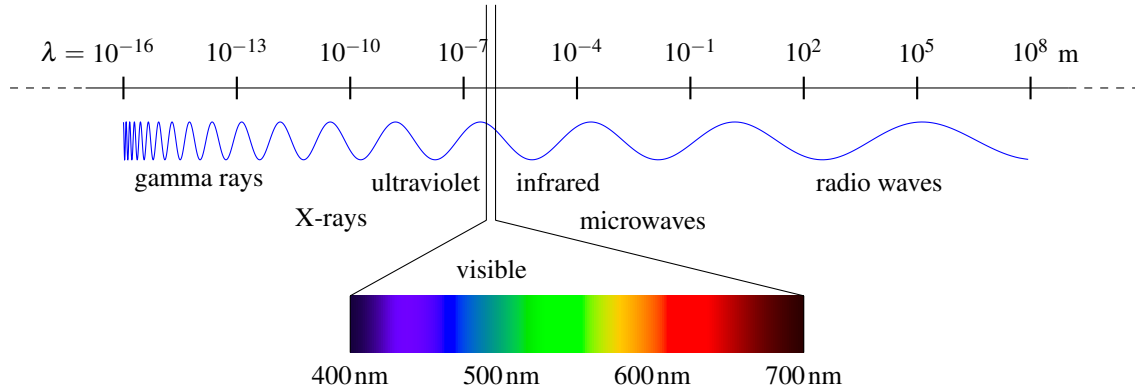
Figure 2.1: The electromagnetic spectrum ranges from gamma rays and X-rays on the short-wavelength range to microwaves and radio waves at the long-wavelength end. Human beings are only capable of seeing light falling within a narrow range from approximately 400 to 700 nm.

400 to 700 nm. Other regions of the electromagnetic spectrum, in particular the ultraviolet region (approximately 200 to 400 nm), may have a significant influence on material appearance over time.

2.2.1   Nature of Light

Light has a dual nature: it may be viewed as consisting of a stream of particles called photons, or as an electromagnetic wave. Which form best describes a particular phenomenon depends on the experimental conditions [24]. Typically, however, when the sizes of the objects that light is interacting with, and of their surface details, are large relative to the wavelength of the light, the particle nature of light dominates. Within this dissertation, we primarily make use of the particle nature of light. However, certain quantities, such as wavelength and spectral distribution, are drawn from the wave nature of light.

2.3   Light Interactions with Matter

When analysing the distribution of light within an environment, we must account for the sources of light, the redirection of light, and the loss of light from the system. The terms emission, scattering, and absorption are used to describe these phenomena, respectively. We discuss each in more detail

in the remainder of this section.

2.3.1 Emission

Emission introduces light into the system. It occurs when another form of energy is converted to light. Forms of emission may be broadly classified into one of two categories: thermal and luminescent [2, 55]. Thermal emission refers to the emission of light caused by heat, whereas luminescent emission is attributable to other factors. We describe these forms in more detail in the following sections.

Thermal Emission

Thermal emission occurs when light is emitted due to heat (*e.g.*, combustion). Specifically, some of the kinetic energy of atoms or molecules in thermal motion is converted into light. The spectral radiant exitance of this emission is described by blackbody radiation, which is a function of temperature [78]:

$$M_{bb}(\lambda, T) = \frac{2\pi hc^2}{\lambda^5} \left(\frac{1}{e^{hc/\lambda kT} - 1} \right), \tag{2.1}$$

where λ represents the wavelength, T represents the temperature, h is Planck's constant, c is the speed of light, and k is the Boltzmann constant. The colour emitted by a blackbody radiator follows a progression from infrared, to red, orange, white, and finally blue as the temperature increases.

Luminescent Emission

Luminescent emission refers to forms of emission resulting from processes other than heat. For example, chemiluminescence results when light is emitted as a result of a chemical reaction, such as the reaction of luminol with iron in the blood that is employed in investigations of crime scenes [49]. Bioluminescnece is a form of chemiluminescence that results when a chemical reaction takes place within a living organism, such as the light emitted by a firefly. Photoluminescence occurs when light is re-emitted as a result of prior absorption by light [69]. Fluorescence and phosphorescence

are forms of photoluminescence. Fluorescence occurs when light at one wavelength is absorbed and then subsequently re-emitted at a longer wavelength [65]. Fluorescent treatments are applied to photocopy paper that re-emit ultraviolet light in the visible region of the spectrum, making them appear brighter. Phosphorescence occurs when light is re-emitted a significant period of time after absorption takes place [65]. This effect is used, for example, in the production of glow in the dark toys.

2.3.2 Scattering

Scattering occurs when a photon is deflected through interactions with material particles or interfaces, thus redistributing light within the environment by removing it from one path and adding it to another [25]. The nature of these interactions (spatial distribution of scattered light, as well as the amount of light that is scattered), depends on the wavelength of light relative to the size of the particles with which it is interacting. This can be divided into three broad scattering regimes, which are distinguished according to the size of the scattering particles relative to the wavelength of light. The first is *Rayleigh scattering*, which occurs when the particles are much smaller than wavelength of light. *Mie theory* describes the scattering that occurs when the size of the scattering particles is on the same order of magnitude as the wavelength of light. Finally, when the scattering particles are much larger than the wavelength of light, *geometric optics* dominates. Each of these light scattering regimes is discussed in more detail below.

Rayleigh Scattering

Rayleigh scattering occurs when the particles are much smaller than the wavelength of light interacting with them. The strength of scattering is inversely proportional to λ^4 [78]. As a result, blue light is scattered preferentially over red light. This phenomenon explains why the sky is blue during the day and red at sunset, as blue light is more likely to be scattered to an observer on the surface of the Earth during the day, yet red light is more likely to traverse the longer path through the atmosphere unscattered when the Sun is low in the sky [9]. It also explains why the Sun appears yellow
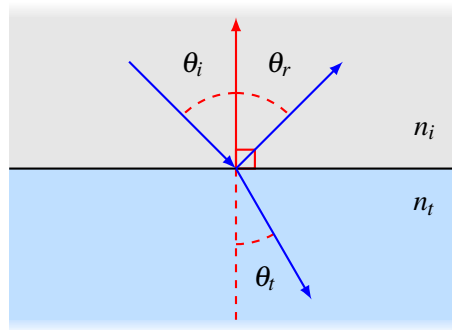
Figure 2.2: At an ideal planar interface between two media, having refractive indices of n_i and n_t, reflected light leaves the surface at an angle equal to that of incidence (Equation 2.2). Transmitted light is refracted according to Snell's law (Equation 2.3). In both cases, light is scattered into the same plane which contains the incident vector and the normal to the interface. Fresnel's equations (Equations 2.4-2.9) describe how much light is reflected and how much is transmitted.

from Earth (whereas from space it appears white), as blue light is more likely to be scattered away from the direct path between the Sun and an observer on Earth.

Mie Scattering

Mie scattering occurs when the particles are of approximately the same order of magnitude in size as the wavelength of light. In the Mie scattering regime, scattering tends to be uniform across all wavelengths. Mie scattering explains, for example, the white appearance of clouds, which are comprised of water droplets of a size approximately of the same magnitude as the wavelength of visible light [17].

Geometric Optics

Geometric optics best describes the interaction of light with objects much larger than the wavelength of the light. Geometric optics explains most of the appearance phenomena encountered on a daily basis. Within the geometric optics regime, light travels in straight lines between interactions with objects in the environment (rectilinear propagation). At an interface between two media, depicted in Figure 2.2, light may be reflected (*i.e.*, scattered back into the medium from which it came) or

transmitted (scattered into the other medium). For an ideal interface, the law of reflection [78],

$$\theta_i = \theta_r, \tag{2.2}$$

describes how light is reflected. Snell's law describes how light is transmitted [78]. It is expressed in terms of the refractive indices, n_i and n_t, of the two media as well as the angles, θ_i and θ_t, between the normal and the incident and transmitted directions, respectively:

$$n_i \sin \theta_i = n_t \sin \theta_t. \tag{2.3}$$

The Fresnel equations describe how much light is subject to either phenomena (reflection or transmission) [78]. It describes, for example, the appearance of glass, which appears more reflective when viewed at an oblique angle than when viewed from the perpendicular direction. Reflectance at an ideal surface is dependent on the polarization of incident light, and may be expressed separately for the component of light oriented so that the electric field is perpendicular to the plane of incidence and the component oriented so that the magnetic field is perpendicular to the plane of incidence. These are called the *transverse electric* (TE) and *transverse magnetic* (TM) modes, respectively [78]. The reflectances for these two components may be expressed as:

$$R_{TE} = \left(\frac{\cos \theta_i - \sqrt{n^2 - \sin^2 \theta_i}}{\cos \theta_i + \sqrt{n^2 - \sin^2 \theta_i}} \right)^2 \tag{2.4}$$

$$R_{TM} = \left(\frac{n^2 \cos \theta_i - \sqrt{n^2 - \sin^2 \theta_i}}{n^2 \cos \theta_i + \sqrt{n^2 - \sin^2 \theta_i}} \right)^2, \tag{2.5}$$

where $n = n_t/n_i$. The reflectance of unpolarized light is then given by

$$R_U = \frac{1}{2} (R_{TE} + R_{TM}). \tag{2.6}$$

15

The transmittances for each component are given by

$$T_{TE} = 1 - R_{TE}, \tag{2.7}$$

$$T_{TM} = 1 - R_{TM}, \tag{2.8}$$

and consequently the transmittance for unpolarized light is

$$T_U = 1 - R_U. \tag{2.9}$$

Additional models have been developed that describe scattering at more complex interfaces [15, 40, 76, 92, 100], although many of these models incorporate these basic laws of geometric optics.

2.3.3 Absorption

Absorption removes light from the environment by converting it into another form of energy [23, 71]. Light that is transmitted into a medium may then be absorbed by pigments or dyes within the medium. The degree to which light is absorbed while travelling through a medium is influenced by several factors, including the concentration, distribution, and absorptivity of the pigments or dyes within the medium [90]. When light is absorbed, its energy is converted into another form such as heat or chemical energy. This may, in turn, lead to chemical change in the medium, resulting in fading or brightness reversion.

Concentration refers to the total amount of pigment present within a given volume of the material. This quantity may be expressed in various forms across different areas of research [69]. For example, in biological fields, concentration is often expressed in terms of amount of substance per unit volume, having SI units of mol/m^3. In other fields, mass per unit volume may be used (*e.g.*, kg/m^3). Concentration may also be expressed as a dimensionless ratio of volumes. With other factors remaining constant, a larger concentration will yield increased absorption.

Absorptivity describes the capacity of a pigment or dye to absorb light. This is an intrinsic property of the pigment or dye which expresses the fraction of light absorbed across a given dis-

tance (m^{-1}) per unit concentration. Accordingly, absorptivity may have SI units of m^2/mol (molar absorptivity), m^2/kg, or m^{-1} depending on how concentration is expressed. A greater absorptivity results in increased absorption.

The distribution of absorbing pigments or dyes within a medium may also influence absorption by the medium as a whole. A homogenous solution consisting of the absorbing pigment within a non-scattering substrate will result in absorption that follows the Beer-Lambert law [69]:

$$I = I_0 e^{-\varepsilon c \ell}, \tag{2.10}$$

where I is the radiant intensity ($W\,sr^{-1}$) after passing through the medium, I_0 is the incident radiant intensity, ε is the absorptivity, c is the concentration, and ℓ is the path length through the medium. Alternatively, if the pigment is concentrated within smaller particles distributed throughout the medium, absorption may be influenced by sieve and detour effects. A ray entering the medium may pass through the entire medium without encountering an absorbing particle. This phenomenon is called the sieve effect, and it results in decreased absorption. Conversely, a ray entering the medium may be subject to scattering within the medium. The resulting increase in path length may result in a higher probability that an absorbing particle is encountered. This phenomenon is referred to as the detour effect, and it results in increased absorption.

2.4 Ray Tracing Pipeline

The ray tracing pipeline describes the process of generating an image from a modeled scene. For realistic image synthesis, we are interested in developing a predictive rendering pipeline [32]. That is, rendered images should accurately represent the appearance of that scene, if it were to exist. In order to generate a photorealistic image, each stage of the pipeline must faithfully simulate the underlying physical processes. Inaccuracies in any of these stages may result in a corresponding reduction in accuracy in the final image. Furthermore, it is possible for subsequent stages in the pipeline to mask inaccuracies in a prior stage, thus resulting in *believable*, yet non-predictive images.

It is therefore important to evaluate each of the components of the rendering pipeline in isolation.

2.5   Rendering Equation

The rendering equation describes how light is influenced by emission, absorption, and scattering by elements within the environment. It is expressed in terms of the radiance, $L(\mathbf{r}, \omega)$, at a point $\mathbf{r}$ in space and in the direction ω. This refers to the power flowing through a differential area around $\mathbf{r}$ in a differential cone of directions around ω, and has units of $\mathrm{W\,m^{-2}\,sr^{-1}}$. In its most general form, light may be emitted, absorbed, or scattered at any point within the environment. This is described by the volumetric rendering equation [3]:

$$\omega \cdot \nabla L(\mathbf{r}, \omega) + \mu(\mathbf{r})L(\mathbf{r}, \omega) = L_e(\mathbf{r}, \omega) + \int_{\mathscr{S}^2} k(\mathbf{r}; \omega' \cdot \omega)L(\mathbf{r}, \omega')\, d\omega'. \tag{2.11}$$

This indicates that the radiance along a path through $\mathbf{r}$ in the direction of ω is reduced by attenuation at a rate of $\mu(\mathbf{r})$ per unit distance, which may be further broken down into attenuation due to absorption, $\mu^a(\mathbf{r})$, and scattering of light into other directions,

$$\mu^s(\mathbf{r}) = \int_{\mathscr{S}^2} k(\mathbf{r}; \omega \cdot \omega')\, d\omega'. \tag{2.12}$$

Conversely, radiance along this path is increased by emission, $L_e(\mathbf{r}, \omega)$, and scattering into the direction ω of light originally travelling in other directions ω'.

Often, only emission, absorption, and scattering events that take place at surfaces are considered. Radiance then remains unchanged along an unobstructed line. That is,

$$L(\mathbf{r}, \omega) = L(\mathbf{r} + t\omega, \omega), \tag{2.13}$$

so long as there is no obstructing surface between $\mathbf{r}$ and $\mathbf{r} + t\omega$. Under this assumption, the rendering

equation may be simplified to

$$L(\mathbf{r}, \omega) = L_e(\mathbf{r}, \omega) + \int_{\mathscr{S}^2} f(\mathbf{r}, \omega, \omega') L(\mathbf{r}, \omega') d\omega'. \tag{2.14}$$

Here $f(\mathbf{r}, \omega, \omega')$ represents the *bidirectional scattering distribution function*, or BSDF, given by

$$f(\mathbf{r}, \omega, \omega') = \frac{dL(\mathbf{r}, \omega')}{L(\mathbf{r}, \omega) \cos \theta \, d\omega}. \tag{2.15}$$

Often this is separated into the bidirectional *reflectance* distribution function (BRDF) and the bidirectional *transmittance* distribution function (BTDF) [6], which refer to f on the regions of the domain where $(\omega \cdot \mathbf{n})(\omega' \cdot \mathbf{n})$ is either negative or positive, respectively. More generally, light may scatter within a medium and be re-emitted at a point separate from where the light entered the medium. Accounting for this yields the bidirectional scattering-surface reflectance distribution function (BSSRDF), $f(\mathbf{r}, \mathbf{r}', \omega, \omega')$. The BSDF is a special case of this where $\mathbf{r} = \mathbf{r}'$ [74].

2.6 Monte Carlo Methods

Several algorithms designed for realistic image synthesis employ the Monte Carlo method [37] to compute the integral described in Equations 2.11 or 2.14. To estimate the value of the integral,

$$I = \int_S f(x) \, dx, \tag{2.16}$$

we draw uniform random samples $x_i \in S$, $1 \leq i \leq N$. The estimate is then given by

$$\hat{I} = \frac{\text{vol}(S)}{N} \sum_{i=1}^{N} f(x_i), \tag{2.17}$$

where

$$\text{vol}(S) = \int_S dx \tag{2.18}$$

denotes the volume of *S*. The variance of this estimate is proportional to $1/\sqrt{N}$ [37].

This may be generalized to allow for drawing samples from *S* according to a distribution described by the probability density function $p(x)$. The estimate then becomes

$$\hat{I} = \frac{\text{vol}(S)}{N} \sum_{i=1}^{N} \frac{f(x_i)}{p(x_i)}. \tag{2.19}$$

By selecting a probability distribution whose probability density function closely resembles *f*, the variance may be reduced. In the ideal case, if *p* is exactly proportional to *f*, the summands become constant and the variance of the estimate becomes zero.

In the last decades, Monte Carlo based rendering systems have been extensively employed in the generation of synthetic images [22]. These systems use the above techniques to evaluate the rendering equation (Equation 2.11 or Equation 2.14).

2.7 Local Illumination

Local illumination describes the interaction of a ray with a material at the boundary of an object within the scene. When a photon impinges on a material within a scene, it may interact with the material in several ways. It may be scattered within the material. The resulting emitted photon may travel outward in a direction given by some probability distribution characterized by the properties of the material. This distribution may be fairly uniform, resulting in a matte appearance, or it may be sharply peaked (*i.e.*, specular), such as glass or a mirror. The photon also may be absorbed. That is, the energy of the photon may be converted into another form, such as heat. How light interacts with the material determines the appearance of that material.

2.7.1 Measurement of Appearance

The appearance of a material may be divided into its spectral attributes and its spatial attributes. The former describes its colour. The latter refers to other qualitiative characteristics, such as whether the material appears matte or glossy. Together, these attributes form the basis for the *measurement of*

appearance [45].

Spectral Component

The spectral component of the measurement of appearance refers to the variation of the reflectance of the material as a function of wavelength. This determines the colour of the material.

Spatial Component

The spatial component of the measurement of appearance refers to the distribution of outgoing scattered photon directions as a function of incident direction. This is usually described by the *bidirectional scattering distribution function*, or BSDF defined earlier (Equation 2.15). Recall that the BSDF is sometimes separated into a bidirectional *reflectance* distribution function (BRDF) and bidirectional *transmittance* distribution function (BTDF). Alternatively, the BRDF may be used alone when the material is opaque. The spatial component determines various qualitative characteristics of the appearance of a material, such as whether a material appears shiny, glossy, matte, transparent or translucent, anisotropic (*e.g.*, brushed metal), etc.

2.8 Global Illumination

Whereas local illumination is concerned with the simulation of light interactions with materials, global illumination refers to the simulation of light transport throughout the scene to be rendered. The emphasis is placed on what happens to light between material interactions. The simulation must account for how the geometry of the scene occludes and distributes light from the light sources. An accurate simulation of global illumination within a scene will faithfully reproduce phenomena such as soft shadows, diffuse interreflections, colour bleeding, and caustics. Popular methods for simulating global illumination are path tracing and bidirectional path tracing [64, 97], Metropolis light transport [97, 98, 57], photon mapping [50, 51], and radiosity [31].

Despite this difference in emphasis, global illumination and local illumination are closely re-

lated. Many local illumination models are designed around modelling the small-scale geometry comprising the material. These are effectively precomputations of the "global" illumination simulation at this scale. Conversely, one can imagine that precomputing a reflectance model representing an entire scene might be useful as viewed from afar [26]. A key distinction between global illumination and local illumination in this context is that the geometry is often viewed as fixed relative to nearby geometry in the latter case. At the scale of an entire scene, however, various components are often moved around, making such precomputation impractical [26].

2.9 Photometry

Photometry refers to the perception of electromagnetic radiation by a human observer [106]. Typically, at the end of the rendering pipeline, spectral power distributions must be converted to some colour space (such as an RGB colour space) to be displayed on a screen. Accurately transforming spectral power distributions to RGB requires modeling the human visual system, as well as the display characteristics of the screen. The human eye contains two types of light receptors: rods and cones. Rods are sensitive to brightness, while cones are sensitive to colour. There are three types of cones, which are sensitive to light having long, medium and short wavelengths. As a result, colour spaces are typically three-dimensional.

2.9.1 CIE XYZ Colour Space

The XYZ colour space was developed by the *Commision Internationale de l'Éclairage* (CIE). Colour matching experiments were used to model a standard human observer [90]. For these experiments, lights having three primary colours (red, green, and blue) were provided, as well as a reference light. The subject could vary the intensity of the primary colours and was instructed to mix the primary colours in order to match the reference colour. Because not all colours could be reproduced from the three primaries, the subject was also allowed to shine a primary colour onto the reference colour instead, effectively assigning a *negative* intensity to that primary. This test was
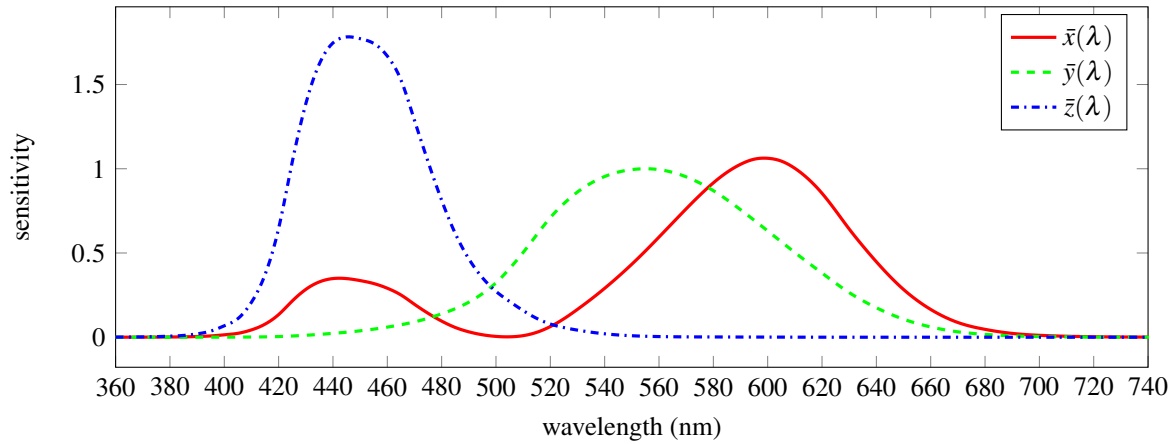
Figure 2.3: The colour matching functions for the CIE XYZ colour space [89].

repeated using monochromatic light, at several wavelengths, as reference colours. This would yield red, green and blue colour matching functions: $\bar{r}(\lambda)$, $\bar{g}(\lambda)$, and $\bar{b}(\lambda)$, respectively. The amount of red, green, and blue light needed to reproduce the colour of light having a spectrum $L(\lambda)$ would then be:

$$R = \int \bar{r}(\lambda)L(\lambda)\,d\lambda, \tag{2.20}$$

$$G = \int \bar{g}(\lambda)L(\lambda)\,d\lambda, \tag{2.21}$$

$$B = \int \bar{b}(\lambda)L(\lambda)\,d\lambda. \tag{2.22}$$

A linear transformation was then applied to this colour space so that the corresponding colour matching functions would always be non-negative forming the XYZ colour space, with colour matching functions $\bar{x}(\lambda)$, $\bar{y}(\lambda)$, and $\bar{z}(\lambda)$. These functions are depicted in Figure 2.3. The colour corresponding to light having the spectrum $L(\lambda)$ is then computed by:

$$X = k \int \bar{x}(\lambda)L(\lambda)\,d\lambda, \tag{2.23}$$

$$Y = k \int \bar{y}(\lambda)L(\lambda)\,d\lambda, \tag{2.24}$$

$$Z = k \int \bar{z}(\lambda)L(\lambda)\,d\lambda, \tag{2.25}$$

23
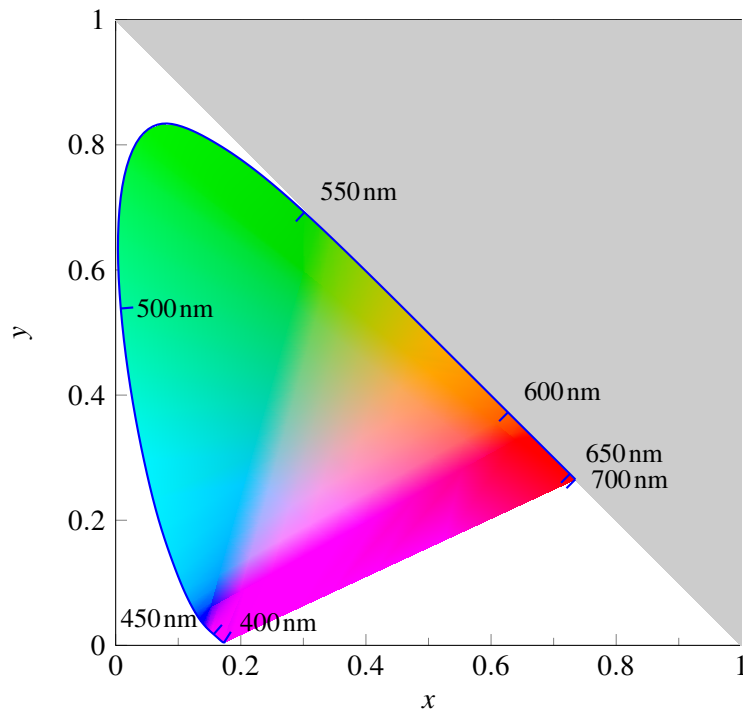
Figure 2.4: The CIE chromaticity diagram depicting the colours corresponding to the chromaticity coordinates *x* and *y* expressed in Equations 2.26 and 2.27. The outer edge of the horseshoe depicts the monochromatic colours in the visible region of the electromagnetic spectrum.

where $k = 683\,\text{lm}\,\text{W}^{-1}$ is the peak luminous efficacy for photopic vision. Note that the colour matching functions are normalized so that $\bar{y}(555\,\text{nm}) = 1$. The XYZ colour space also has the property that Y corresponds to luminance, or the overall brightness of a colour. The colour may be expressed independently of the luminance by evaluating the chromaticity coordinates:

$$x = \frac{X}{X+Y+Z},$$
(2.26)

$$y = \frac{Y}{X+Y+Z}.$$
(2.27)

The resulting colours are depicted in Figure 2.4.

2.9.2 CIE L*a*b* Colour Space

The CIE XYZ colour space is a linear projection of the spectral radiance curve, $L(\lambda)$. Human perception, however, relates to radiance in a non-linear fashion. That is, the distance between two points in CIE XYZ space will not necessarily correspond to the subjective difference between those colours. The CIE L*a*b* colour space is a transformation of the CIE XYZ space in which the Euclidean distance does indicate a better difference between colours according to human perception, with the unit distance corresponding to a *just noticeable difference*.

Like CIE XYZ, the CIE L*a*b* colour space is a three dimensional colour space. The L^* coordinate indicates the luminance, a^* the colour along the blue-yellow axis, and b^* the colour along the red-green axis. The point $L^* = 100$, $a^* = b^* = 0$ corresponds to the reference white.

The following equations may be employed to convert from CIE XYZ to CIE L*a*b* colour space using X_w, Y_w, and Z_w as the reference white [90]:

$$L^* = 116 \left(f \left(\frac{Y}{Y_w} \right) - \frac{16}{116} \right) \tag{2.28}$$

$$a^* = 500 \left(f \left(\frac{X}{X_w} \right) - f \left(\frac{Y}{Y_w} \right) \right) \tag{2.29}$$

$$a^* = 200 \left(f \left(\frac{Y}{Y_w} \right) - f \left(\frac{Z}{Z_w} \right) \right), \tag{2.30}$$

where

$$f(t) = \begin{cases} t^{1/3} & \text{if } t > 0.008856 \\ 7.787t + \frac{16}{116} & \text{otherwise.} \end{cases} \tag{2.31}$$

The distance between two points is then referred to by

$$\Delta E = \left((L_2^* - L_1^*)^2 + (a_2^* - a_1^*)^2 + (b_2^* - b_1^*)^2 \right)^{1/2}. \tag{2.32}$$

25

2.9.3 sRGB Colour Space

Often images will need to be converted to an RGB colour space, for example to be displayed on a monitor. In the absense of an RGB space indicated by the colourimetric properties of the actual display, the standard RGB (sRGB) colour space may be used. To convert from CIE XYZ to sRGB, we must first apply a linear transformation to the XYZ coordinates, yielding linear RGB coordinates:

$$\begin{pmatrix} R' \\ G' \\ B' \end{pmatrix} = \begin{pmatrix} 3.2410 & -1.5374 & -0.4986 \\ -0.9692 & 1.8760 & 0.0416 \\ 0.0556 & -0.2040 & 1.0570 \end{pmatrix} \begin{pmatrix} X \\ Y \\ Z \end{pmatrix}. \tag{2.33}$$

Next, we apply a transformation, $f(t)$, to each channel to account for the non-linear response of a typical display, where

$$f(t) = \begin{cases} 1.055t^{1.0/2.4} - 0.055 & \text{if } t > 0.0031308 \\ 12.92t & \text{otherwise.} \end{cases} \tag{2.34}$$

The sRGB coordinates are then given by $R = f(R')$, $G = f(G')$, and $B = f(B')$.

2.10 Predictive Modeling

A model is predictive if it is capable of reproducing the spectral or spatial appearance of real materials when provided with the data characterizing that material. This, in turn, requires that a proposed model be validated through comparisons with physical measurements [32].

For artistic applications in computer graphics, predictive models may assist in automating aspects of scene design, allowing the artist to focus on the creative aspect of their work. Instead of tweaking meaningless paramaters to achieve a desired appearance, the artist can adjust parameters relevant to the material in question. The artist can then be confident that he or she has a realistic starting point from which to work.

Furthermore, in general multiple spectral curves may yield identical perceived colours. That

is, $L_1(\lambda)$ and $L_2(\lambda)$ may yield identical tristimulus values (X, Y, Z) when substituted into Equation 2.25. This phenomenon is called *metamerism* [90]. A consequence when employing non-predictive models is that the artist may determine a parameter set that achieves a realistic appearance in one environment (*i.e.*, lighting conditions, surroundings, etc.). However, a subsequent change to the environment may render that object's appearance unrealistic. By employing predictive models, the artist is assured that a realistic appearance will be maintained regardless of subsequent changes to other aspects of the scene.

Chapter 3

Related Work

In this chapter, we review the literature related to the topics discussed in this dissertation. In Section 3.1, we provide an overview of the state of the art with regard to the simulation of the broader class of aging and weathering phenomena in computer graphics. This includes methods developed at simulating particular processes, such as the formation of metallic patinas, as well as data-driven techniques aimed at reproducing wider range of aging effects. In Section 3.2, we review investigations into lightfastness of materials in the conservation literature. In Section 3.3, we outline the research related to yellowing, or brightness reversion. In Section 3.4, we discuss previous applications of Kubelka-Munk theory, which is employed in this dissertation. In Section 3.5, we outline works aimed at digital restoration of faded works of art.

3.1 Aging and Weathering

While there have been many recent advances toward the modeling of aging and weathering phenomena in computer graphics, the work presented here is, to the best of our knowledge, the first to address the physically-based simulation of light exposure effects on material appearance over time[*]. For in-depth surveys on the modeling of aging and weathering phenomena, the reader is referred to

---

[*]Note that this work was originally published in 2013 [60].

the comprehensive texts by Dorsey *et al.* [21] or Mérillou and Ghazanfarpour [70]. In the following, we present an overview of relevant techniques used to render aging and weathering effects. For the purpose of this overview, we loosely divided these techniques into two groups: phenomenological and functional.

3.1.1 Phenomenological Techniques

Phenomenological techniques are targeted toward particular effects. For example, Dorsey and Hanrahan [19] applied erosion and deposition to a layered surface model in order to simulate and render metallic patinas, while Dorsey *et al.* [20] simulated water flow over a surface using particle systems to account for the transport of material and the resulting aged appearance. More recently, Chen *et al.* [13] extended this idea by allowing weathering particles to leave the surface by reflection (as in photon transport), and by bouncing off a surface, in addition to flowing along a surface. They also employed the results of their weathering transport computation to render other types of weathering phenomena besides those involving transport of material by water. Bosch *et al.* [10] developed techniques for determining flow simulation parameters from images.

There has also been much effort devoted to the simulation of organic materials. Kider *et al.* [59] used a biologically motivated reaction-diffusion approach to simulate the deterioration of fruit. Iglesias-Guitan *et al.* [46] proposed a model for simulating the aging of human skin. Chen *et al.* [12] developed a hyperspectral model for skin appearance, which was subsequently used to simulate skin tanning effects due to ultraviolet exposure [11]. More recently, Barros and Walter [5] proposed a model to simulate the most frequent types of human skin pigmentation disorders.

3.1.2 Functional Techniques

Functional techniques are more broadly applicable, but require prior acquisition of the time-varying BRDF data describing the desired effect. For example, Gu *et al.* [34] developed a database of the time-varying appearance of materials undergoing various natural processes such as drying or corrosion. This is expressed in the form of a seven dimensional Time and Spatially-Varying BRDF (TSV-

BRDF). They described a procedure for factoring the TSV-BRDF into temporally and spatially varying components which may then be stored compactly in their database. Similarly, Wang *et al.* [99] noted that the spatially varying appearance of a weathered material, for example rust forming on a sheet of metal, typically reflects variation in the degree of weathering. From spatially variant BRDF data captured from a weathered material sample at a single instant in time, they organized the variety of appearances present in a particular weathering process into an appearance manifold. This manifold was then used to synthesize new textures of the same material representing its weathered appearance at different points in time.

3.2 Fading

The relevant work on fading and lightfastness of materials comes primarily from the conservation field. Giles and McKay [29] and Giles [27] studied the factors and mechanisms that contribute to fading of dyes and pigments. They found that a finely dispersed dye would fade more readily than one in an aggregate form. Johnston-Feller *et al.* [53] studied the fading rates of thin films of several pigments under various levels of exposure. They observed that the fading behavior followed first order kinetics, *i.e.*, the rate at which pigment is lost over time is proportional to its concentration. The formulation of our framework is consistent with these findings. In addition, it accounts for a wide range of variations in the light exposure and sample conditions.

Whitmore and Bailie [101] developed a mathematical model to describe the fading of transparent glazes. Their model was limited to non-scattering media subjected to monochromatic illumination. These simplifications allowed them to consider the medium as a whole without accounting for the variation in fading with depth. Our proposed framework removes these limitations.

Morris and Whitmore [72] extrapolated the results of micro-fading tests to visualize the faded appearance of an entire painting or museum object. Small areas (approximately $0.4\,\text{mm}^2$) of the object were faded with intense illumination while the colour was continuously measured to produce a fading curve in CIE Lab space [102]. The results of these micro-fading tests were extrapolated

to visualize the entire object after years of light exposure [72]. While this approach may correctly predict the fading of other areas of the object having the same properties as the measured sample, it is unclear how it can correctly predict the fading rate of areas with different properties (*e.g.*, distinct pigment composition). In addition, this data-driven approach is limited to simulating the rate of fading of the material measured under the specific illumination used in the test. In contrast, the comprehensive physicochemical approach employed in our framework allows us to perform not only data-driven, but also theoretical fading simulations involving materials with different properties and subject to a wide range of illumination conditions.

Shi *et al.* [86, 87] used per-pixel spline interpolation in the RGB colour space in order to visualize the appearance of fading works of art at intermediate stages. The initial and final results of the fading processes are required as input. This is not always feasible, particularly when the processes involved take place over extended periods of time. In addition, it is worth noting that this technique was not designed to predict how fading may evolve under hypothetical circumstances. Our proposed framework is based on the simulation of physicochemical processes. While it requires knowledge of the spectral properties of the byproducts of these processes, the final result is not directly employed as an input parameter.

3.3 Yellowing

Paper that has not been chemically treated turns yellow during prolonged exposure to daylight, and ultraviolet light in particular [42]. This process is called *brightness reversion*. Brightness reversion occurs as lignin, which accounts for 17-35% by weight of the wood used in paper production [81], undergoes a photochemical reaction resulting in the formation of yellow chromophores known as *orthoquinones* [42]. Heitner [42] outlines the development of current understanding of the reaction pathways involved in paper yellowing. To the best of our knowledge, this phenomenon has not been specifically addressed in the computer graphics literature before.

3.4 Applications of Kubelka-Munk Theory

The theory for light transport in a uniform medium proposed by Kubelka and Munk [63] has been extended and successfully employed in a wide assortment of disciplines to simulate light interactions with various man-made and natural materials, from plastics [83] and printer inks [105] to plants [84] and human skin [18]. In conservation, Johnston-Feller [52] employed the K-M theory to account for the effects of light exposure on museum objects using empirical techniques. In computer graphics, Haase and Meyer [35] applied the K-M theory to facilitate correct colour calculations for realistic image synthesis. Subsequently, this theory has been employed in the rendering of artistic effects involving painting media such as watercolours [16] and wax crayons [82]. It has also been used as a component in more complex models. For example, Dorsey and Hanrahan [19] simulate natural processes, such as erosion and deposition, in a layered model based on the earlier work of Hanrahan and Krueger [38] to achieve the appearance of a metallic patina. They used K-M theory to account for the scattering and absorption within each layer. Abdul-Rahman and Chen [1] employed the K-M theory to propose a spectral volume rendering technique that more accurately accounts for absorption and scattering properties than simple alpha blending in RGBA space*. More recently, Hašan *et al.* [39] incorporated the K-M theory in their work aimed at fabricating objects with predetermined subsurface scattering properties.

3.5 Digital Restoration

In conservation literature, teams at the Harvard Art Museum and the MIT Media Lab collaborated to develop computational techniques for transforming measured colour changes into patterns of illumination that may be projected onto faded murals in order to restore them to their original appearance [41]. In contrast to traditional art restoration techniques, this approach preserves the original artifact and is completely reversible. Berns [7] and Berns *et al.* [8] proposed methods for

---

*In RGBA, colours are represented by four components: red, green, blue, alpha [90]. The alpha channel denotes the opacity, and multiple colours may be combined by multiplying the first three channels by alpha and summing the results.

digital restoration of paintings by using a single-constant Kubelka-Munk model to compute the intermediate appearance stages of faded artwork, given measured spectral properties of the faded and unfaded pigments.

3.6 Summary

Various aging and weathering phenomena have been studied extensively in the computer graphics literature. In addition, particular aspects of fading and yellowing of pigments and dyes have been studied in the conservation literature. The research presented in this dissertation, however, represents the first framework in computer graphics for simulating the fading and yellowing of materials using a first principles approach [60].

Chapter 4

Theoretical Framework

The goal of the proposed framework is to account for the light induced changes in material appearance as time progresses. In particular, we consider spectral changes such as the fading of pigments and dyes or the light-induced yellowing of paper.

These changes in appearance require that a chemical reaction takes place within the material [29]. To compute the effect of light exposure therefore requires that we understand the subsurface light environment. Furthermore, conservation of energy dictates that, in the case of light induced fading, absorption takes place in order to initiate a reaction. This is known as the Grotthus–Draper law [29]. The induced changes in material properties within the subsurface volume are then accumulated over time.

In the following, we begin by describing the theoretical underpinnings for our framework. Using the scattering model proposed by Kubelka and Munk [63], we then examine in detail the application of the proposed framework to single-flux and two-flux scenarios. Even in these cases, as we shall see, numerical techniques will be required to solve the resulting systems of equations.

4.1 General Framework

To describe the light environment below the surface of the material to be subjected to light exposure over time, we begin with the general equation for light transport in three dimensional space [3]:

$$\omega \cdot \nabla L(\mathbf{r}, \omega) + \mu(\mathbf{r}) L(\mathbf{r}, \omega) = L_e(\mathbf{r}, \omega) + \int_{\mathscr{S}^2} k(\mathbf{r}; \omega' \cdot \omega) L(\mathbf{r}, \omega') \, d\omega', \tag{4.1}$$

where $L(\mathbf{r}, \omega)$ denotes the radiance at position $\mathbf{r}$ in the direction $\omega = (\theta, \phi)$, μ is the attenuation coefficient, L_e is the emitted radiance, and k represents the volume scattering kernel. Equation 4.1 indicates that the radiance along a path is reduced by absorption and out-scattering, and increased by emission and in-scattering. Scattering and absorption are accounted for everywhere in three dimensional space, thereby handling participating media and subsurface scattering in a natural way. This is more general than the familiar light transport equation given by Kajiya [56], which only considers absorption and scattering at surfaces.

Generally, an additional term,

$$\frac{1}{c} \frac{\partial L}{\partial t},$$

is added to the left hand side of Equation 4.1 which accounts for time-dependent phenomena due to the finite speed of light, denoted by c [3]. Although we are interested in the simulation of time-dependent phenomena, the processes that we are investigating take place over time scales much larger than the amount of time required for light to be transported from one point to another in a typical scene. Hence, we are still using the approximation that light is transported instantaneously between any two points.

To account for the effects of light exposure over time, we first introduce time as a parameter to all components of Equation 4.1: L, L_e, k, and μ. Differential equations are then derived to describe how $\mu(\mathbf{r}, t)$ and $k(\mathbf{r}, t; \omega' \cdot \omega)$ vary with light exposure, denoted by $L(\mathbf{r}, \omega, t)$, over a period of time. The system of differential equations that includes Equation 4.1 and the additional differential equations
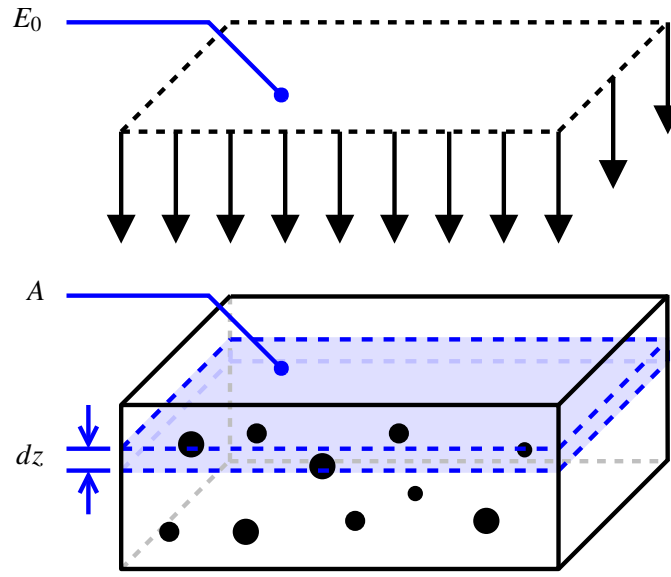
Figure 4.1: An initially homogeneous slab of absorbing material is subjected to collimated illumination of uniform irradiance E_0 from above. The particles are small relative to the volume of the slab. In particular, we are interested in the cross section $A\,dz$, which is illuminated by an unknown radiant flux density E after having been absorbed by the portion of the slab above it.

describing the effects of light exposure must then be solved. Typically, to obtain a solution, one will be required to use numerical methods. This will be discussed in Chapter 5.

4.2   Uniform Slab

In this section, we consider the case of a uniform slab of absorbing and scattering material subjected to collimated illumination from above (see Figure 4.1). Absorption and scattering take place at colourant particles distributed (initially uniformly) throughout the medium. These particles are considered to be small relative to the thickness of the medium. We shall employ the two-flux approach similar to the theory originally proposed by Kubelka and Munk [63]. Since, in this section, we are considering radiation in the upward and downward directions only, all quantities vary only along the z-axis. We shall therefore use z in place of **r** in the following analysis.

4.2.1   Single-flux Model

As an initial example, we shall consider a uniform slab of absorbing particles subjected to collimated illumination from above. This is analogous to the special case of the K-M theory in which it is assumed that scattering is absent.

The single-flux model may be described in terms of Equation 4.1 by expressing quantities in terms of the radiant flux density (irradiance), $E(z)$, as follows [43]:

$$L(z, \omega) = E(z)\delta(\omega, \mathbf{k}), \tag{4.2}$$

$$L_e(z, \omega) = E_0\delta(z)\delta(\omega, \mathbf{k}), \tag{4.3}$$

$$k(z; \omega' \cdot \omega) = 0, \tag{4.4}$$

where $\delta(x)$ represents the Dirac delta function and $\mathbf{k}$ represents the unit vector in the direction of increasing z. For brevity, we define

$$\delta(\omega_1, \omega_2) = \delta(\cos\theta_1 - \cos\theta_2)\delta(\phi_1 - \phi_2). \tag{4.5}$$

Substituting the above into Equation 4.1, we find that E satisfies the following equation when $\omega = \mathbf{k}$:

$$\frac{\partial E(z)}{\partial z} + \mu(z)E(z) = 0, \tag{4.6}$$

which we shall write more concisely as

$$E_z = -\mu E. \tag{4.7}$$

We also obtain the boundary condition $E(0) = E_0$. Note that whenever $\omega \neq \mathbf{k}$, we have $E = 0$.

Next, we must express how μ varies as a function of time. The slab $A\,dz$ in Figure 4.1 is lit from above by collimated illumination of irradiance E. Let σ_g represent the cross-sectional area of the colourant per unit total volume of the slab (in m^{-1}). This can be expressed in terms of

simpler quantities as $\sigma_g = f\sigma_p$, where f is a dimensionless quantity representing the fraction of total volume occupied by the particulate, and σ_p is the cross-sectional area per unit volume of the particulate (in m^{-1}). These quantities are intrinsic properties of the size, shape, and orientation distribution of the particles. Hence, $\sigma_g EA\,dz$ watts impinge upon the absorbing particles. In the context of our framework, we define the *absorption efficiency*, $\alpha^a \in [0, 1]$, as the fraction of power absorbed by a particle with respect to the total power impinging on it. The remaining power is transmitted. Defining $\mu^a = \alpha^a \sigma_g$ as the volumetric absorption coefficient, we have that $\mu^a EA\,dz$ watts are absorbed. Note that $\mu = \mu^a$ for a non-scattering medium.

We define β, in m^3 J^{-1}, as the volume of absorbing matter consumed by a given amount of energy. This is consistent with prior observations found in the conservation literature [73]. The volume of the colourant that changes with time is then expressed as

$$dv = -\beta\mu^a EA\,dz\,dt, \tag{4.8}$$

where v is the volume of absorbing matter in the slab $A\,dz$. Equation 4.8 describes how the volume of the colourant changes with time. Dividing both sides by the total volume $A\,dz$ yields

$$df = -\beta\mu^a E\,dt. \tag{4.9}$$

Substituting $f = \mu^a/(\alpha^a \sigma_p)$ gives

$$d\mu^a = -\alpha^a \sigma_p \beta\mu^a E\,dt. \tag{4.10}$$

Assuming that absorbed radiation only changes the volume of particulate matter, and not its distribution (*i.e.*, α^a and σ_p remain constant), we are then left with the following system of differential equations from Equations 4.7 and 4.10:

$$E_z = -\mu^a E, \tag{4.11}$$

$$\mu_t^a = -\beta'\mu^a E, \tag{4.12}$$

where $\beta' = \alpha^a \sigma_p \beta$ is the cross-sectional area of the colourant consumed per unit energy absorbed (in $m^2 J^{-1}$). As indicated by Equation 4.12, the parameter β' determines the rate at which a material will *fade* over time.

If we differentiate both sides of Equation 4.11 with respect to t, followed by multiplying both sides by E, we obtain

$$EE_{zt} = -\mu_t^a E^2 - \mu^a EE_t. \tag{4.13}$$

We can eliminate μ_t^a by substituting Equation 4.12 into the above, yielding

$$EE_{zt} = \beta'\mu^a E^3 - \mu^a EE_t. \tag{4.14}$$

Finally, substituting Equation 4.11 for both terms on the right side, we get

$$EE_{zt} + \beta' E_z E^2 - E_z E_t = 0. \tag{4.15}$$

Additionally, we have the following boundary conditions:

$$E(z,0) = E_0 e^{-\mu_0^a x}, \tag{4.16}$$

$$E(0,t) = E_0, \tag{4.17}$$

$$E(z,\infty) = E_0, \tag{4.18}$$

$$E(\infty,t) = 0. \tag{4.19}$$

Equation 4.16 describes the slab at time $t = 0$, before any absorbing matter has been consumed. At this time, the slab is uniform. Hence, Beer's law (Equation 2.10) applies. The irradiance at the surface, $z = 0$ is held constant at E_0 by assumption, yielding Equation 4.17. Eventually, all

absorbing matter is consumed above any given fixed depth z. This is realized in Equation 4.18. At any fixed time t, all incident radiation is absorbed at some depth, yielding Equation 4.19.

4.2.2 Two-flux Model

Next, we extend the model described in the previous section to account for scattering. We consider upwelling and downwelling radiation in a manner analogous to that described by Kubelka and Munk [63].

Let E^d indicate the downwelling flux density and E^u indicate the upwelling flux density. After traversing a unit distance dz, E^d is diminished due to absorption by $\mu^a E^d\, dz$, due to outscattering by $\mu^s E^d\, dz$, and augmented due to inscattering by $\mu^s E^u\, dz$. The upwelling flux density E^u is diminished and augmented in a similar manner, yielding the following system of differential equations:

$$E_z^d = -(\mu^a + \mu^s)E^d + \mu^s E^u, \tag{4.20}$$

$$-E_z^u = -(\mu^a + \mu^s)E^u + \mu^s E^d. \tag{4.21}$$

Note that, as with the single-flux case, these equations may also be derived from Equation 4.1 by substituting the following:

$$L(z, \omega) = E^d(z)\delta(\omega, \mathbf{k}) + E^u(z)\delta(\omega, -\mathbf{k}), \tag{4.22}$$

$$\mu(z) = \mu^a + \mu^s, \tag{4.23}$$

$$L_e(z, \omega) = E_0\delta(z)\delta(\omega, \mathbf{k}), \tag{4.24}$$

$$k(z; \omega' \cdot \omega) = \mu^s\delta(\omega' \cdot \omega + 1). \tag{4.25}$$

Equations 4.20 and 4.21 may also be expressed in terms of the sum, $F = E^d + E^u$, and difference, $D = E^d - E^u$, of the radiant flux densities in either direction. The sum and difference of

Equations 4.20 and 4.21 are given, respectively, by

$$D_z = -\mu^a F, \tag{4.26}$$

$$F_z = -(\mu^a + 2\mu^s)D. \tag{4.27}$$

More generally, the quantity F is given by

$$F(\mathbf{r}) = \int_{\mathcal{S}^2} L(\mathbf{r}, \omega) \, d\omega. \tag{4.28}$$

This quantity, called the *fluence rate* (in $\mathrm{W\,m}^{-2}$), describes the total irradiance impinging on a given point in space.

The derivation of the expressions describing the variation of μ^a over time proceeds as before, except that now incident radiation is absorbed from both directions. Thus, E is substituted by F in Equations 4.8–4.10 and 4.12, yielding the following expressions:

$$df = -\beta \mu^a F \, dt, \tag{4.29}$$

$$\mu_t^a = -\beta' \mu^a F. \tag{4.30}$$

To obtain the corresponding expression for μ^s, we introduce the *scattering efficiency*, α^s, denoting the fraction of power scattered by a particle with respect to the total power impinging on it. The scattering coefficient is then given by $\mu^s = \alpha^s \sigma_g$. Note that $\alpha^s = \mu^s/\sigma_g$ and $\alpha^a = \mu^a/\sigma_g$. Multiplying both sides of Equation 4.30 by α^s/α^a yields

$$\mu_t^s = -\beta' \mu^s F. \tag{4.31}$$

4.2.3 Mixtures

Next, we consider a colourant consisting of a mixture of component substances (pigments or dyes). Let the absorption and scattering coefficients be given by μ_j^a and μ_j^s, respectively. The absorption

and scattering components of the mixture are then

$$\mu^a = \sum_j \mu_j^a, \tag{4.32}$$

$$\mu^s = \sum_j \mu_j^s. \tag{4.33}$$

The absorption and scattering coefficients of the mixture are used to determine how F varies with depth, z, following the same procedure as above. However, the reduction in the volume fraction occupied by each single colourant is proportional to the energy absorbed by this particular colourant. Thus, we have $df_j = -\beta_j \mu_j^a F \, dt$ for $j = 1, \ldots, m$. Following the same derivation as above, we get $\mu_{j,t}^a = -\beta_j' \mu_j^a F$ and $\mu_{j,t}^s = -\beta_j' \mu_j^s F$ for each colourant j.

We remark that β' is proportional to absorption efficiency α^a. Consequently, any colourant that does not absorb ($\alpha^a = 0$) will not fade. This is consistent with the law of conservation of energy. If a medium consists of a mixture where some components scatter but do not absorb, and the remainder absorb but do not scatter, then the scattering components will not fade. Consequently, the scattering will be left unaffected by light exposure. In this instance, we consider μ^s as constant and drop the equations affecting μ_j^s with time. We are then left with the following system of differential equations similar to Equations 4.11 and 4.12 from the single-flux case:

$$D_z = -\mu^a F, \tag{4.34}$$

$$\mu_{j,t}^a = -\beta_j' \mu_j^a F. \tag{4.35}$$

To solve this system, we proceed in a similar manner as before (Equations 4.13 to 4.15).

If there is only a single absorbing colourant, $\mu_1^a = \mu^a$, then the system of differential equations may be reduced to

$$F D_{zt} + \beta_a' D_z F^2 - D_z F_t = 0. \tag{4.36}$$

Note that when $E^u = 0$, we have $F = D = E^d$ and Equation 4.36 reduces to Equation 4.15.

4.2.4 Spectral Considerations

In the multi-spectral context, the reduction in the volume fraction of a colourant is proportional to the energy absorbed by that colourant across the entire spectrum. That is,

$$df_j = -\beta_j \, dt \int_0^\infty \mu_j^a F_\lambda \, d\lambda. \tag{4.37}$$

Here, the absorption coefficients μ_j^a become wavelength dependent and the fluence rate is substituted by the *spectral fluence rate*, F_λ (having units of $\mathrm{W\,m^{-2}\,nm^{-1}}$). Rather than folding Equation 4.37 into an expression in terms of $d\mu_j^a$ as was done prior, we instead use Equation 4.37 as is. We then compute μ_j^a in terms of the changing volume fraction f_j and a constant (with respect to time) *specific* absorption coefficient $\mu_j^{a*} = \alpha_j^a \sigma_p$, yielding $\mu_j^a = f_j \mu_j^{a*}$.

4.3 Non-trivial Breakdown Products

In some cases, the breakdown products of a light dependent reaction may not be colourless. For instance, some papers develop a yellow hue after exposure to ultraviolet light. This may be attributed to the formation of orthoquinones when the lignin is irradiated with UV light [42]. To account for this, we add a positive term to the equations in the system, to model the increase in these breakdown products due to light absorption:

$$df_j = -\beta_j \mu_j^a F \, dt + \sum_{i \neq j} \gamma_{i,j} \mu_i^a F \, dt. \tag{4.38}$$

for $j = 0, \ldots, m$, where $\gamma_{i,j}$ denotes the rate at which constituent i breaks down into constituent j due to light absorption by i. If only a single constituent breaks down into j, then only a single term in the above summation will be non-zero.

4.4 Summary

In this chapter, we have provided the framework describing the influence of exposure to light over time on appearance. By introducing time as a key parameter into the rendering equation, this framework accounts for the photochemical processes of pigment and dye fading. We have explored some particular cases within this framework, namely the single-flux and two-flux models, which will serve as the basis for study in the remainder of this dissertation. In the following chapters, we will discuss how to evaluate these models numerically under a given set of initial conditions. We will then examine the effectiveness of the framework for predicting the progression of spectral appearance changes under experimental conditions.

Chapter 5

Numerical Approaches

5.1   Overview

To the best of our knowledge, the systems of equations developed in the preceding chapter have no closed form solution [80]. We must therefore resort to numerical methods. To accomplish this task, we first discretize the domain in the vertical depth (z) and the time (t) dimensions. We then solve the problem in each dimension in turn, holding μ^a and μ^s constant within each interval. We have used uniform depth and time intervals in our analysis for simplicity, although arbitrary discretization strategies may be employed. Extending the following to allow for variable depth and/or time steps is straightforward.

5.2   Depth Discretization Step

To solve for the radiant flux densities E^d and E^u at a fixed time, we discretize along the z-axis into N layers and hold μ^a and μ^s constant within each layer as depicted in Figure 5.2.
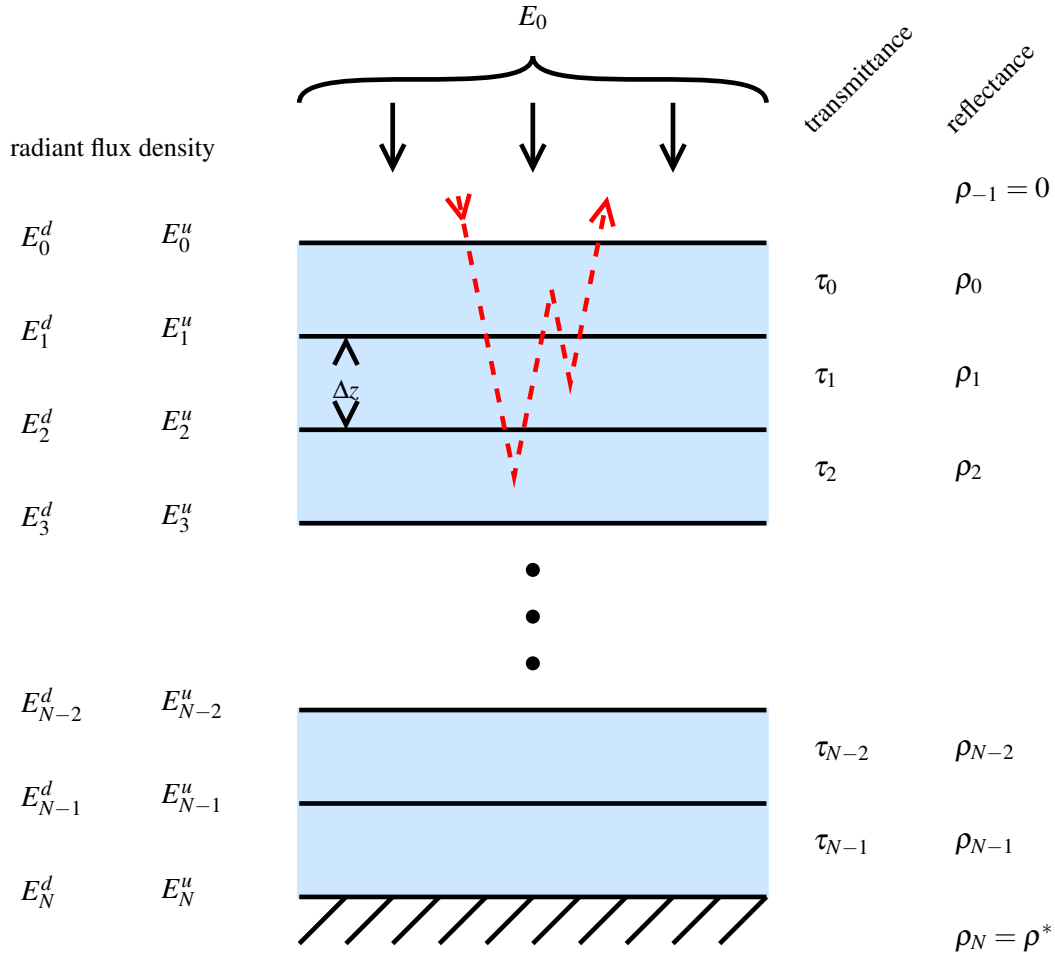
Figure 5.1: Diagram depicting the vertical discretization of the simulated medium according to the two-flux model. The thickness of each layer is denoted by Δz. Each layer is uniform in its absorption and scattering, from which the reflectance and transmittance of the layer in isolation, as indicated on the right, may be computed using the K-M theory [Kubelka 1948]. From these quantities, the radiant flux density at the layer boundaries, shown on the left, may be determined. The dashed line schematically describes a sample path through the medium.

5.2.1 Reflectance and Transmittance of a Layer

Under these assumptions, the reflectance and transmittance of each layer may be computed by integrating Equations 4.20 and 4.21, as described by Kubelka [62], yielding:

$$\rho_i = \frac{1}{a_i + b_i \coth b_i \mu_i^s \Delta z}, \tag{5.1}$$
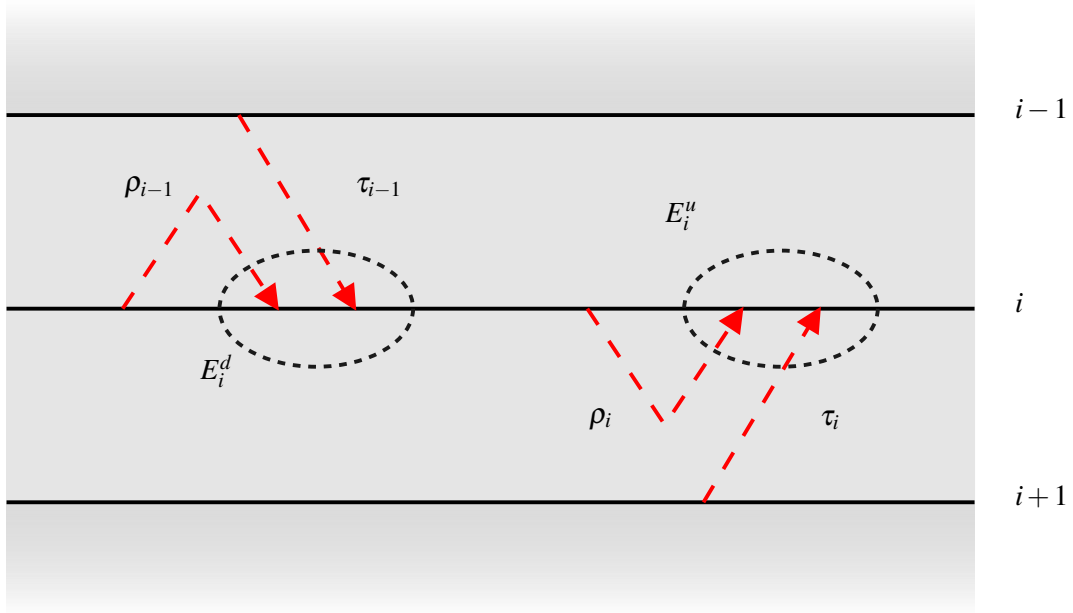
Figure 5.2: Diagram depicting the light paths that contributed to the upward and downward radiant flux densities, E, at the ith layer interface in terms of the radiant flux densities at the adjacent layer interfaces and in terms of the reflectances (ρ) and transmittances (τ) of the adjacent layers.

$$\tau_i = \frac{b_i}{a_i \sinh b_i \mu_i^s \Delta z + b_i \cosh b_i \mu_i^s \Delta z}, \tag{5.2}$$

where

$$a_i = (\mu_i^s + \mu_i^a)/\mu_i^s \tag{5.3}$$

and

$$b_i = \sqrt{a_i^2 - 1}. \tag{5.4}$$

Since each layer has uniform scattering and absorption properties throughout, the reflectance and transmittance of each layer is the same from below as from above.

For an ideal white scatterer, we have $\mu_i^a = 0$. The reflectance and transmittance of such a layer

reduces to [63]

$$\rho_i = \frac{\mu_i^s \Delta z}{\mu_i^s \Delta z + 1}, \tag{5.5}$$

$$\tau_i = \frac{1}{\mu_i^s \Delta z + 1}. \tag{5.6}$$

For a non-scattering glaze, *i.e.*, $\mu_i^s = 0$, the Beer-Lambert law applies (Equation 2.10). Without scattering, there is no mechanism by which light may be reflected. Hence, the reflectance and transmittance of such a layer reduces to [63]

$$\rho_i = 0, \tag{5.7}$$

$$\tau_i = e^{-\mu_i^a \Delta z}. \tag{5.8}$$

Note also that the above equations use a ground reflectance of zero. Therefore, they only account for reflection within layer i and not for reflection due to subsequent transmission through layer i after reflection from another layer or from the ground. Additionally, we define $\rho_{-1} = 0$ to be the reflectance of the infinite, non-scattering layer representing the ambient medium, and we define $\rho_N = \rho^*$ to be the ground reflectance.

5.2.2 System of Equations

Let $E_i^d = E^d(i\Delta z)$, $E_i^u = E^u(i\Delta z)$, for $0 \leq i \leq N$, denote the upward and downward irradiances at each layer boundary. These values may be expressed in terms of the reflectances and transmittances of the adjacent layers using the following system of equations:

$$E_0^d = E_0 \tag{5.9}$$

$$E_i^u = \rho_i E_i^d + \tau_i E_{i+1}^u \qquad\qquad 0 \leq i < N \tag{5.10}$$

$$E_i^d = \tau_{i-1} E_{i-1}^d + \rho_{i-1} E_i^u \qquad\qquad 0 < i \leq N \tag{5.11}$$

$$E_N^u = \rho_N E_N^d. \tag{5.12}$$

We remark that the reflectances, ρ_i, and transmittances, τ_i, are exact for a finite, uniform layer [62], as they were determined by integrating Equations 4.20 and 4.21. There is, therefore, no discretization error in this system of equations for the initial state (*i.e.*, at time $t = 0$). Discretization error will be introduced as the simulation proceeds because average absorption and scattering coefficients are used for each layer, whereas layers would become non-uniform in reality as fading progresses. This is discussed further in Chapter 9.

This system of equations may be expressed in matrix form as

$$\mathbf{E} = \mathbf{M}\mathbf{E} + \mathbf{E}_0, \tag{5.13}$$

where $\mathbf{E}$ and $\mathbf{E}_0$ are $2(N+1)$-dimensional vectors given by

$$\mathbf{E} = \left(E_0^u, E_0^d, \ldots, E_N^u, E_N^d \right)^T, \tag{5.14}$$

$$\mathbf{E}_0 = (0, E_0, 0, \ldots, 0)^T, \tag{5.15}$$

and $\mathbf{M}$ is a $2(N+1) \times 2(N+1)$ block tridiagonal matrix

$$\mathbf{M} = \begin{pmatrix} \mathbf{R}_0 & \mathbf{T}_0^u & & 0 \\ \mathbf{T}_0^d & \ddots & \ddots & \\ & \ddots & \ddots & \mathbf{T}_{N-1}^u \\ 0 & & \mathbf{T}_{N-1}^d & \mathbf{R}_N \end{pmatrix} \tag{5.16}$$

having 2×2 blocks

$$\mathbf{R}_i = \begin{pmatrix} 0 & \rho_i \\ \rho_{i-1} & 0 \end{pmatrix} \qquad\qquad 0 \le i \le N, \tag{5.17}$$

$$\mathbf{T}_i^u = \begin{pmatrix} \tau_i & 0 \\ 0 & 0 \end{pmatrix} \qquad\qquad 0 \le i < N, \tag{5.18}$$

$$
\begin{pmatrix}
E_0^u \\
E_0^d \\
E_1^u \\
E_1^d \\
\vdots \\
E_{N-1}^u \\
E_{N-1}^d \\
E_N^u \\
E_N^d
\end{pmatrix}
=
\begin{pmatrix}
0 & \rho_0 & \tau_0 & 0 & & & & & \\
\rho_{-1} & 0 & 0 & 0 & & & & & \\
0 & 0 & 0 & \rho_1 & \tau_1 & 0 & & & \\
0 & \tau_0 & \rho_0 & 0 & 0 & 0 & & & \\
 & & \ddots & \ddots & & \ddots & & & \\
 & & & 0 & 0 & 0 & \rho_{N-1} & \tau_{N-1} & 0 \\
 & & & 0 & \tau_{N-2} & \rho_{N-2} & 0 & 0 & 0 \\
 & & & & & 0 & 0 & 0 & \rho_N \\
 & & & & & 0 & \tau_{N-1} & \rho_{N-1} & 0
\end{pmatrix}
\begin{pmatrix}
E_0^u \\
E_0^d \\
E_1^u \\
E_1^d \\
\vdots \\
E_{N-1}^u \\
E_{N-1}^d \\
E_N^u \\
E_N^d
\end{pmatrix}
+
\begin{pmatrix}
0 \\
E_0 \\
0 \\
0 \\
\vdots \\
0 \\
0 \\
0 \\
0
\end{pmatrix}
$$

Figure 5.3: The block tridiagonal system of equations, with blocks of 2×2, describing the radiant flux densities at each of the layer boundaries resulting from irradiance E_0 from above. Note that E_i^u and E_i^d represent the upward and downward radiant flux density of the ith layer boundary, and that ρ_i and τ_i represent the reflectance and transmittance of the ith layer.

$$
\mathbf{T}_i^d = \begin{pmatrix} 0 & 0 \\ 0 & \tau_i \end{pmatrix} \qquad\qquad 0 \leq i < N. \tag{5.19}
$$

The entire structure of this matrix equation is depicted in Figure 5.3.

5.2.3 Markov Chain Representation

We remark that this system may be represented by a Markov chain [75]: a sequence of discrete random variables X_j, $j \in \mathbb{N}$, having the property that each element of the sequence depends only on the element immediately preceding it. That is,

$$
\Pr\left(X_{n+1} = x \mid X_0 = x_0, X_1 = x_1, \ldots, X_n = x_n\right) = \Pr\left(X_{n+1} = x \mid X_n = x_n\right). \tag{5.20}
$$
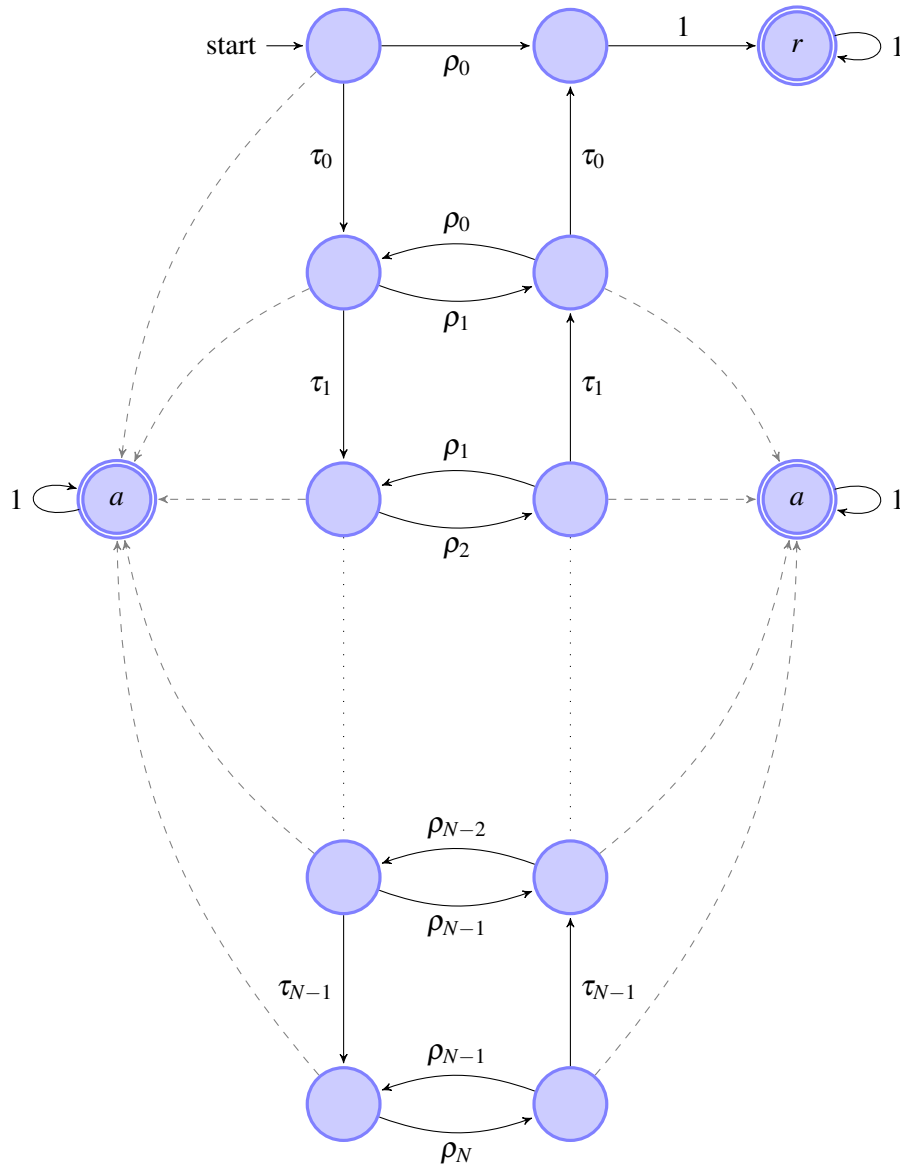
Figure 5.4: The state diagram for a Markov chain representing the two-flux system of equations. The left column of states represents downwelling flux, and the right column of states represents the upwelling flux. Each row of states represents flux passing through a particular layer boundary. The transitions between the transient states represent reflection and transmission through the adjacent layers. State r represents light reflected from the medium as a whole. State a represents absorbed light (it is shown twice for clarity). The probabilities (not shown) associated with the dashed transitions are sufficient to ensure that the sum of the outgoing transition probabilities for each node is 1.

The corresponding state transition diagram is depicted in Figure 5.4. The states represent a combination of a layer boundary and a direction (upwelling or downwelling). The transitions represent reflection, transmission, or absorption by the adjacent layers, although those for the latter do not appear explicitly in the system of equations depicted in Figure 5.3.

Absorbing and Transient States

A state within a Markov chain is called *absorbing* if there is no way to leave it [33]. That is, a state is absorbing if the only transition is a self-loop having a transition probability of 1. There are two absorbing states in the Markov chain shown in Figure 5.4: state r representing light reflected from the medium as a whole, and state a having transitions representing light that is absorbed within a layer (note the differing uses for the term *absorption*). Non-absorbing states are called *transient*. The transient states in Figure 5.4 include all of the states representing downwelling and upwelling flux at each layer boundary.

Absorbing Markov Chains

An *absorbing Markov chain* is a Markov chain which [33]

1. has at least one absorbing state, AND

2. for every transient state, there is a non-zero probability of reaching an absorbing state in one or more transitions.

As is evident from Figure 5.4, a Markov chain having this structure will be absorbing so long as there do not exist two layers having unit reflectance separated by zero or more layers having zero absorptance. That is, such a Markov chain will be absorbing unless there are two layers i and j (with $0 \leq i < j \leq N$) such that $\rho_i = \rho_j = 1$ and for which $\rho_k + \tau_k = 1$ whenever $i < k < j$. To see this, observe that if there are no two such layers, then one of the following statements must hold:

1. There are no layers having unit reflectance,
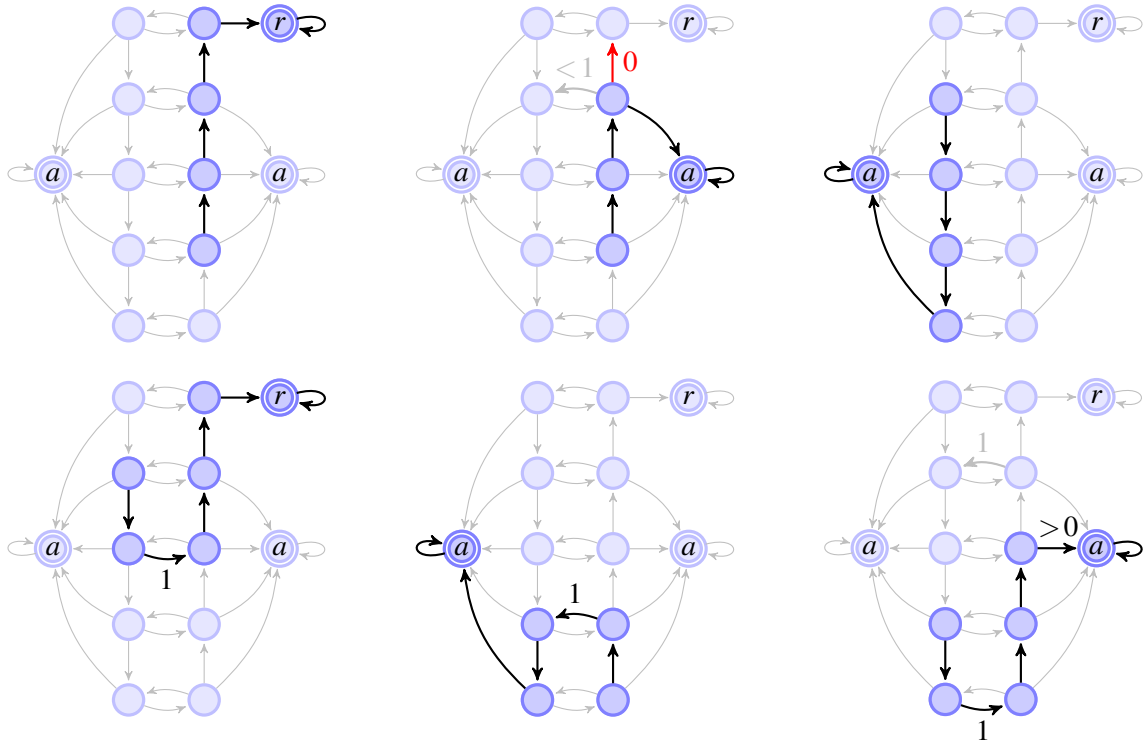
Figure 5.5: Example paths to the absorbing states within a Markov chain having the form depicted in Figure 5.4. *Top Left:* An uninterrupted upward path ending at state *r*. *Top Middle:* An upward path is interrupted by a layer having zero transmittance. Since the reflectance is less than one, we may transition to state *a* at this point. *Top Right:* An uninterrupted downward path is absorbed at the bottom layer. *Bottom Left:* A downward path is reflected upward with unit probability and reaches state *r*. *Bottom Middle:* An upward path is reflected downward with unit probability and reaches state *a* from the bottom layer. *Bottom Right:* Starting from a state between two perfectly reflective layers, we may reach state *a* from an intervening layer having non-zero absorptance.

2. There is one layer having unit reflectance, OR

3. There are two or more layers having unit reflectance, but for any pair of such layers there is a layer in between with non-zero absorptance.

If (1) holds, then state *r* may be reached from any upwelling state by means of transmission through each layer (Figure 5.5, *Top Left*). If a layer is encountered along this path with $\tau_i = 0$, then state *a* may be reached from this state since $\rho_i + \tau_i < 1$ by supposition (Figure 5.5, *Top Middle*). Since $\rho_N < 1$, state *a* may likewise be reached from all downwelling states via the transition from the

bottom downwelling state to *a* (Figure 5.5, *Top Right*).

If (2) holds, suppose that $\rho_j = 1$. Upwelling states $i \le j$ and downwelling states $i \ge j$ may be treated in an identical manner as for (1). State *r* is reachable from downwelling states $i \le j$ by means of downward transmission toward state *j*, reflection at layer *j*, and then upward transmission toward state *r* (Figure 5.5, *Bottom Left*). Likewise, state *a* is reachable from any upwelling state $i \ge j$ via reflection at state *j* and absorption from layer *N* (Figure 5.5, *Bottom Middle*).

If (3) holds, any states outside a pair of perfectly reflective layers may be treated in the same manner as for (1) or (2). State *a* may be reached from any state in between two perfectly reflective layers via the supposed layer having non-zero absorptance (Figure 5.5, *Bottom Right*).

Under the Kubelka-Munk formulation described in Chapter 4, the reflectance of layer of finite thickness is always less than 1 [63]. The ground reflectance, ρ_N, may be 1. Hence, the two-flux system falls into category (1) or (2). The corresponding Markov chain is therefore absorbing.

The Fundamental Matrix

Consider an absorbing Markov chain having *n* transient states and *m* absorbing states. Let **T** be the $n \times n$ matrix of transition probabilities between the transient states, and let **A** be the $n \times m$ matrix of transition probabilities from the transient states to the absorbing states. Note that the matrix of transition probabilities among the absorbing states is the $m \times m$ identity matrix. The full transition matrix for this Markov chain is

$$\mathbf{B} = \begin{pmatrix} \mathbf{T} & \mathbf{A} \\ \mathbf{0} & \mathbf{I} \end{pmatrix}. \tag{5.21}$$

The matrix $\mathbf{I} - \mathbf{T}$ for an absorbing Markov chain is non-singular [33] and its inverse,

$$\mathbf{N} = \sum_{k=0}^{\infty} \mathbf{T}^k = (\mathbf{I} - \mathbf{T})^{-1}, \tag{5.22}$$

is called the *fundamental matrix* of the absorbing Markov chain [33]. This result follows from the fact that $\mathbf{U} = \mathbf{I} - \mathbf{T}$ has the following properties [88]:

- $\mathbf{U}$ is diagonally dominant (albeit not necessarily strict), as $\rho_i + \tau_i \leq 1$ for each row i, and

- for any row i for which dominance is not strict (*i.e.*, $\rho_i + \tau_i = 1$), there exists a row j for which the dominance is strict (*i.e.*, $\rho_j + \tau_j < 1$) and a sequence of rows $i_1, i_2, \ldots, i_n$ for which $\mathbf{U}_{ii_1}, \mathbf{U}_{i_1 i_2}, \ldots, \mathbf{U}_{i_n j}$ are all non-zero. This corresponds to a path through the Markov chain with non-zero probability ending at an absorbing state.

5.2.4   Existence of a Solution

We can solve for $\mathbf{E}$ by rearranging Equation 5.13 to obtain

$$\mathbf{E} = (\mathbf{I} - \mathbf{M})^{-1} \mathbf{E}_0. \tag{5.23}$$

Observe that $\mathbf{M}$ is the matrix of transition probabilities among the transient states of the absorbing Markov chain depicted in Figure 5.4. Hence, a unique solution for $\mathbf{E}$ exists as $\mathbf{I} - \mathbf{M}$ is non-singular.

5.2.5   Computational Complexity

Furthermore, the block tridiagonal structure of this system allows for it to be solved in $O(N)$ time [48] rather than the $O(N^3)$ time required for a general system of linear equations.

5.2.6   Fluence Rate Estimation

The fluence rates at the layer boundaries are given by $\mathbf{F} = \mathbf{E}^d + \mathbf{E}^u$. The mean fluence rate within layer i is estimated by taking the average of the fluence rates at the boundaries:

$$F_i = \frac{1}{2}\left(\mathbf{F}_i + \mathbf{F}_{i+1}\right).$$

We remark that the spectral fluence rate F_λ may be computed independently for each wavelength.

5.3 Time Stepping

Time stepping proceeds by solving Equation 4.37 while holding the fluence rate constant within each layer. The absorption coefficients are then updated according to

$$f(t + \Delta t) = f(t) \exp \left(-\Delta t \int_0^\infty \beta \mu^a F_\lambda \, d\lambda \right). \tag{5.24}$$

The spectral fluence rate F_λ is computed for a fixed set of wavelengths using the procedure described in the previous section. The absorption coefficient μ^a is sampled at the same set of wavelengths. The result is then integrated numerically. Finally, the absorption coefficient may be updated according to

$$\mu^a(t + \Delta t) = \frac{f(t + \Delta t)}{f(t)} \mu^a(t). \tag{5.25}$$

5.4 Summary

In the preceding, we have seen that the system of equations arising from introducing time as a parameter into the rendering equations cannot be solved analytically, even for the relatively simple single-flux and two-flux models. We have developed numerical techniques for solving these systems of equations, which involve discretizing the domain along the spatial and temporal dimensions. A solution is found for each dimension in turn, and this is iterated over to produce the progression of appearance changes over time. Next, we shall examine the effectiveness of this approach for predicting the progression of appearance changes over time due to light exposure, and we will investigate the performance characteristics of the proposed techniques.

Chapter 6

Evaluation Procedures

In this chapter, we describe our evaluation approach in which we compare measured and simulated reflectance curves obtained as fading takes place over an extended period of time. Several sets of experiments were conducted subjecting various materials to light exposure over time. The materials selected for experimentation included 30 lb (48.8 g m^{-2}) newsprint paper (70 μm thick), two dyes (Toluidine Blue O and Congo Red), and a fine grain cork (typically used for bulletin boards). Square samples were prepared and affixed to a piece of bristol board with two-sided tape around the edges of each sample to prevent them from curling during exposure, thus maintaining a consistent distance and orientation with respect to the light source.

The samples were exposed to light from a 27 W fluorescent bulb. This type of lamp was selected to minimize the effects of heat as a cause of fading. The spectral power distribution of the bulb is depicted in Figure 6.1.

Reflectance measurements were taken before exposure, after every six hours of exposure up to twenty-four hours, and after every twenty-four hours thereafter up to seven days. Measurements were performed using a StellarNet Inc. BLK-C-SR spectrophotometer with a SL1-Filter Tungsten/Krypton lamp. Although the measured values presented some quantitative variability due to the handling of heterogeneous sample materials (Figure 6.2), the dominant spectral trends in the progression of reflectance curves were fully preserved. This is an essential evaluation requisite since
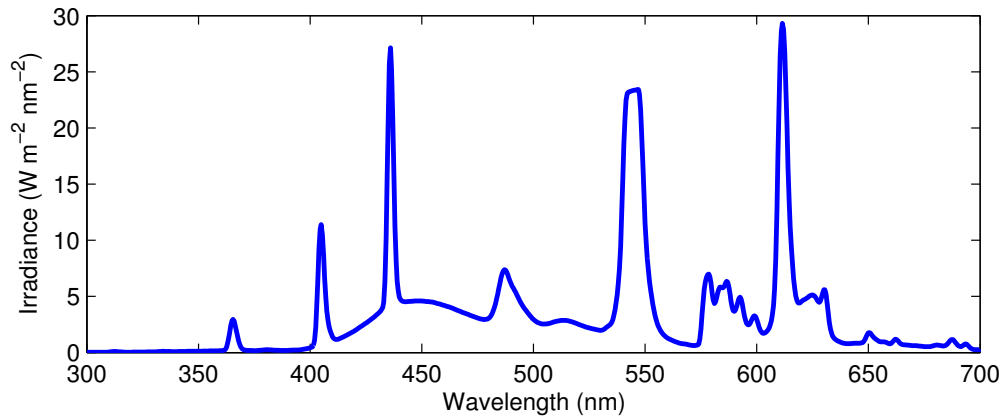
Figure 6.1: Spectral irradiance of the 27 W fluorescent light bulb used in the experiments as measured from $5/8$ inches from the center of the bulb (the distance from which the samples were illuminated).
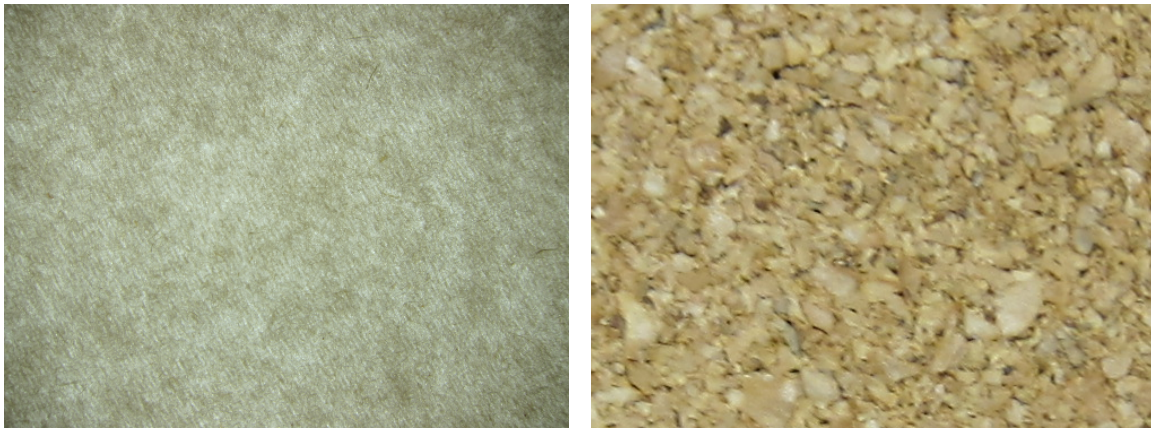
Figure 6.2: Photographs depicting the heterogeneous structure of the materials used in the experiments: *Left*: Newsprint, *Right*: Cork.

the main purpose of these experiments was to provide spectral references for assessing whether the proposed framework can capture different fading behaviors.

6.1 Paper

Reflectance measurements over black and over white substrates were taken of the unexposed sample in order to determine separately the initial scattering and absorption coefficients of the newsprint,
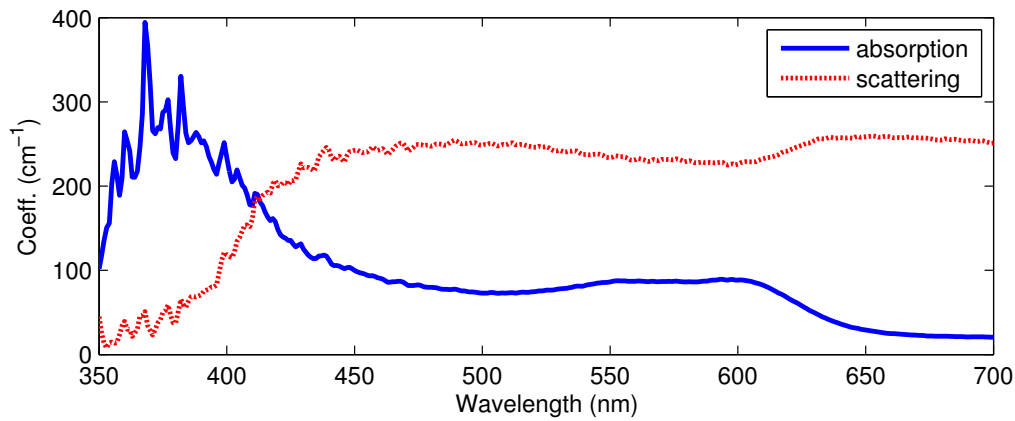
Figure 6.3: Scattering and absorption coefficients of the newsprint used in our experiments.
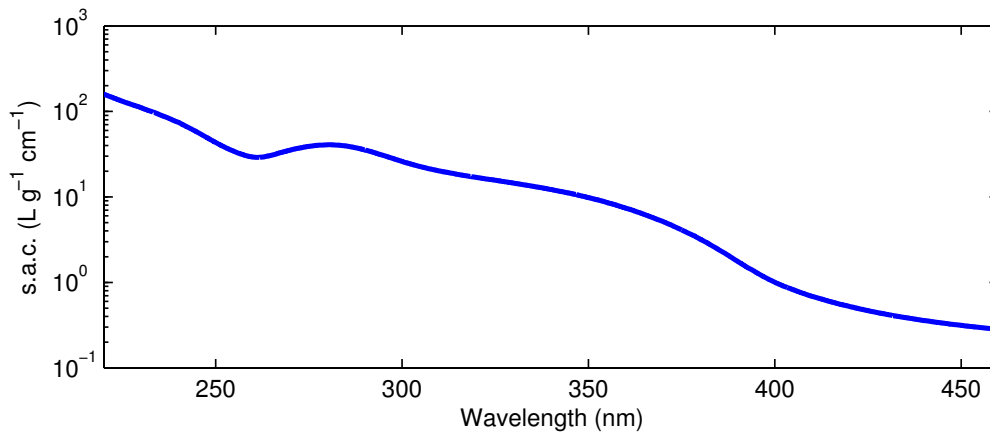
Figure 6.4: Specific absorption coefficient (s.a.c.) of lignin [Glading 1940].

depicted in Figure 6.3, using the method described in Appendix A. The initial absorption coefficient was separated into a component for lignin and a component for the remaining constituents. The lignin content of newsprint is similar to that of the wood from which it was produced, which typically falls in the range of 20-27% [81]. The midpoint of this range was used in our simulations. The specific absorption coefficient of lignin [30] is shown in Figure 6.4 (*Left*).   Further, it was assumed that absorption by lignin produced a chromatic breakdown product, whereas other substances broke down to a non-absorbing material. The absorption coefficient of the breakdown products resulting from absorption by lignin was determined by exposing a sample of newsprint
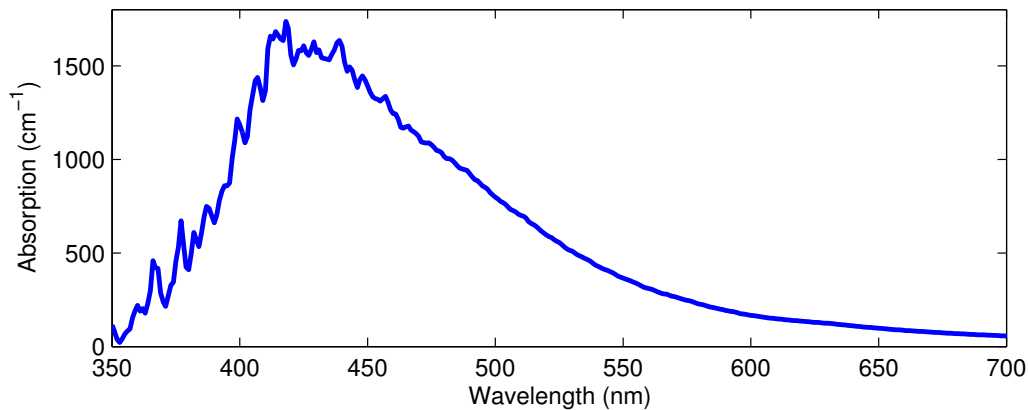
Figure 6.5: Absorption coefficient of the fully yellowed newsprint used in our experiments.

on both sides for long enough to allow the sample to completely yellow. The absorption coefficient was then computed from the reflectance measurement under the assumption that the scattering coefficient was unaffected (Figure 6.5).

6.2 Dyes

Solutions of the dyes (Toluidine Blue O and Congo Red) in water were prepared in test tubes. Squares of newsprint paper were cut. Samples were prepared for each solution by pouring the solution into a petri dish and soaking one of the squares until the solution penetrated the paper. The samples were hung vertically in a dark environment to dry. Since the pigmented samples were too dark to allow for incomplete hiding of the substrate, we have assumed that the pigments themselves contribute only to absorption, eliminating the requirement for separate reflectance measurements over black and over white substrates.

6.3 Cork

A $^1/_{32}$ inch (0.8 mm) thick sample of fine grain cork was used. Due to the infeasibility of obtaining a cork sample thin enough for reflectance measurements with incomplete hiding, only a single

reflectance measurement was taken before light exposure and after each time interval. Thus, only the ratio of the absorption and scattering coefficients may be obtained. In our simulations, we used the average specific scattering coefficient over the visible region of the spectrum measured from the newsprint ($237\,\mathrm{L\,g^{-1}\,cm^{-1}}$) as an approximation of the scattering from cork. Cork contains approximately 22.7% lignin by weight [79]. The absorption coefficient used was therefore expressed as a sum of the absorption coefficient for this concentration of lignin and the remaining constituents, which were assumed to break down into a colourless product.

6.4 Summary

In the preceding chapter, we have outlined the procedures used to measure the progression of spectral reflectance curves during an extended period of exposure and to compare these measurements with simulated reflectance curves. In the following chapters, we will discuss particular challenges that had to be overcome, provide an analysis of the experimental results and examples of rendered scenes, as well as describe the performance characteristics of the model derived from our framework.

Chapter 7

Measurement Challenges

> Good science requires both theory and
> data. One is of little use without the other.
>
> ―――――――――――――――――――
> Gregory J. Ward [100]

In this chapter, we outline the measurement procedures used to obtain the data employed in the evaluation of the model described in the preceding chapters. We describe the challenges involved in obtaining these measured data and discuss the techniques used to overcome them. In Section 7.1, we describe the procedures used in preparing the samples to be subjected to light exposure. In Section 7.2, we outline the light sources used. In Section 7.3, we discuss the experimental procedures used to subject these samples to light exposure. In Section 7.4, we describe the equipment and procedures used to measure the reflectance characteristics of the samples.

In the following, it should be remembered that a typical experiment trial required approximately two weeks. This includes seven days (168 hours) of cumulative exposure time, plus additional time between periods of exposure to remove the samples to obtain reflectance measurements. As a consequence, it was often the case that each time one of the challenges detailed below was discovered, two weeks worth of measurements had to be redone. This does not include additional time that was often required to design and develop a solution to mitigate the problem that was discovered.

7.1 Sample Preparation

Several samples were prepared for experimentation. These included different types of pigments and dyes, as well as different types of paper, and other materials such as cork. These samples had to be carefully prepared to match, as closely as possible, the initial conditions assumed in the evaluation of the model developed in Chapter 5. For the purposes of evaluation, we had assumed that the absorption and scattering coefficients were initially uniform throughout the depth of the specimen.

For cork, no additional preparation was necessary. Although the cork samples had some variability in their appearance in the horizontal directions, they could be considered uniform with respect to depth (to the extent that light would be able to penetrate them) due to their sufficiently high optical density. Non-dyed samples of paper were similarly assumed to be initially uniform in their absorption and scattering characteristics.

Paper samples treated with pigments or dyes had to be prepared in a manner so as to ensure that the concentration of the colourant was uniform throughout. This was generally accomplished by soaking the paper in the colourant until it appeared the same from both sides.

7.1.1 Sample Selection

In the evaluation described in Chapter 6, we used newsprint dyed with Toluidine Blue O and with Congo Red. Several other combinations of pigments and dyes were attempted prior to this.

For example, in early experiments, we exposed samples of marker ink to a fluorescent lamp as depicted in Figure 7.1. As depicted in this figure, the pink marker was more susceptible to light exposure than the others. These samples, however, were not sufficiently large in order to have their reflectance measured using the equipment we had available to us at the time. We therefore prepared a larger sample using the pink marker in order to obtain a progression of reflectance measurements during the course of light exposure as shown in Figure 7.2. With this marker sample, however, it was discovered from the progression of spectral reflectance curves that the ink consisted of a mixture of at least two colourants that faded at different rates. Commercial pigments, such as these marker
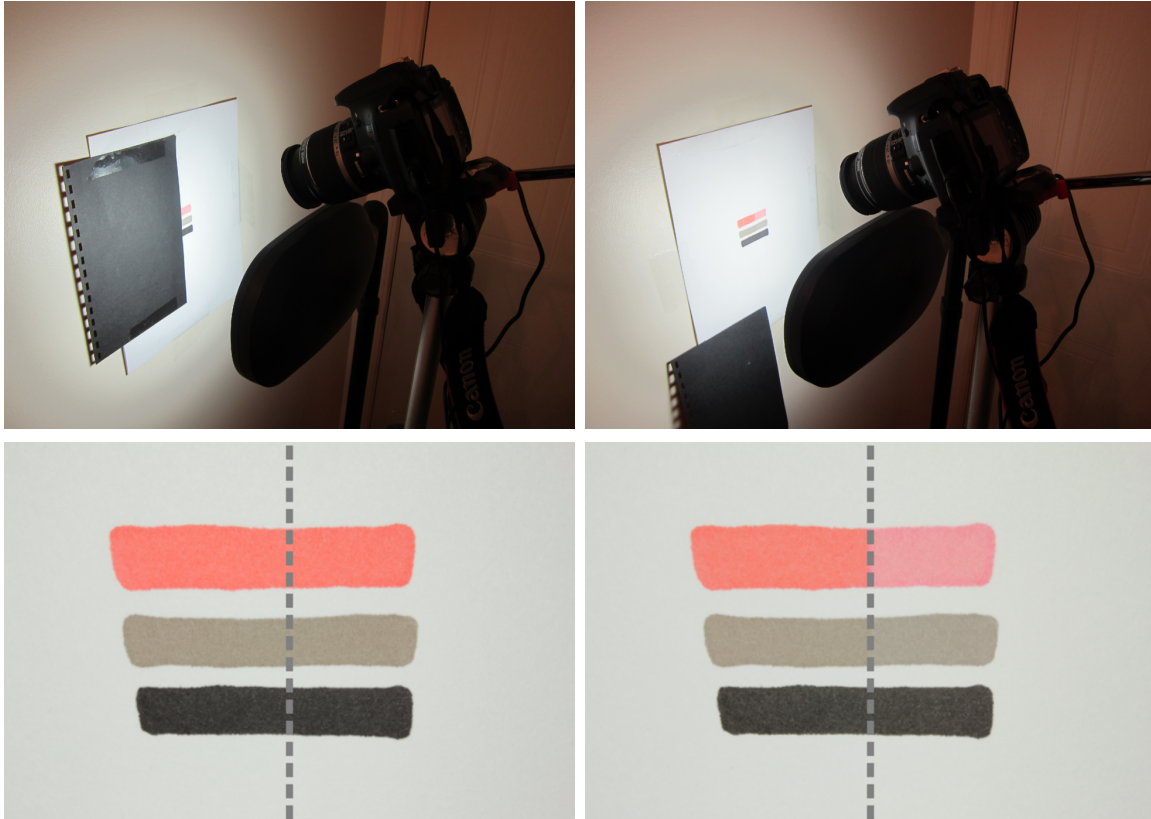
Figure 7.1: Three marker samples exposed to light from a fluorescent lamp. *Top Left:* Half of the samples were covered in order to evaluate the effect of the light exposure on the sample. *Top Right:* After exposure, the unexposed side is revealed. *Bottom Left:* A close-up of the marker samples prior to light exposure. The dashed line separates the unexposed area (left side) from area to be exposed (right side). *Bottom Right:* A close-up of the marker samples after exposure. There is considerable variability in the degree of lightfastness among these samples.
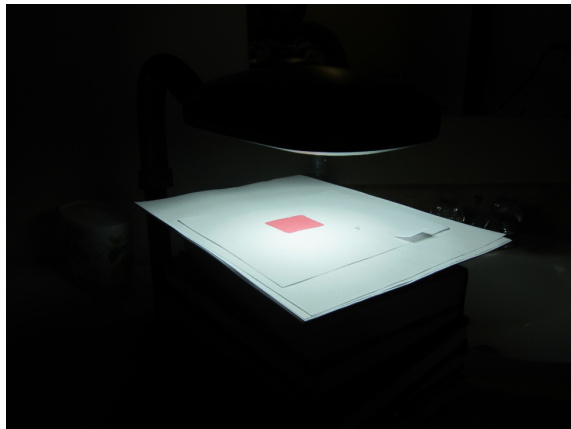
Figure 7.2: A larger sample was prepared using one of the markers in order to obtain a progression of reflectance measurements during the course of light exposure.

inks, are often manufactured from a combination of a number of other pigments and dyes. The component pigments used and their precise ratios are not typically disclosed, making it difficult to distinguish the fading behaviors of the component pigments during an experiment.

For later experiments, we selected several additional pigments and dyes. Since we now had more samples than could be exposed simultaneously by the lamp used in our initial experiments, we employed fluorescent tube lamps as shown in Figure 7.5. Here, it was evident that without securing the samples to the backing, the paper tended to curl during exposure. Although we could flatten the specimen during measurement, as depicted in Figure 7.6, this often was not sufficient to reduce the variability in the reflectance measurement. This is because the small samples required that the reflectance probe be placed very close to the specimen. With this setup, even a small variation in the distance between the sample in the probe could affect the measurement. Furthermore, the curling of the specimen would result in an increased irradiance impinging on the specimen where the paper had been closer to the light source.

To address these problems, we prepared larger samples and affixed them to a strip of bristol board prior to exposure as shown in Figure 7.7. By using larger samples, the probe could be held further away from the specimen, reducing the sensitivity of the measurements to the precise distance between the specimen and the probe. Since the samples were held flat during the course of the
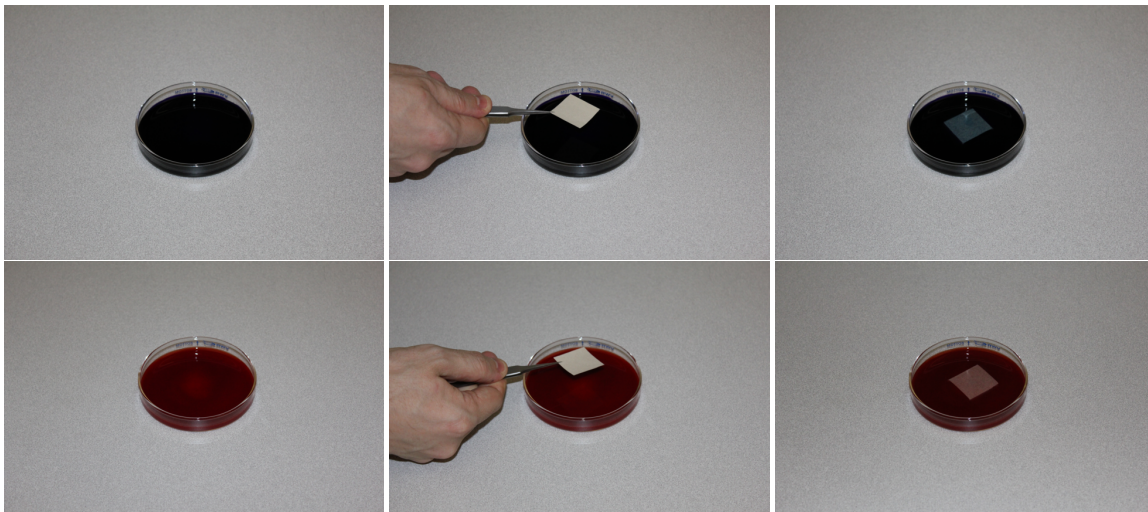
Figure 7.3: Preparation of samples of newsprint dyed with Toluidine Blue O (*top row*) and with Congo Red (*bottom row*). *Left:* A solution of the dye in water is prepared. *Middle:* A newsprint sample is placed in the solution. *Right:* The sample is left in the newsprint until the dye soaks through the paper.

Figure 7.4: Paper samples soaked in pigment or in dye solutions are hung to dry in order to ensure that the colourant does not settle toward one face of the paper.
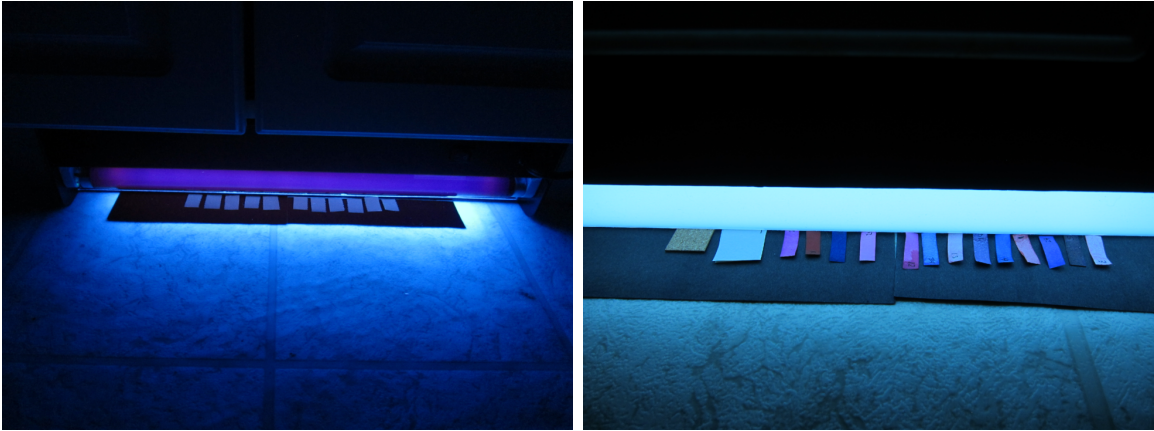
Figure 7.5: Several specimens exposed to light from fluorescent tube lamps. *Left:* Newsprint samples exposed to an ultraviolet blacklight. *Right:* A variety of samples exposed to a standard fluorescent tube.
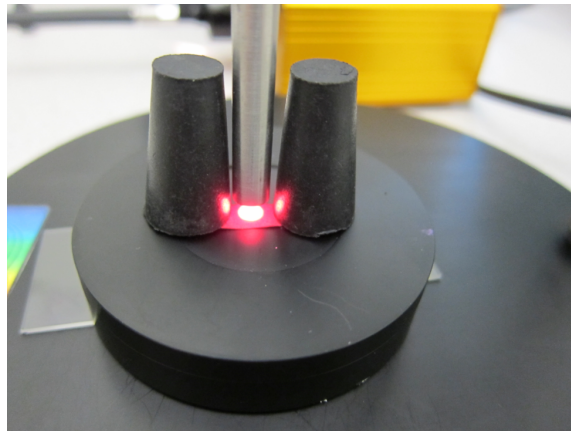
Figure 7.6: A specimen is held flat while measuring its reflectance by placing two weights on either end of the strip.
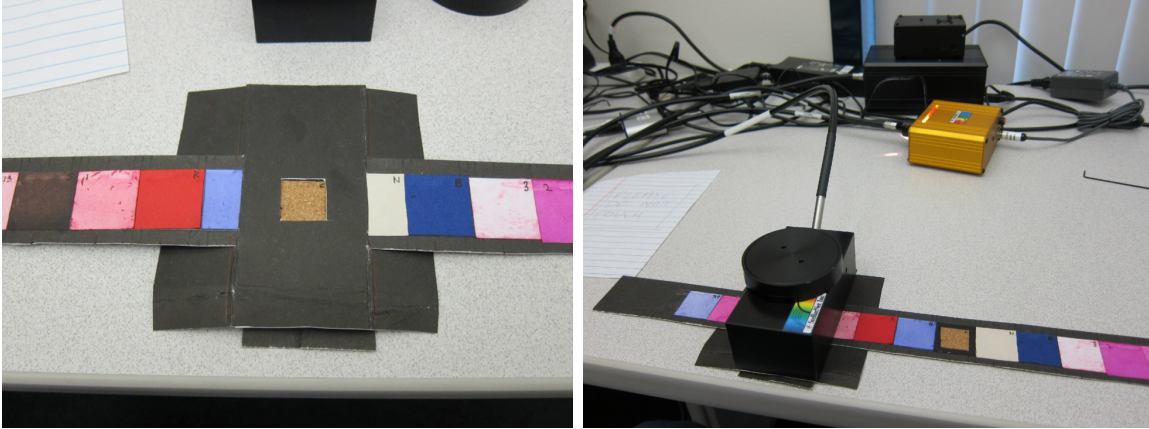
Figure 7.7: Several specimens were prepared and affixed to a strip of bristol board prior to exposure. *Left:* A close-up is shown of the strip of specimens, along with a mask used to prevent reflectance measurements from being influenced by adjacent samples. *Right:* The reflectance of one of the samples is being measured.

experiment, the irradiance impinging on the specimens remained consistent over time. During this round of experiments, however, several other challenges were revealed. Many of the samples did not show significant fading even after the full seven days of exposure.

Additionally, for some samples, the pigment did not apply evenly across the area of the paper. Note that, since the specimen had to be removed from under the light source in order to measure its reflectance, there was some variation in the exact position of the specimen being measured. Thus, even if the pigment concentration did not vary with depth at any particular point, this unevenness could give rise to considerable variability in reflectance measurements.

Finally, standard printer paper is treated with fluorescent dyes in order to appear brighter under typical indoor lighting. This was found to have an influence during exposure, as depicted in Figure 7.8. For this reason, only specimens using newsprint paper were retained. Those using printer paper were discarded.
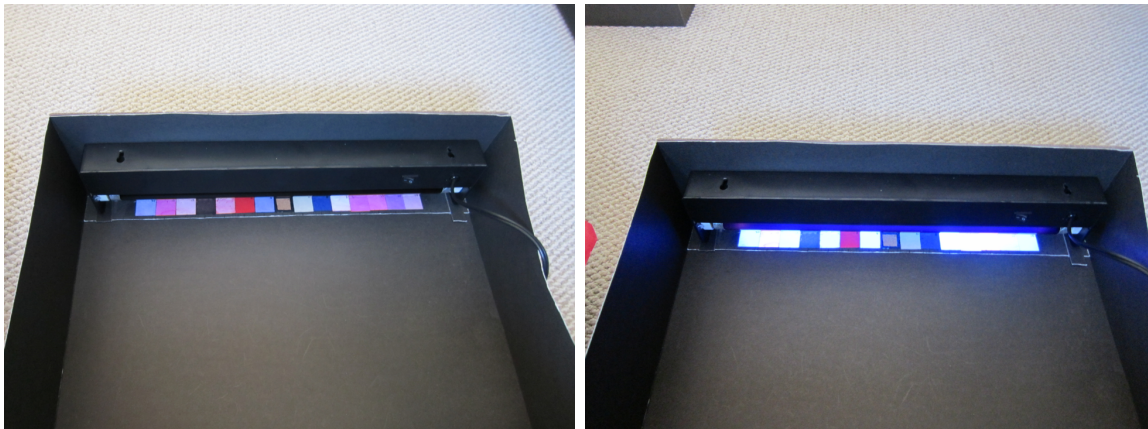
Figure 7.8: Several specimens under a fluorescent lamp, which emits some light in the ultraviolet region. Fluorescence was found to have an effect during exposure of the samples employing printer paper, which is often treated with fluorescent dyes in order to appear brighter under typical lighting conditions. *Left:* The lamp is off, revealing the appearance of the specimens under normal conditions. *Right:* The lamp is on. Many of the samples fluoresce under exposure to the lamp.

7.2   Light Sources

For a light source to be useful for these experiments, it must emit light with sufficient power at wavelengths which the colourant will absorb and which will be effective at inducing fading. Furthermore, in order to minimize the effects of heat as a potential cause of fading, we must either employ a light source that radiates little heat, or place the specimen far away from the light source.

Initially, we worked with incandescent lamps placed far away from the specimen as shown in Figure 7.9 (*Left*). Such lamps emit light primarily at longer (*i.e.*, lower energy) wavelengths, and emit very little in the ultraviolet. Thus, these lamps were not very effective at inducing fading in the specimens used. A halogen lamp was also employed as seen in Figure 7.9 (*Right*). This lamp was much brighter overall. Although it still emitted primarily at longer wavelengths, there was some emission in the ultraviolet.

Fluorescent lamps were found to have prominent emission bands in the ultraviolet region of the spectrum, and were more effective at inducing fading as a result. They also radiated much less heat, allowing for more flexibility in positioning the light source. Fluorescent tubes may be uneven across the length of the bulb, particularly at the ends, as may be observed in Figure 7.10.
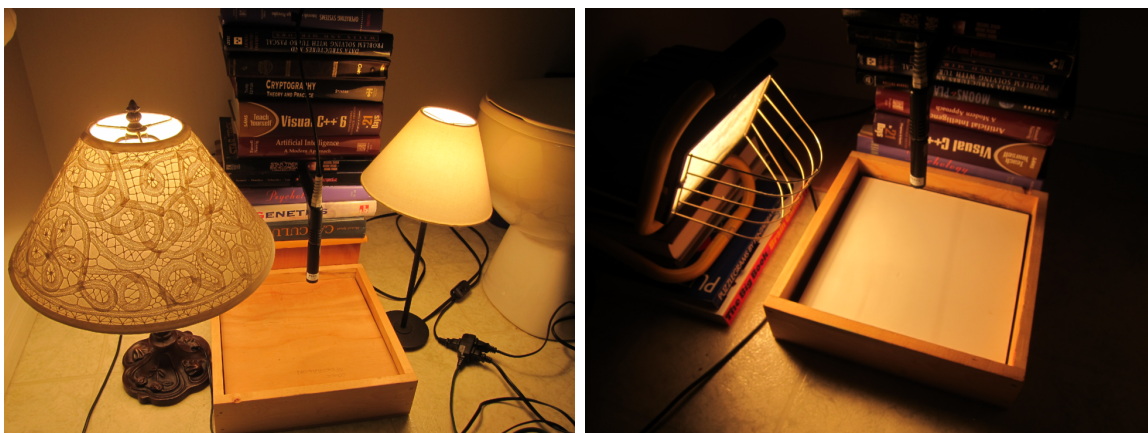
Figure 7.9: Light sources used in early experiments. These lamps radiate a lot of heat, and therefore needed to be placed far away from the sample to minimize the influence of this heat on fading. They also emit mainly at longer wavelengths, and were therefore less effective at inducing fading. *Left:* Incandescent lamps. *Right:* A halogen lamp. This lamp was brighter than the incandescent lamp, and emitted some light in the ultraviolet, although it still emitted primarily at longer wavelengths.

Figure 7.10: The emission from a fluorescent lamp may vary across the length of the bulb. Here, the bulb is dimmer at the ends of the tube.

7.3 Experimental Procedure

To minimize the influence of exposure from light sources other than the source used in the experiment, it was necessary to conduct the experiment in a room that we could keep dark. It was also necessary that we had control over the use of the room over the extended period of time needed to conduct the experiment.

In addition, we needed to ensure that the samples received consistent irradiance during periods of exposure after having been removed in order to obtain reflectance measurements. For this purpose, we made sure that the light sources were fixed in place and we used markings to ensure that the samples were returned to their positions after removal.

7.4 Measurement Equipment and Procedures

7.4.1 Sample Size

The sample size must be large enough in order to obtain an accurate measurement using the reflectance probe. How large the sample must be depends on how far away the probe is from the sample. On the other hand, the samples must be small enough in order to fit all of them under the light source.

When samples are affixed to a backing in order to prevent them from being deformed during exposure, it is necessary to ensure that reflectance measurements are not influenced by adjacent specimens. For this purpose, a mask is used to block adjacent samples, as shown in Figure 7.7 (*Left*).

The mask served as a template to ensure that, for each measurement, the reflectance probe was aimed at the same location on the surface of the sample. This ensured that differences in reflectance measurements across time intervals were due to fading, rather than due to inhomogeneity across the surface of the sample (as depicted in Figure 6.2).

Accordingly, we took a single reflectance measurement at each time interval from a point near

71
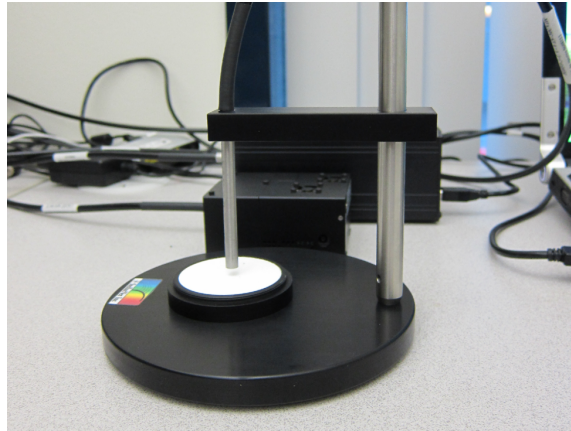
Figure 7.11: A measurement being performed using a white reflectance standard.

the center of the sample. We note that multiple measurements taken at the same location at each time interval would likely vary only in terms of the measurement device's uncertainty [4], which can be estimated to be on the order of ± 0.001 or lower [55].

7.4.2   White Reference and Dark Current

When measuring reflectance, instruments give readings in terms of raw, dimensionless *counts*. In order to obtain reflectance measurements, it is necessary to obtain white reference and dark current measurements under the same illumination and measurement conditions. To obtain a white reference measurement, a reference material is used in place of the specimen to be measured as demonstrated in Figure 7.11. The dark current measurement is obtained by blocking the light source. The reflectance is then computed as

$$\rho = \frac{x - x_{\mathrm{dc}}}{x_{\mathrm{wr}} - x_{\mathrm{dc}}}, \tag{7.1}$$

where x is the reading obtained from the sample being measured and x_{wr} and x_{dc} are the white reference and dark current readings, respectively.

Dark current readings are caused by spurious current that passes through the device when not exposed to light. This may be temperature-dependent. It is therefore important to turn on the

measurement devices, and allow them to warm up for some period of time to allow the dark current level to stabilize before conducting measurements. For early experiments, we used an Analytical Spectral Devices (ASD) spectrophotometer and found that the dark current would not be stable even after having been left on for a considerable length of time. In order to ensure the accuracy of these measurements, we would take dark current and white reference readings between each measurement. The time was recorded for each reading, and the dark current and white reference in effect while measuring the specimen was estimated by linear interpolation of the dark current and white reference readings taken before and after measurements of the specimen. The final reflectance estimate was obtained by computing the average of several such reflectance measurements.

7.5   Summary

There are several challenges that must be overcome when conducting physical experiments involving the fading of materials under exposure to light over an extended period of time. These arise from many different factors. There are challenges resulting from the difficulty of obtaining data for the pigments, dyes, and other materials used in preparing the samples to be faded. There are challenges involving sample preparation and handling, experimental setup, and involving the use of measurement equipment. Each of these factors must be addressed in order to obtain useful experimental measurements. Furthermore, the learning process is slow, as each iteration requires weeks to complete. It is our hope that the preceding discussion aids others in future research building on this work.

Chapter 8

Evaluation Outcomes and Discussion

In this chapter, we evaluate the predictive capability of the proposed algorithms. Results are presented depicting comparisons between simulations employing the numerical algorithms to measurements obtained using the procedures outlined in the preceding chapters. We also assess the phenomenological characteristics of the proposed framework, drawing comparisons with accounts from the conservation literature. Finally, we demonstrate the applicability of the proposed techniques to computer graphics through several rendered scenes depicting the fading and yellowing of materials before and after extended periods of light exposure.

The remainder of this chapter is organized as follows. Section 8.1 discusses the results of comparison between experimental and simulated results described in Chapter 6. Section 8.2 discusses the behavior of the framework and draws comparisons with the literature. In Section 8.3, we present several scenes rendered to further illustrate the applicability of our framework in realistic image synthesis. Performance characteristics will be addressed in the next chapter.

8.1 Experimental Assessment

Figure 8.1 shows the measured (*top*) and simulated (*bottom*) reflectance curves obtained from the illuminated side of the newsprint before exposure and after several periods of exposure to light from
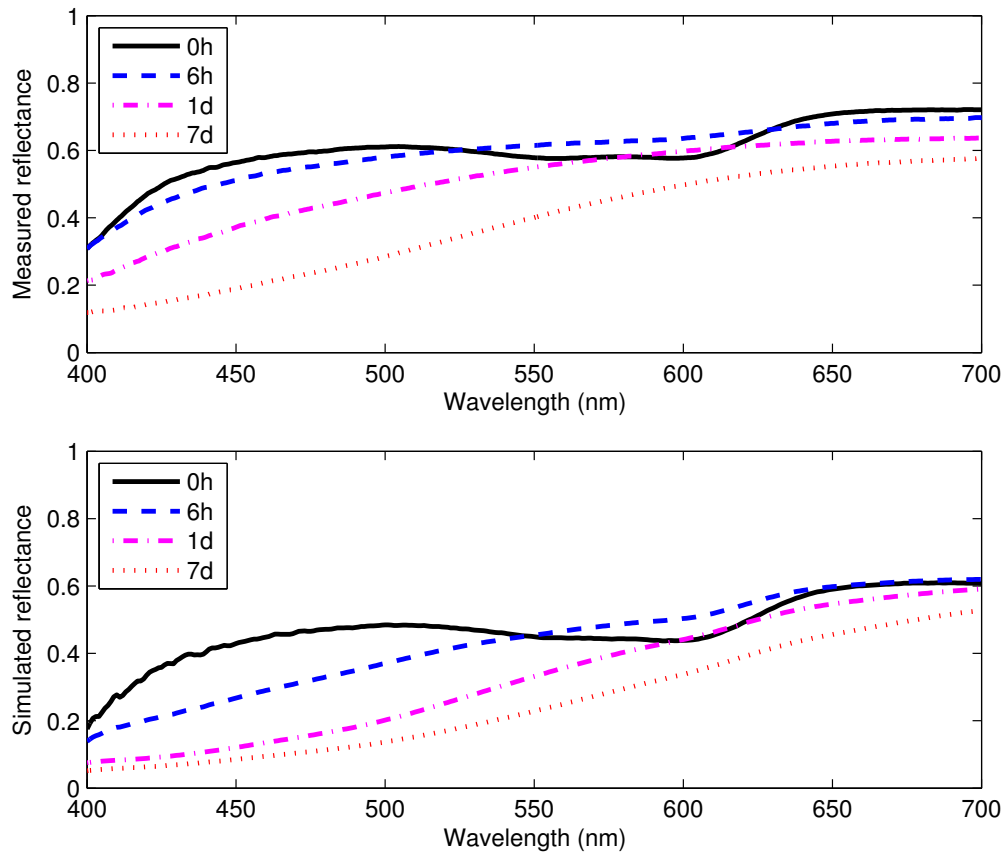
Figure 8.1: Measured and simulated reflectances of yellowing newsprint as obtained from the front (illuminated) side of the paper initially *(0h)*, after six hours *(6h)*, one day *(1d)*, and seven days *(7d)*. *Top*: Measured progression of reflectance curves. *Bottom*: Simulated progression of reflectance curves.

the fluorescent lamp. For clarity, we have selected a representative set of curves to show in the plots. Note that our framework is able to capture the simultaneous rapid fading of the absorption band between 500 and 600 nm and the darkening caused by yellowing of the lignin. We remark that the difference in the absolute level of the measured *vs.* simulated initial reflectance curves is attributable to the spatial variation in the internal structure of the newsprint, as shown in Figure 6.2 (*Left*). The fading parameters used are given in Tables 8.1 and 8.2. Table 8.3 shows timings for simulating the yellowing of newsprint on a single core of a machine with two 2.8 GHz quad core Xeon processors. Timings for other simulations were similar.
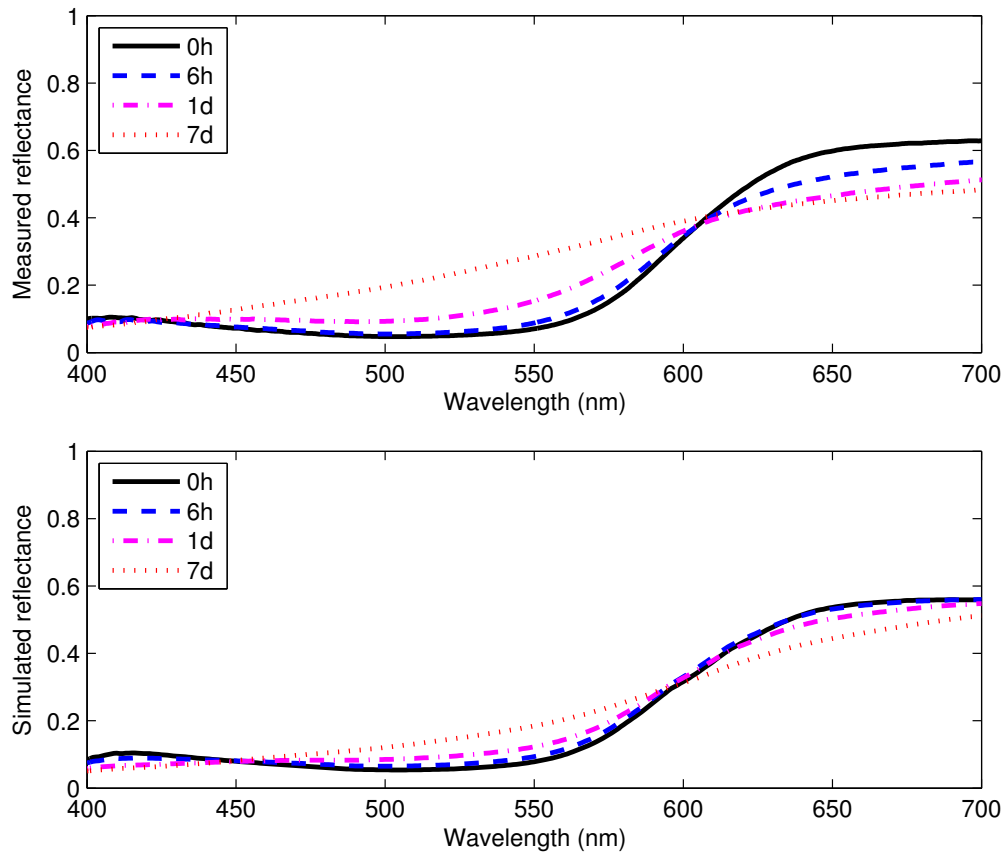
Figure 8.2: Measured and simulated reflectances of newsprint dyed with Congo Red as obtained from the front (illuminated) side of the sample initially *(0h)*, after six hours *(6h)*, one day *(1d)*, and seven days *(7d)*. *Top*: Measured progression of reflectance curves. *Bottom*: Simulated progression of reflectance curves.

Figure 8.2 shows the measured (*top*) and simulated (*bottom*) reflectance curves obtained from the front side of the newsprint dyed with Congo Red prior to exposure and after several periods of exposure to light from the fluorescent lamp. Note that the pivot point at approximately 600 nm produced by the simultaneous fading of the Congo Red dye and the yellowing of the newsprint is reproduced by our framework.

Figure 8.3 shows the measured (*top*) and simulated (*bottom*) reflectance curves obtained from the front side of the newsprint dyed with Toluidine Blue O. Note that the pivot point in the blue end of the visible spectrum is reproduced in our simulation. This is caused by the simultaneous fading
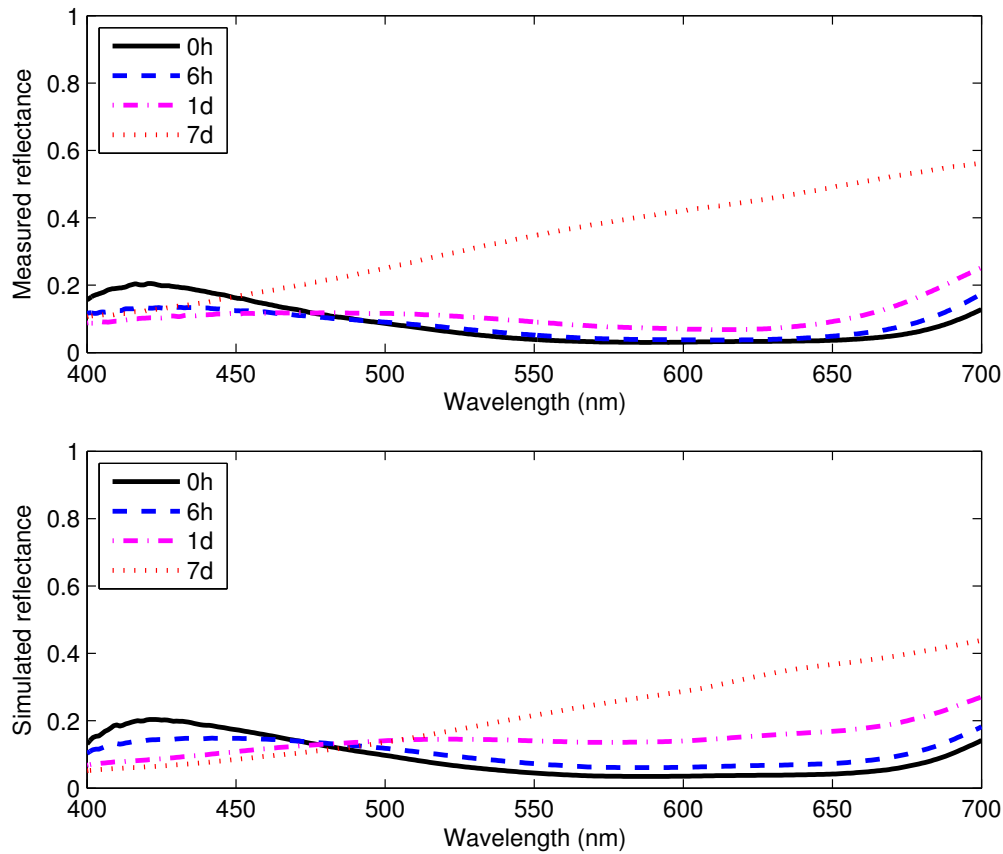
Figure 8.3: Measured and simulated reflectances of newsprint dyed with Toluidine Blue O as obtained from the front (illuminated) side of the sample initially *(0h)*, after six hours *(6h)*, one day *(1d)*, and seven days *(7d)*. *Top*: Measured progression of reflectance curves. *Bottom*: Simulated progression of reflectance curves.

of the Toluidine Blue O dye with the yellowing of the newsprint.

Figure 8.4 depicts the corresponding reflectance curves obtained from the back of the dyed newsprint samples. Note that our framework can also reproduce the preferential darkening on the red end of the spectrum on the unexposed side of the newsprint dyed with Congo Red. This is caused primarily by the spike in the spectral irradiance from the lamp in the near ultraviolet at approximately 370 nm (see Figure 6.1). In this region, the Congo Red dye absorbs very little, allowing this light to penetrate through the paper and cause yellowing through to the other side. Since the dye is highly absorbing in the visible region, however, very little light penetrates through
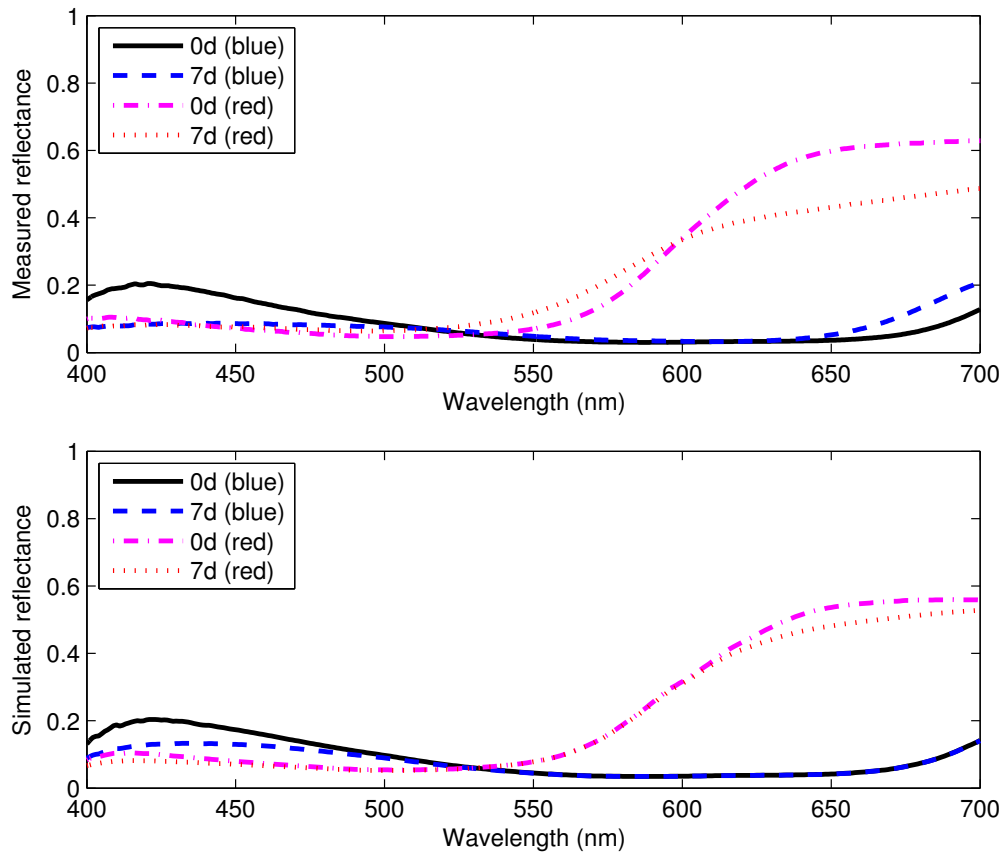
Figure 8.4: Measured and simulated reflectances of newsprint dyed with Toluidine Blue O *(blue)* and Congo Red *(red)* as obtained from the back (unilluminated) side of the sample initially *(0d)* and after seven days *(7d)*. *Top*: Measured reflectance curves. *Bottom*: Simulated reflectance curves.

the sample and there is therefore no fading seen from the unexposed side. Similarly, note the preferential darkening in the blue end of the spectrum on the unexposed side. This may be explained in a similar manner as with the red sample.

Figure 8.5 shows the measured and simulated progression of reflectance curves for cork. Note that the reflectance curve maintains its general shape while increasing in value over time. This is caused by the simultaneous yellowing of the lignin with the fading of the remaining constituents. Without yellowing of the lignin, the reflectance curves would flatten out as fading progressed. That is, fading would proceed faster in the blue end of the spectrum than in the red end.
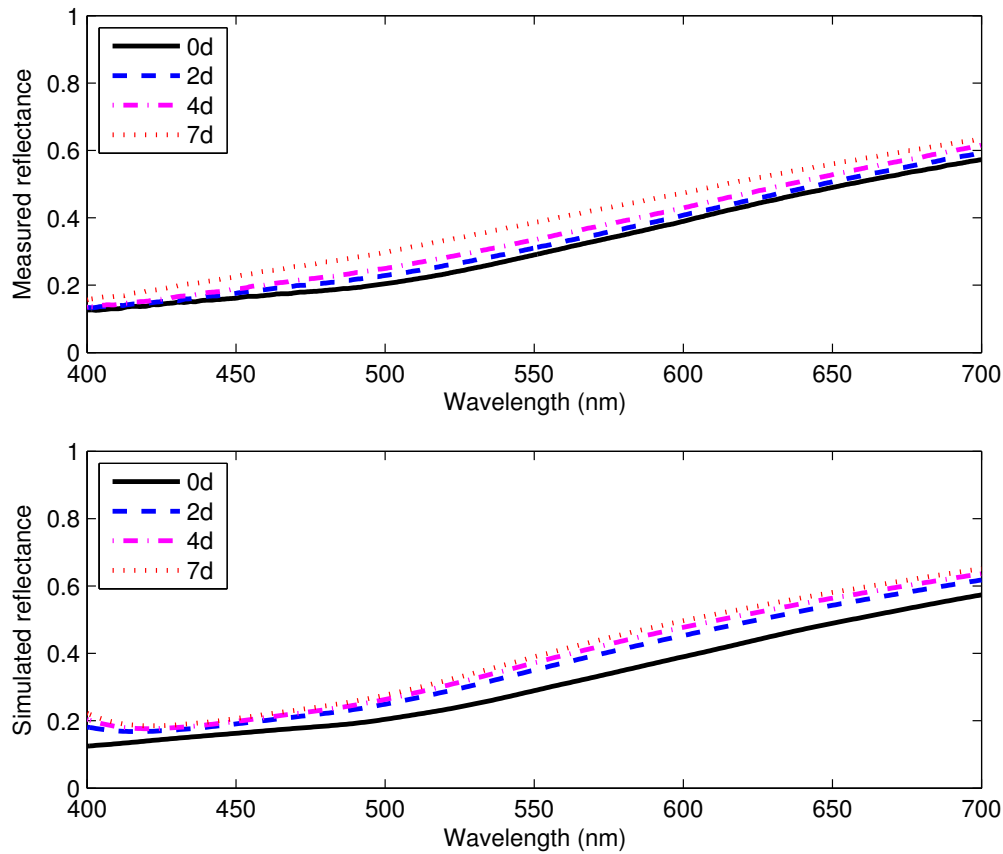
Figure 8.5: Measured and simulated reflectance curves of fading cork initially, after six hours, one day, and seven days. *Top*: Measured progression of reflectance curves. *Bottom*: Simulated progression of reflectance curves.

8.2 Phenomenological Assessment

Figure 8.6 shows the progress of fading under different conditions as simulated by our framework. The top sequence indicates the resulting behavior for a non-scattering medium. In this instance, fading proceeds as a wave of colourant decomposition that progresses downward at a constant rate. This is consistent with prior observations reported in the literature [28]. Conversely, for scattering media, the progression of fading slows over time. This behavior is depicted in the middle row of Figure 8.6, and agrees with the findings of Johnston-Feller [54] in which the depth of fading decreased with increasing TiO_2 content (a tint). Finally, the bottom sequence depicts the fading of a

Material	β (at 400 nm)	λ_{max}
Lignin	1.670×10^{-9}	400 nm
Newsprint[*]	1.002×10^{-8}	700 nm
Cork[*]	2.000×10^{-13}	700 nm
Toluidine Blue O	1.336×10^{-13}	700 nm
Congo Red	1.336×10^{-13}	700 nm

[*] considering constituents other than lignin.

Table 8.1: Fading rates used in the experiments.

From Material	To Material	γ (at 400 nm)	λ_{max}
Lignin	o-Quinone	1.670×10^{-9}	400 nm

Table 8.2: Breakdown rate used in the experiments for newsprint and for cork.

mixture of pigments in which one of them fades faster than the others. Examples of image sequences rendered using this technique are presented in Figure 8.7. The corresponding fading rates for each of the components are indicated in Table 8.4. Fading parameters required to obtain 50% fading over a fixed period of time are provided for selected pigment combinations under several lighting conditions in Table 8.5.

8.3   Rendered Scenes

Figures 8.8-8.11 present images depicting different fading scenarios, before and after extended periods of light exposure. Where artistic effect is the primary motivation, one may employ the monochromatic approach on the individual RGB channels for simplicity. This technique was used in Figures 8.9 and 8.10.

Figure 8.9 shows a typical living room with a fugitive carpet. To determine the mean light

No. of	Time Steps				
Layers	20	40	60	80	100
10	3.66	7.31	10.96	14.62	18.27
100	6.84	13.66	20.49	27.32	34.15
1000	41.38	82.87	124.19	165.51	206.73

Table 8.3: Time required (in seconds) to simulate the effect of light exposure on newsprint using the proposed framework, and considering 371 wavelengths (330-700 nm at 1 nm intervals).

| Row | Pigment | | |
---	Cyan	Magenta	Yellow
1	8.661×10^{-8}	9.735×10^{-8}	1.256×10^{-7}
2	8.661×10^{-8}	4.867×10^{-8}	6.279×10^{-8}
3	4.331×10^{-8}	1.217×10^{-7}	6.279×10^{-8}
4	4.331×10^{-8}	4.867×10^{-8}	2.511×10^{-7}

Table 8.4: Sets of fading rates for the pigments used in the renderings depicted in Figure 8.7. The fading rates are quoted in $m^3 J^{-1}$ at 500 nm.

Pigments	Daylight	Incandescent
Cyan	3.385×10^{-8}	9.128×10^{-6}
Magenta	3.812×10^{-8}	2.354×10^{-5}
Yellow	4.825×10^{-8}	7.753×10^{-5}
Cyan + Magenta	4.817×10^{-8}	2.423×10^{-5}
Cyan + Yellow	4.350×10^{-8}	1.452×10^{-5}
Magenta + Yellow	5.211×10^{-8}	3.393×10^{-5}
Cyan + Magenta + Yellow	6.027×10^{-8}	3.315×10^{-5}

Table 8.5: Fading rates (in $m^3 J^{-1}$ at 500 nm) required to fade selected combinations of pigments by a factor of 50% (measured according to the luminance of the material relative to the luminance of the unpigmented medium) in approximately 56 hours (8 hours per day for 7 days) under daylight (D65 with a peak irradiance of approximately $1.6 \, W \, m^{-2} \, nm^{-1}$) and incandescent (100 W bulb at a distance of 1 m) illumination.
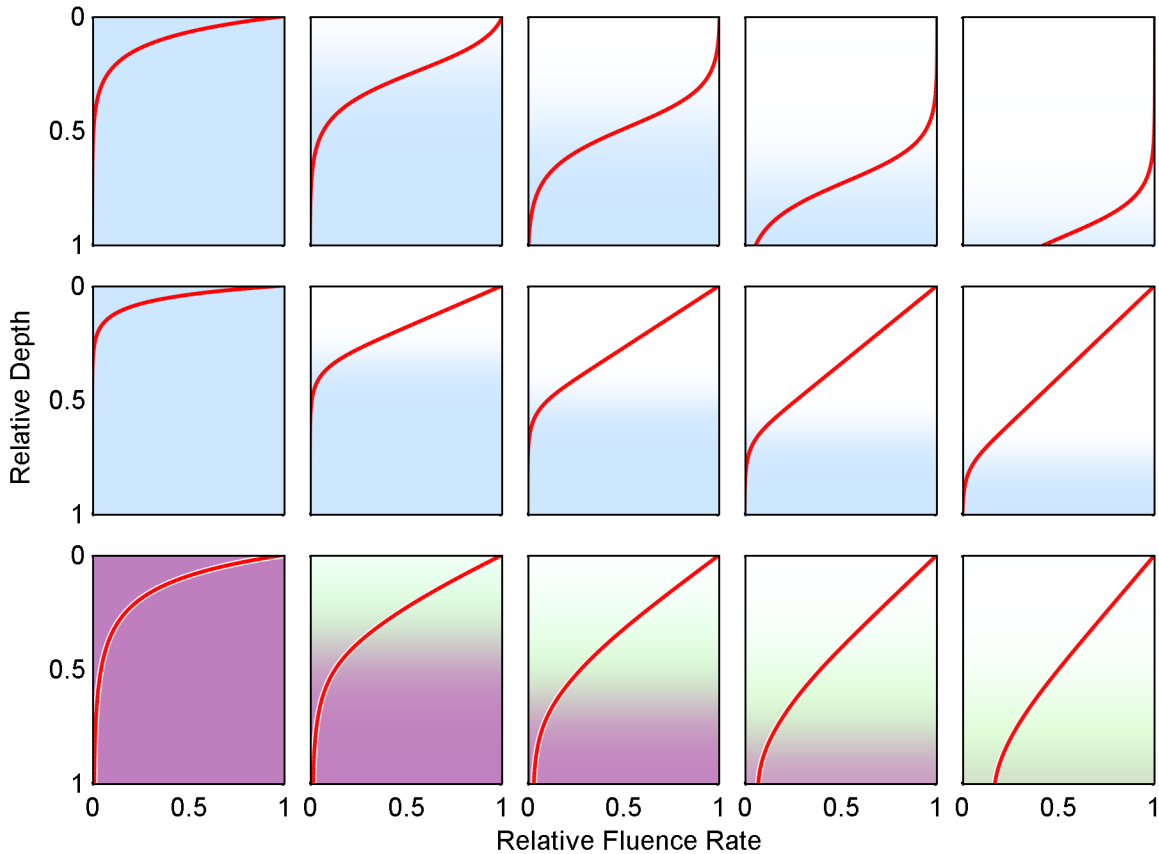
Figure 8.6: Sequences of plots depicting the progression of fading as simulated by the proposed framework. The shading denotes the value of the absorption coefficient relative to its original value. The red line indicates the fluence rate relative to the fluence rate at the surface. *Top Row:* Fading of a non-scattering sample. The colourant is consumed at a constant rate, progressing downward over time. *Middle Row:* Fading of a highly scattering sample. The rate at which the colourant is consumed decreases with time. *Bottom Row:* Fading of a mixture of pigments of varying lightfastness. The hue of the shaded area represents the relative volume fraction of the component colourants with depth.

exposure incident as a function of position, a Monte Carlo renderer (see Section 2.6) was modified to allow the floor surface to function as a camera. The position and orientation of various pieces of furniture were jittered randomly for each sample to account for the fact that these objects would not maintain their locations over a light exposure period of many years. The images in Figure 8.10 show a sunroom with a painting (composed of single colourants) exposed to light from above. The uneven irradiance across the surface of the painting was computed using a standard global

Figure 8.7: Rendering of an image composed of mixtures of cyan, magenta, and yellow pigments is faded according to four hypothetical sets of fading rates for a total exposure of $4.365 \times 10^7 \, \mathrm{J\,m^{-2}}$. The sets of fading rates used are indicated in Table 8.4. *Top Row:* The pigments fade at perceptually similar rates. *Second Row:* The cyan pigment fades more rapidly. *Third Row:* The magenta pigment fades more rapidly. *Bottom Row:* The yellow pigment fades more rapidly.

illumination algorithm. Figure 8.8 depicts a newspaper exposed over an extended period of light exposure ($2.789 \times 10^7 \, \mathrm{J\,m^{-2}}$). The newsprint was folded in quarters during exposure, resulting in an uneven pattern of yellowing. The fading parameters used are given in Tables 8.1 and 8.2.

Figure 8.11 shows a bulletin board. Printed materials have been added and removed from the bulletin board over time. While a printed material is in place, the area of the bulletin board covered by it is shielded from fading effects, resulting in a dark patch whose colour depends on the period of light exposure. The fading parameters used are given in Tables 8.1 and 8.2.

Figure 8.8: Rendering of a newspaper as it turns yellow due to extended light exposure. *Top Left:* Before exposure. *Top Right:* After exposure. *Bottom:* The newspaper has been unfolded.

Figure 8.9: A living room scene in which the carpet has faded over many years of light exposure. Some models used with permission of Turbosquid [93, 95, 94]. *Top Left:* Before exposure. *Top Right:* After exposure. *Bottom:* The furniture has been removed, revealing areas that have been masked from fading.

Figure 8.10: In a sunroom, a painting (composed of single colourants) has its colours altered after an extended period of light exposure. *Top Left:* Before exposure. *Top Right:* After exposure. *Bottom:* Closeup of the painting.
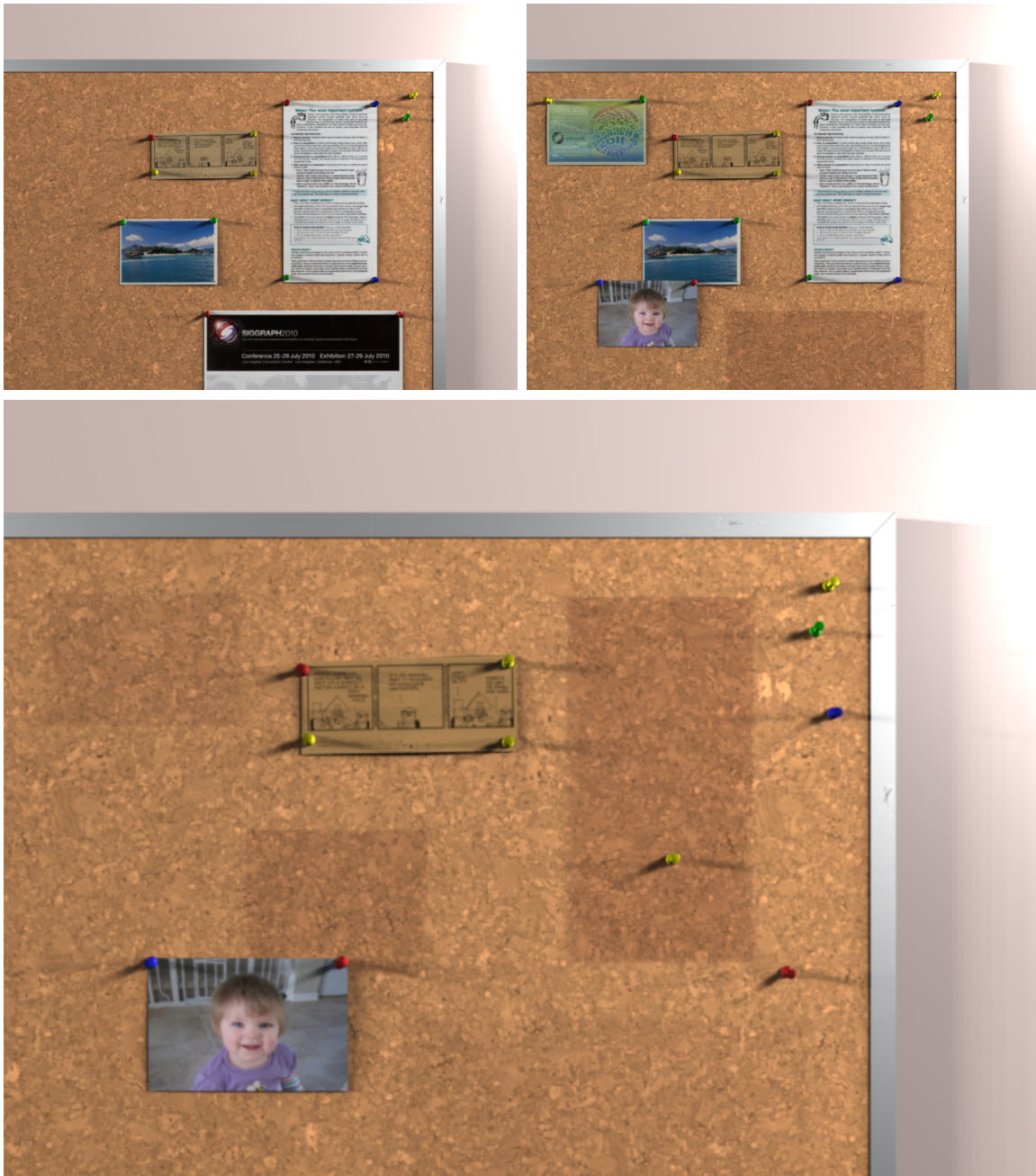
Figure 8.11: A sequence of renderings of a bulletin board in which printed materials have been added and removed over time, leaving an irregular fading pattern on the cork. A comic strip clipped from a newsprint has also yellowed from the prolonged light exposure. Some textures used with permission of Turbosquid [96]. *Top Left:* Before exposure. *Top Right:* After some exposure. The postings have been rearranged as time has passed. *Bottom:* After further exposure. Most of the postings have been removed, revealing the uneven fading pattern.

8.4 Limitations

The proposed framework is directed at simulating the changes in appearance of materials due to extended periods of light exposure. Although exposure to light is arguably one of the primary causes of fading of pigments, other factors, such as heat or humidity, may also influence fading. Our framework as proposed does not account for these effects.

To the best of our knowledge, detailed numerical data regarding the lightfastness of particular colourants is unavailable. Lightfastness data typically consists of a rating on a subjective scale. The rating is obtained by fading the sample under consideration next to a test card consisting of blue wool samples of varying degrees of lightfastness [14]. Moreover, such data is not typically published for commercially available materials. As a result, it was necessary to fit the parameters used in our model using regression techniques [58]. In many fields, regression techniques are used to overcome data scarcity limitations [66, 85, 36]. We remark that although the values assigned for the parameters were selected to highlight appearance features, these parameters have a physical basis. This allows the scope of applications of the proposed framework to be extended to predictive rendering as described by Greenberg *et al.* [32] in their seminal work on predictability.

8.5 Summary

In this chapter, we have presented experimental results evaluating the predictive capability of the proposed framework. We have demonstrated that these techniques can faithfully replicate fading and brightness reversion using several example specimens, including newsprint, cork, and Congo Red and Toluidine Blue O dyes. We provided comparisons between the simulated fading behavior and qualitative accounts drawn from the literature. The framework was also used to estimate the fading rates of various dyes and pigments. These were applied to simulate the progression of example photographs faded over time due to light exposure, as well as demonstrated through several rendered scenes.

Chapter 9

Performance Enhancements

We remark that the focus of this research is to develop a physically-based framework to enable accurate simulations of these processes. In contexts requiring a high degree of interactivity, particularly when simulations of a large number of colourant mixtures is needed, the framework as proposed may not be sufficient to produce results in a timely manner. In this chapter, we provide an analysis of the influence of the key parameters of this framework, in particular the number of layers and time steps, on its performance characteristics. The run-time, and the resulting spectral reflectance and colour characteristics resulting from the simulation obtained while varying these key parameters are compared with the results yielded by a reference simulation employing a large number of layers and time steps. Practical solutions are proposed allowing for the simulation of material appearance changes due to light exposure where higher performance is required.

The remainder of this chapter is organized as follows. In Section 9.1, we discuss the key parameters of the framework and evaluate their influence on the accuracy of the results yielded by light exposure simulations. In Section 9.2, we propose methods to accelerate the simulation process. We provide a brief summary in Section 9.3.

9.1 Influence of Key Parameters

The main parameters that influence the accuracy of the results produced by the layered fading model include the number of layers and the number of time steps. We discuss the impact of these parameters below and analyse their effects on the accuracy and performance of the simulations. This analysis may be used to guide the selection of these key parameters in order to maximize the accuracy of a fading simulation while minimizing the runtime cost.

9.1.1 Number of Layers

Within a layer, the medium is treated as fading uniformly throughout its depth. This is an approximation of actual fading behavior, where fading will be more pronounced on the exposed side of the layer than the unexposed side. The difference between the fluence rate from the top of a layer to the bottom of that layer increases with greater layer thickness or optical density. Hence, the accuracy of the simulation may be improved by increasing the number of layers.

At each time step, the solution to the block tridiagonal system shown in Figure 5.3, whose size is proportional to the number of layers, n, must be found. This may be solved in $O(n)$ time [48], rather than the $O(n^3)$ time that is typically required for a general system of linear equations.

9.1.2 Number of Time Steps

At each time step, the fluence rate is determined for each layer. The fluence rate within each layer is presumed constant during the course of the time step. The accuracy of this approximation is primarily determined by the rate of fading during the time interval. As upper layers fade, the fluence rate increases in the layers below. Thus, the more rapidly fading progresses, the less accurate the approximation is that the fluence rate remains constant. To reduce error introduced by discretization in time, more time steps may be used.

The simulation of each time step only depends on the computation of the fluence rate and absorptive properties throughout the medium at the beginning of the time step and the length of the

Figure 9.1: Optical depth associated with absorption of the three colourants (at full concentration) used in the assessment of the fading simulation parameters.

time interval. As there is no other dependency on prior time steps, the performance is linear with respect to the number of time steps.

9.1.3 Influence Assessment

As stated earlier, the key parameters affecting the behavior of the layered fading model are the number of layers and the number of time steps. The selection of values for these parameters represents a trade-off between run-time performance and minimization of discretization error. To assess the effects of these parameters, fading simulations were performed using samples consisting of random mixtures of three primary colourants: cyan, magenta, yellow. The Kubelka-Munk absorption and scattering coefficients for these colourants were derived from measurements by Yang [104] of optical depth, $\ln(I_0/I)$, at full concentration, which are provided in Figures 9.1 and 9.2, respectively.

Note that, in the case of absorption, the optical depth is commonly expressed as

$$\sigma_a(\lambda) = \ln\left(\frac{\Phi_i(\lambda)}{\Phi_a(\lambda)}\right), \tag{9.1}$$

where Φ_i and Φ_a correspond to the spectral radiant fluxes received and absorbed by the material,
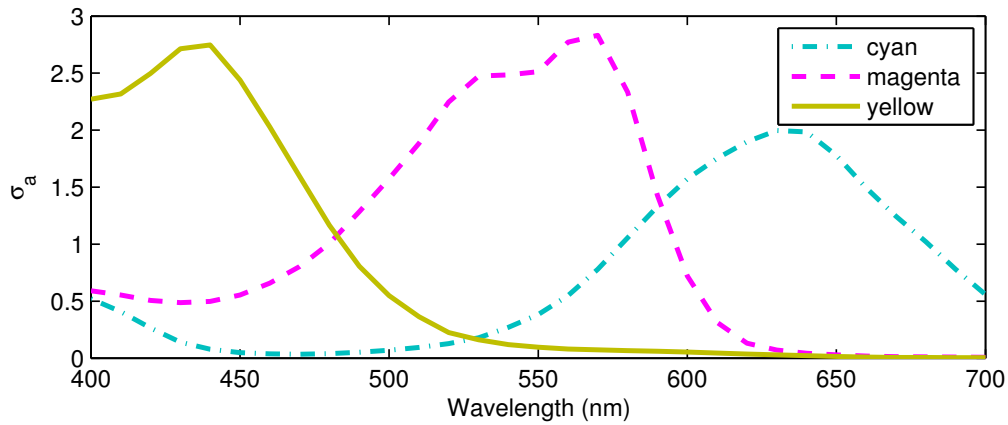
91
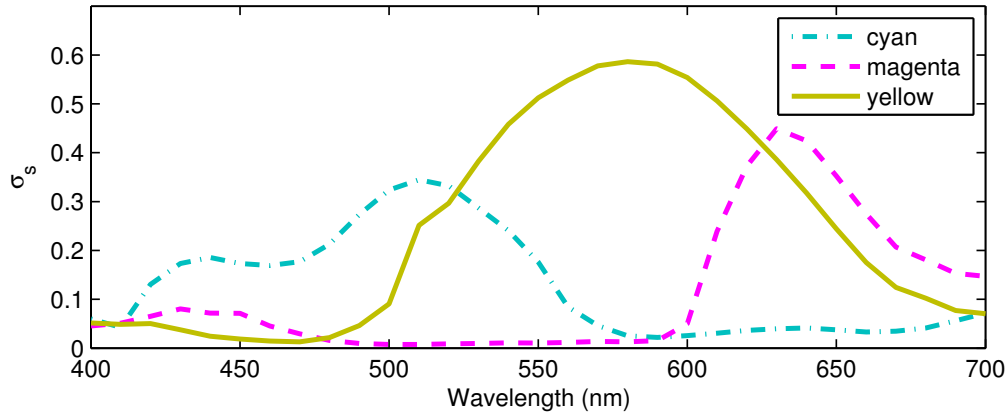
Figure 9.2: Optical depth associated with scattering of the three colourants (at full concentration) used in the assessment of the fading simulation parameters.

respectively. Similarly, in the case of scattering, the optical depth is usually expressed as

$$\sigma_s(\lambda) = \ln\left(\frac{\Phi_i(\lambda)}{\Phi_s(\lambda)}\right), \tag{9.2}$$

where Φ_s represents the spectral radiant flux scattered by the material. The number of layers and time steps were varied and the results compared for colour and spectral accuracy to a reference simulation using 1024 layers and 625 time steps.

To evaluate the spectral accuracy of the model, the reflectance of each sample was compared directly to the reflectance given by the corresponding reference simulation. The root-mean-square (RMS) difference between these two reflectance curves was computed. The maximum RMS difference across all samples is given in Table 9.1 for various combinations of the key parameters.

To evaluate colour accuracy, the reflectance curves generated by the simulation are transformed to the CIE Lab colour space [90]. Table 9.2 shows the maximum ΔE, the Euclidean distance in the CIE Lab colour space (Equation 2.32), between the trial simulation and the corresponding reference simulation. This distance is a measure of the perceptual difference between two colours, with $\Delta E = 1$ representing a *just noticeable difference*. That is, two colours having a difference represented by $\Delta E < 1$ are indistinguishable to a human observer [68].

max	**Time Steps**		
RMS(ΔR)	5	25	125
2	0.0626	0.0352	0.0302
4	0.0371	0.0129	0.0085
8	0.0311	0.0071	0.0027
16	0.0297	0.0058	0.0013
32	0.0293	0.0055	0.0010
64	0.0292	0.0054	0.0009
128	0.0292	0.0054	0.0009

Table 9.1: Spectral difference between the results of fading simulated according to the framework using varying numbers of layers and time steps and a reference simulation using 1024 layers and 625 time steps. Ten random samples were selected and fading was simulated. For each sample, the RMS ΔR was computed. The values indicated are the maximum RMS ΔR over all of the samples.

	Time Steps		
max ΔE	5	25	125
2	6.2203	3.8875	3.4764
4	3.3564	1.2955	0.9543
8	2.7686	**0.6476**	**0.2844**
16	2.6603	**0.5102**	**0.1225**
32	2.6333	**0.4882**	**0.0872**
64	2.6265	**0.4827**	**0.0811**
128	2.6248	**0.4813**	**0.0798**

Table 9.2: Colour difference between the results of fading (simulated according to the framework using varying numbers of layers and time steps) and a reference simulation (using 1024 layers and 625 time steps). The values indicated are the maximum ΔE over ten randomly selected samples. The figures shown in bold represent ΔE less than a just noticeable difference.

Table 9.3 shows the average run-time (across all samples) required to simulate fading. The simulations were performed using a single core on a machine with two 2.8 GHz quad-core Xeon E5462 processors and 16 GB of RAM.

Figure 9.3 depicts renderings of two sequences of photographs demonstrating fading over an extended period of time. These sequences employ the same settings as for the reference simulations, *i.e.*, 1024 layers and 625 time steps. Figure 9.4 provides a visual depiction of the effect of using varying number of layers and time steps.

		Time Steps	
time (*s*)	5	25	125
2	0.6	2.9	14.0
4	0.7	3.2	15.4
8	0.8	3.6	17.6
16	1.0	4.4	21.5
32	1.5	6.3	30.7
64	3.5	15.8	76.6
128	8.6	36.8	179.0

Table 9.3: Time (in *seconds*) required to simulate fading according to the framework using the varying numbers of layers and time steps.

Figure 9.3: Reference renderings of two photographs faded according to the framework using 1024 layers and 625 time steps. The leftmost images depict the initial (unfaded) state of the photographs. The remaining images depict the photograph faded over progressively longer time periods.

9.2 Acceleration

A typical high definition image consists of over two million pixels and may contain hundreds of thousands of unique colours. As such, it is prohibitively expensive to run a simulation for each colour in the image. For typical fading scenarios, there are only a few pigments involved. The colours to be faded consist of varying mixtures of these pigments. For mixtures of *n* pigments, we can divide the *n*-dimensional space into a grid and simulate fading only at grid points. To determine the reflectance of a faded sample consisting of a different mixture of these pigments, we interpolate between grid points. By dividing a three-dimensional colour space (such as CMY) into a coarse grid, we only need to simulate fading for a comparatively small number of pigment combinations. We use a $6 \times 6 \times 6$ grid in our simulations. Fading results may then be computed at interactive rates.
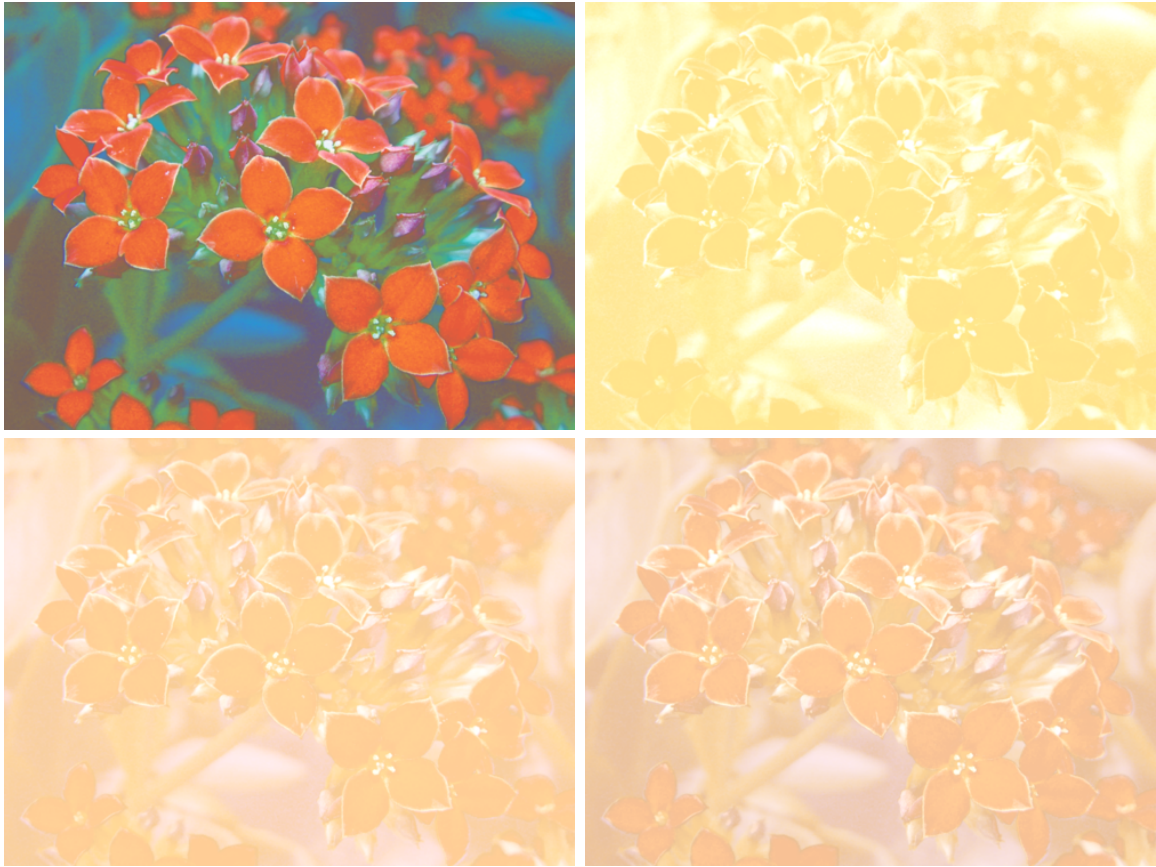
Figure 9.4: Photograph faded using varying numbers of layers and time steps. *Top-Left:* Initial (unfaded) state of the photograph. *Top-Right:* Faded using two layers, five time steps. *Bottom-Left:* Faded using 128 layers, 125 time steps. *Bottom-Right:* Reference rendering, faded using 1024 layers, 625 time steps.

Figure 9.5 shows a comparison of a photograph with fading applied with and without interpolation as described above. The simulation without acceleration required 218.3 hours to complete. In contrast, the $6 \times 6 \times 6$ grid took 6.3 hours to generate, after which multiple images may be generated instantaneously. Figure 9.6 shows renderings of a scene subjected to light exposure over the course of several years. The dresser has faded except where the lamp stood. The rug has faded, and the wood floor has turned yellow except where the rug was placed. These renderings illustrate the use of this framework in realistic image synthesis applications. The rug and the dresser were faded by approximating the initial state (prior to light exposure) as a combination of the primary

Figure 9.5: Rendering of a photograph fading with and without acceleration. *Left:* Original photograph. *Center:* Reference rendering using 1024 layers and 625 time steps. *Right:* Rendering using interpolation over a $6 \times 6 \times 6$ grid.

pigments depicted in Figures 9.1–9.2 and using the same techniques applied to the photographs in Figures 9.3–9.5. The fading of the wood floor was simulated using absorption data for lignin and orthoquinones provided in [60].

9.3 Summary

In this chapter, we have analysed the performance characteristics of the proposed framework. We have developed practical techniques for improving the performance for applications in which a higher degree of interactivity is required.

Figure 9.6: Rendering of a scene in which a dresser, rug, and wood floor are subjected to light exposure over the course of several years. *Top Left:* Prior to light exposure. *Top Right:* After several years of exposure, the rug and dresser have faded and the wood floor has yellowed. *Bottom:* The rug and lamp have been removed, revealing the effects of light exposure on the dresser and on the wood floor.

Chapter 10

Conclusion and Future Work

The appearance of a material is determined by how it scatters and absorbs light. In traditional computer graphics, appearance is considered at a given instant in time. Over extended periods of time, however, light can alter the physicochemical properties of a material, leading to noticeable changes in its appearance. Among these changes, fading is one of the most ubiquitous in real-world settings.

Several advances have been made in recent years toward modeling and rendering of aging and weathering phenomena. Data-driven approaches have been proposed that could be employed to render the appearance progression of faded materials. However, these techniques require appearance attributes at key intervals be supplied as input to the algorithm. To the best of our knowledge, our work [60] is the first in the computer graphics literature to address the predictive simulation of fading and yellowing of materials based on first principles.

10.1 Contributions

In this dissertation, we have presented a novel theoretical framework for the underlying mechanisms responsible for the fading of surface finishes, such as paints and stains, due to light exposure. By introducing time as an integral parameter within the standard rendering equation, this framework

describes the kinetics of fading processes using a robust, yet flexible, physicochemical approach that allows for a wide range of variations in light exposure levels and sample conditions such as thickness and colourant (single or mixture) contents.

The proposed framework provides the foundation for predictive simulations of time-dependent light exposure effects on material appearance, aimed not only to computer graphics applications, but also to conservation and industrial investigations. In this work, these simulations are realized through the development of a layered fading model using the Kubelka-Munk formulation [63]. To evaluate the fidelity of this model, its readings were compared to spectrophotometric measurements obtained from a fading experiment performed during this research. The qualitative agreement between the simulated and measured results indicates that the theoretical treatment given to fading in this dissertation can capture a variety of different fading behaviors.

We have also provided measurements pertaining to the progression of spectral appearance of selected materials over time due to light exposure. Such data is not readily available in the literature. We discussed challenges that arose in preparing the experimental setup required to obtain reliable measurements.

On the application side, the layered fading model introduced in this dissertation can be readily integrated into existing image synthesis pipelines. To solve the system of differential equations describing the effects of light exposure on material appearance over time, we have proposed an efficient numerical strategy that takes advantage of the layered structure of the proposed framework. We note that these procedures have potential applications in a wide range of different fields as outlined in the next section. We have used these techniques to estimate the fading rates of a few selected dyes and pigments. To demonstrate the applicability of this model, we have rendered several typical scenes depicting man-made objects subjected to light exposure during extended periods of time.

10.2   Future Research

It should be noted that the proposed framework is limited to accounting for changes at the site in which light absorption takes place. For instance, the removal of a colourant at the site of absorption may cause adjacent colourant to spread in order to reach an equilibrium. Additionally, in organic materials, the absorption of light may induce reactions that affect the medium at locations other than the site of absorption. In future work, we plan to extend the proposed framework to address these limitations. We also intend to explore its application for simulating changes to other material appearance attributes, such as fluorescence, induced by absorbed radiation. Additionally, we plan to investigate the techniques for inverting the simulation procedures described in this dissertation. This would enable its application in studies aimed at digital restoration of faded artifacts. For example, from spectral images of historical documents [77], along with data describing the spectral absorption and scattering characteristics and lightfastness characteristics of its constituents, one could render an image depicting the document in its original appearance. Further, to increase the accuracy to run-time cost ratio, we intend to modify the underlying model to allow for dynamic, non-uniform layer thicknesses. By using thinner layers where the fluence rate changes more sharply, a higher degree of accuracy may be achieved with fewer layers. Allowing these layer thicknesses to vary from one time-step to another will allow the system to adapt as the colourant distribution evolves. We are confident that the proposed framework sets a firm foundation for these extensions to be built upon.

References

[1] A. Abdul-Rahman and M. Chen. Spectral volume rendering based on the Kubelka-Munk theory. *Computer Graphics Forum*, 24(3):413–422, 2005.

[2] ANSI. Nomenclature and definitions for illuminating engineering. In *ANSI/IES RP-6-1986*. Illuminating Engineering Society of North America, New York, 1986.

[3] J. Arvo. Transfer equations in global illumination. In *SIGGRAPH '93 Course Notes*, volume 42, August 1993.

[4] G.V.G. Baranoski and J.G. Rokne. *Light Interaction with Plants: A Computer Graphics Perspective*. Horwood Publishing, Chichester, UK, 2004.

[5] R.S. Barros and M. Walter. Synthesis of human skin pigmentation disorders. *Computer Graphics Forum*, pages 1–15, June 2016.

[6] F.O. Bartell, E.L. Dereniak, and W.L. Wolfe. The theory and measurement of bidirectional reflectance distribution function (BRDF) and bidirectional transmittance distrubtion function (BTDF). *Proceedings of SPIE Radiation Scattering in Optical Systems*, 257:154–160, 1980.

[7] R.S. Berns. Rejuvenating the appearance of cultural heritage using color and imaging science techniques. In *Proceedings of the 10th Congress of the International Colour Association*, pages 369–374, 2005.

[8] R.S. Berns, S. Byrns, F. Casadio, I. Fiedler, C. Gallagher, F.H. Imai, A. Newman, M. Rosen, and L.A. Taplin. Rejuvenating the appearance of Seurat's *a sunday on la grande jatte – 1884* using color and imaging science techniques - a simulation. In *Proceedings of the 10th Congress of the International Colour Association*, pages 1669–1672, 2005.

[9] C.F. Bohren. *Atmospheric Optics*. Wiley-VCH Verlag GmbH & Co. KGaA, 2007.

[10] C. Bosch, P. Laffont, H. Rushmeier, J. Dorsey, and G. Drettakis. Image-guided weathering: A new approach applied to flow phenomena. *ACM Transactions on Graphics*, 30(3):20:1–13, May 2011.

[11] T.F. Chen. *On the Modelling of Hyperspectral Light and Skin Interactions and the Simulation of Skin Appearance Changes Due to Tanning*. PhD thesis, University of Waterloo, 2015.

[12] T.F. Chen, G.V.G. Baranoski, B.W. Kimmel, and E. Miranda. Hyperspectral modeling of skin appearance. *ACM Transactions on Graphics*, 34(3):31:1–31:14, April 2015.

[13] Y. Chen, L. Xia, T. Wong, X. Tong, H. Bao, B. Guo, and H. Shum. Visual simulation of weathering by γ-ton tracing. *ACM Transactions on Graphics*, 24(3):1127–1133, July 2005.

[14] A. Choudhury. *Textile Preparation and Dyeing*. Science Publishers, Enfield, NH, 2006.

[15] R. Cook and K.E. Torrance. A reflectance model for computer graphics. *Computer Graphics (SIGGRAPH Proceedings)*, 15(3):301–316, July 1981.

[16] C.J. Curtis, S.E. Anderson, J.E. Seims, K.W. Fleischer, and D.H. Salesin. Computer-generated watercolor. In *Computer Graphics Proceedings, Annual Conference Series*, pages 421–430, 1997.

[17] D. Deirmendjian. Scattering and polarization properties of water clouds and hazes in the visible and infrared. *Applied Optics*, 3(2):187–196, 1964.

[18] M. Doi and S. Tominaga. Spectral estimation of human skin color using the Kubelka-Munk theory. In *Proceedings of SPIE*, volume 5008, pages 221–228, January 2003.

[19] J. Dorsey and P. Hanrahan. Modeling and rendering of metallic patinas. In *Computer Graphics Proceedings, Annual Conference Series*, pages 387–396, 1996.

[20] J. Dorsey, H.K. Pedersen, and P. Hanrahan. Flow and changes in appearance. In *Computer Graphics Proceedings, Annual Conference Series*, pages 411–420, 1996.

[21] J. Dorsey, H. Rushmeier, and F. Sillion. *Digital Modeling of Material Appearance*. Morgan Kaufmann/Elsevier, 2008.

[22] P. Dutré, K. Bala, and P. Bekaert. *Advanced Global Illumination*. Taylor and Francis Group, Boca Raton, FL, 2006.

[23] P.A. Farrant. *Color in Nature: A Visual and Scientific Exploration*. Blandford Press, London, 1999.

[24] R.P. Feynman. *QED: The Strange Theory of Light and Matter*. Princeton University Press, Princeton, NJ, 1985.

[25] R.P. Feynman, R.B. Leighton, and M. Sands. *The Feynman Lectures on Physics*, volume 1. Addison-Wesley Publishing Company, Reading, MA, 1964.

[26] A. Fournier. From local to global illumination and back. In *Proceedings of the 6th Eurographics Workshop on Rendering*, pages 127–136, 1995.

[27] C.H. Giles. The fading of colouring matters. *Journal of Applied Chemistry*, 15:541–550, December 1965.

[28] C.H. Giles, D.P. Johari, and C.D. Shah. Some observations on the kinetics of dye fading. *Textile Research Journal*, 38(10):1048–1056, October 1968.

[29] C.H. Giles and R.B. McKay. The lightfastness of dyes: A review. *Textile Research Journal*, 33(7):528–575, July 1963.

[30] R.E. Glading. *The Ultraviolet Absorption Spectra of Lignin and Related Compounds*. PhD thesis, The Institute of Paper Chemistry, Lawrence College, Appleton, WI, June 1940.

[31] C. Goral, K.E. Torrance, D.P. Greenberg, and B. Battaile. Modeling the interaction of light between diffuse surfaces. *Computer Graphics*, 18(3):213–222, July 1984.

[32] D.P. Greenberg, J. Arvo, E. Lafortune, K.E. Torrance, J.A. Ferwerda, B. Walter, B. Trumbore, P. Shirley, S. Pattanaik, and S. Foo. A framework for realistic image synthesis. In *Computer Graphics Proceedings, Annual Conference Series*, pages 477–494, August 1997.

[33] C.M. Grinstead and J.L. Snell. *Introduction to Probability*. American Mathematical Society, Providence, RI, 2nd edition, 2012.

[34] Jinwei Gu, Chien-I Tu, Ravi Ramamoorthi, Peter Belhumeur, Wojciech Matusik, and Shree Nayar. Time-varying surface appearance: acquisition, modeling and rendering. *ACM Transactions on Graphics*, 25(3):762–771, July 2006.

[35] C.S. Haase and G.W. Meyer. Modeling pigmented materials for realistic image synthesis. *ACM Transactions on Graphics*, 11(4):305–335, October 1992.

[36] L. Hallik, O. Kull, T. Nilson, and J. Peñuelas. Spectral reflectance of multispecies herbaceous and moss canopies in the boreal forest understory and open field. *Canadian Journal of Remote Sensing*, 35(5):474–485, 2009.

[37] J.M. Hammersley and D.C. Handscomb. *Monte Carlo Methods*. Methuen & Co., Ltd., London, England, 1967.

[38] P. Hanrahan and W. Krueger. Reflection from layered surfaces due to subsurface scattering. In *Computer Graphics (SIGGRAPH Proceedings)*, volume 27, pages 165–174, August 1993.

[39] M. Hašan, M. Fuchs, W. Matusik, H. Pfister, and S. Rusinkiewicz. Physical reproduction of materials with specified subsurface scattering. *ACM Transactions on Graphics*, 29(4):61:1–10, July 2010.

[40] X.D. He, K.E. Torrance, F.X. Sillion, and D.P. Greenberg. A comprehensive physical model for light reflection. *Computer Graphics*, 25(4):175–186, July 1991.

[41] J. Hecht. Light repairs art: optical overlays restore faded masterworks. *Optics & Photonics News*, 26(4):40–47, April 2015.

[42] C. Heitner. Light-induced yellowing of wood-containing papers. In C. Heitner and J.C. Scaiano, editors, *Photochemistry and Lignocellulosic Materials*, volume 531 of *ACS Symposium Series*, chapter 1, pages 2–25. American Chemical Society, Washington, DC, 1993.

[43] B.K.P. Horn and R.W. Sjoberg. Calculating the reflectance map. *Applied Optics*, 18(11):1770–1779, June 1979.

[44] K. Hunger and G. Wilker. *Industrial organic pigments: production, properties and applications*. Wiley-VCH, Weinheim, Germany, third edition, 2004.

[45] R. Hunter and R. Harold. *The Measurement of Appearance*. John Wiley and Sons, New York, NY, 2nd edition, 1987.

[46] J.A. Iglesias-Guitian, C. Aliaga, A. Jarabo, and D. Gutierrez. A biophysically-based model of the optical properties of skin aging. *Computer Graphics Forum*, 34(2):45–55, May 2015.

[47] F.H. Imai, M.R. Rosen, and R.S. Berns. Multi-spectral imaging of a Van Gogh's self-portrait at the National Gallery of Art, Washington, D.C. In *Proceedings of the IS&T PICS Conference*, pages 185–189, Springfield, VA, 2001. IS&T.

[48] E. Isaacson and H.B. Keller. *Analysis of Numerical Methods*. Dover Publications, Inc., Mineola, NY, 1994.

[49] S.H. James and W.G. Eckert. *Interpretation of Bloodstain Evidence at Crime Scenes*. CRC Press LLC, Boca Raton, FL, 2nd edition, 1998.

[50] H.W. Jensen. Global illumination using photon maps. In *Proceedings of the Eurographics Workshop on Rendering Techniques*, pages 21–30, December 1996.

[51] H.W. Jensen. *Realistic Image Synthesis using Photon Mapping*. AK Peters, Natick, MA, July 2001.

[52] R. Johnston-Feller. *Color Science in the Examination of Museum Objects: Nondesctructive Procedures*. Tools for Conservation Series. The Getty Conservation Institute, Los Angeles, CA, 2001.

[53] R. Johnston-Feller, R.L. Feller, C.W. Bailie, and M. Curran. The kinetics of fading: Opaque paint films pigmented with alizarin lake and titanium dioxide. *Journal of the American Institute for Conservation*, 23(2):114–129, 1984.

[54] R.M. Johnston-Feller. Reflections on the phenomenon of fading. *Journal of Coatings Technology*, 58(736):33–50, May 1986.

[55] D.B. Judd and G. Wyszecki. *Color in Business, Science and Industry*. John Wiley & Sons, New York, third edition, 1975.

[56] J.T. Kajiya. The rendering equation. In *Computer Graphics (SIGGRAPH Proceedings)*, volume 20, pages 143–150, August 1986.

[57] C. Kelemen, L. Szirmay-Kalos, G. Antal, and F. Csonka. A simple and robust mutation strategy for the metropolis light transport algorithm. *Computer Graphics Forum*, 21(3):531–540, September 2002.

[58] J.F. Kenney and E.S. Keeping. *Mathematics of Statistics*. Van Nostrand, Princeton, NJ, 3rd edition, 1962.

[59] J.T. Kider, S. Raja, and N.I. Badler. Fruit senescence and decay simulation. *Computer Graphics Forum*, 30(2):257–266, April 2011. Proceedings of EUROGRAPHICS 2011.

[60] B. Kimmel, G.V.G. Baranoski, T.F. Chen, D. Yim, and E. Miranda. Spectral appearance changes induced by light exposure. *ACM Transactions on Graphics*, 32(1):10:1–10:13, January 2013.

[61] B.W. Kimmel and G.V.G. Baranoski. Practical acceleration strategies for the predictive visualization of fading phenomena. In *Proceedings of the 29th International Conference on Computer Animation and Social Agents*, pages 45–52, Geneva, Switzerland, May 2016.

[62] P. Kubelka. New contributions to the optics of intensly light-scattering materials. Part I. *Journal of the Optical Society of America*, 38(5):448–457, May 1948.

[63] P. Kubelka and F. Munk. Ein beitrag zur optik der farbanstriche (An article on optics of paint layers). *Zeitschrift für Technische Physik*, 12:593–601, August 1931.

[64] E. Lafortune. *Mathematical Models and Monte Carlo Algorithms for Physically Based Rendering*. PhD thesis, Katholieke Universiteit Leuven, February 1996.

[65] J.R. Lakowicz. *Principles of Fluorescence Spectroscopy*. Springer Science+Business Media, LLC, Singapore, 3rd edition, 2006.

[66] D. Lazár and G. Schansker. *Models of Chlorophyll a Fluorescence Transients*, volume 29 of *Advances in Photosynthesis and Respiration*, pages 85–123. Springer Science+Business Media B.V., Dordrecht, The Netherlands, 2009.

[67] T.J.S. Learner, P. Smithen, J.W. Krueger, and M.R. Schilling, editors. *Modern Paints Uncovered*. Getty Publications, Los Angeles, CA, 2008.

[68] D.L. MacAdam. Visual sensitivities to color differences in daylight. *Journal of the Optical Society of America*, 32(5):247–274, 1942.

[69] A. D. McNaught and A. Wilkinson. *Compendium of Chemical Terminology*. Blackwell Science, Oxford, UK, 2nd edition, 1997.

[70] S. Mérillou and D. Ghazanfarpour. A survey of aging and weathering phenomena in computer graphics. *Computers & Graphics*, 32(2):159–174, April 2008.

[71] J.R. Meyer-Arendt. *Introduction to Modern and Classical Optics*. Prentice-Hall, New Jersey, 1984.

[72] H.R. Morris and P.M. Whitmore. "Virtual fading" of art objects: Simulating the future fading of artifacts by visualizing micro-fading test results. *Journal of the American Institute for Conservation*, 46:215–228, January 2007.

[73] T.H. Morton. The practical assessment of the light fastness of dyeings. *Journal of the Society of Dyers and Colourists*, 62(12):597–605, December 1949.

[74] F.E. Nicodemus, J.C. Richmond, J.J. Hsia, I.W. Ginsberg, and T. Limperis. *Geometrical Considerations and Nomenclature for Reflectance*. National Bureau of Standards, United States Department of Commerce, 1977.

[75] J.R. Norris. *Markov Chains*. Cambridge University Press, 1997.

[76] M. Oren and S.K. Nayar. Generalization of Lambert's reflectance model. In *Computer Graphics Proceedings, Annual Conference Series*, pages 239–246, 1994.

[77] R. Padoan, Th.A.G. Steemers, M.E. Klein, B.J. Aalderink, and G. de Bruin. Quantitative hyperspectral imaging of historical documents: Technique and applications. In *9th International Conference on NDT of Art*, pages 1–10, Jerusalem, Israel, May 2008.

[78] F.L. Pedrotti and L.S. Pedrotti. *Introduction to Optics*. Prentice Hall, Upper Saddle River, NJ, 2nd edition, 1993.

[79] H. Pereira. *Cork: Biology, Production and Uses*. Elsevier, Amsterdam, The Netherlands, 1st edition, 2007.

[80] A.D. Polyanin and V.F. Zaitsev. *Handbook of Nonlinear Partial Differential Equations*. Chapman & Hall/CRC, Boca Raton, FL, 2004.

[81] J.C. Roberts. *The Chemistry of Paper*. The Royal Society of Chemistry, Cambridge, UK, 1996.

[82] D. Rudolf, D. Mould, and E. Neufeld. Simulating wax crayons. In *Proceedings of the Pacific Conference on Computer Graphics and Applications*, pages 163–172, October 2003.

[83] J.L. Saunderson. Calculation of the color of pigmented plastics. *Journal of the Optical Society of America*, 32(12):727–729, 1942.

[84] M. Seyfried and L. Fukshansky. Light gradients in plant tissue. *Applied Optics*, 22(9):1402–1408, May 1983.

[85] T. Shi and C.A. DiMarzio. Multispectral method for skin imaging: development and validation. *Applied Optics*, 46(36):8619–8626, December 2007.

[86] X. Shi and D. Lu. Colorimetric and chemical modeling based aging simulation of Dunhuang murals. In *The Fifth International Conference on Computer and Information Technology*, pages 570–574, September 2005.

[87] X. Shi, D. Lu, and J. Liu. Color changing and fading simulation for frescoes based on empirical knowledge from artists. In *Advances in Multimedia Information Processing - PCM 2006*, volume 4261 of *Lecture Notes in Computer Science*, pages 861–869. Springer Berlin / Heidelberg, 2006.

[88] P.N. Shivakumar and K.H. Chew. A sufficient condition for nonvanishing of determinants. In *Proceedings of the American Mathematical Society*, volume 43, pages 63–66, March 1974.

[89] T. Smith and J. Guild. The C.I.E. colorimetric standards and their use. *Transactions of the Optical Society*, 33(3):73–134, 1931.

[90] M.C. Stone. *A Field Guide to Digital Color*. A K Peters, Natick, MA, 2003.

[91] G. Thomson. *The Museum Environment*. Butterworth-Heinemann, Oxford, U.K., second edition, 2002.

[92] K.E. Torrance and E.M. Sparrow. Theory of off-specular reflection from roughened surfaces. *Journal of the Optical Society of America*, 57(9):1105–1114, September 1967.

[93] Turbosquid (User: Fworx). Blinds. `http://www.turbosquid.com/3d-models/free-blinds-3d-model/243419`, October 2004.

[94] Turbosquid (User: Res_Com_3D). End table. `http://www.turbosquid.com/3d-models/end-table-3ds-free/451642`, March 2009.

[95] Turbosquid (User: Scorchedmedia). Couch. `http://www.turbosquid.com/3d-models/couch-chaise-3ds-free/368829`, September 2007.

[96] Turbosquid (User: TripRay company). Cork a-017. `http://www.turbosquid.com/FullPreview/Index.cfm/ID/463083`, May 2009.

[97] E. Veach. *Robust Monte Carlo Methods for Light Transport Simulation*. PhD thesis, Stanford University, December 1997.

[98] E. Veach and L.J. Guibas. Metropolis light transport. In *Proceedings of SIGGRAPH 1997*, pages 65–76. Association for Computing Machinery, August 1997.

[99] Jiaping Wang, Xin Tong, Stephen Lin, Minghao Pan, Chao Wang, Hujun Bao, Baining Guo, and Heung-Yeung Shum. Appearance manifolds for modeling time-variant appearance of materials. *ACM Transactions on Graphics*, 25(3):754–761, July 2006.

[100] G.J. Ward. Measuring and modeling anisotropic reflection. *Computer Graphics (SIGGRAPH Proceedings)*, 26(2):265–272, July 1992.

[101] P.M. Whitmore and C. Bailie. Further studies on transparent glaze fading: Chemical and appearance kinetics. *Journal of the American Institute for Conservation*, 36(3):207–230, 1997.

[102] P.M. Whitmore, X. Pan, and C. Bailie. Predicting the fading of objects: Identification of fugitive colorants through direct nondestructive lightfastness measurements. *Journal of the American Institute for Conservation*, 38(3):395–409, 1999.

[103] S. Xue, J. Dorsey, and H. Rushmeier. Stone weathering in a photograph. In R. Ramamoorthi and E. Reinhard, editors, *Eurographics Symposium on Rendering*, pages 1189–1196, June 2011.

[104] L. Yang. Modelling ink-jet printing: Does the Kubelka-Munk theory apply? In *International Conference on Digital Printing Technologies*, volume 18, pages 482–485. Society for Imaging Science and Technology, September 2002.

[105] L. Yang. Characterization of inks and ink application for ink-jet printing: Model and simulation. *Journal of the Optical Society of America A (Optics, Image Science, and Vision)*, 20(7):1149–1154, July 2003.

[106] E.F. Zalewski. Radiometry and photometry. In M. Bass, E.W. Van Stryland, D.R. Williams, and W.L. Wolfe, editors, *Handbook of Optics*, volume 2, chapter 24. McGraw-Hill, 2nd edition, 1995.

APPENDICES

Appendix A

Computing the Kubelka-Munk Parameters from Reflectance Measurements

To compute the Kubelka-Munk (K-M) absorption and scattering coefficients, we use a procedure based on techniques described by Johnston-Feller [52]. First, we measure the reflectance of a layer of known thickness over a black substrate with reflectance ρ_b and over a white reflectance standard, such as spectralon (which we assume to have unit reflectance). Let ρ_0 and ρ_1 denote these reflectance measurements, respectively. According to K-M theory [62], the reflectance of a layer of finite thickness is given by

$$\rho = \frac{1 - \rho_g(a - b\coth b\mu^s Z)}{a + b\coth b\mu^s Z - \rho_g},\tag{A.1}$$

where ρ_g is the reflectance of the substrate, Z is the thickness of the layer, and

$$a = \frac{\mu^a + \mu^s}{\mu^a},\tag{A.2}$$

$$b = \sqrt{a^2 - 1}.\tag{A.3}$$

To simplify Equation A.1, we define

$$x_1 = a - b \coth b\mu^s Z, \tag{A.4}$$

$$x_2 = a + b \coth b\mu^s Z. \tag{A.5}$$

Note that

$$a = \frac{x_1 + x_2}{2}. \tag{A.6}$$

This reduces Equation A.1 to

$$\rho = \frac{1 - x_1 \rho_g}{x_2 - \rho_g}. \tag{A.7}$$

From our reflectance measurements, we have

$$\rho_0 = \frac{1 - x_1 \rho_b}{x_2 - \rho_b}, \tag{A.8}$$

$$\rho_1 = \frac{1 - x_1}{x_2 - 1}. \tag{A.9}$$

The unknowns x_1 and x_2 may be determined by solving

$$\begin{pmatrix} \rho_b & \rho_0 \\ 1 & \rho_1 \end{pmatrix} \begin{pmatrix} x_1 \\ x_2 \end{pmatrix} = \begin{pmatrix} 1 + \rho_0 \rho_b \\ 1 + \rho_1 \end{pmatrix}. \tag{A.10}$$

Now a and b may be computed using Equations A.6 and A.3, respectively. The scattering and absorption coefficients may then be derived from Equations A.5 and A.2, respectively, and are given by

$$\mu^s = \frac{1}{bZ} \coth^{-1} \frac{x_2 - a}{b}, \tag{A.11}$$

$$\mu^a = (a - 1)\mu^s. \tag{A.12}$$

Appendix B

Spectral Data Used in the Simulations

The following spectral data was employed in the simulations performed in this work. This includes absorption and scattering data for various pigments and dyes, and emission spectra for light sources used. Unless otherwise indicated in the table captions, the data were derived from experiments performed during this research as described in Chapter 6.

Wavelength (nm)	Absorption $(L\,g^{-1}\,cm^{-1})$	Wavelength (nm)	Absorption $(L\,g^{-1}\,cm^{-1})$	Wavelength (nm)	Absorption $(L\,g^{-1}\,cm^{-1})$
225	1.3152e+02	315	1.8311e+01	405	8.2028e-01
230	1.1041e+02	320	1.6904e+01	410	6.8661e-01
235	9.1280e+01	325	1.5697e+01	415	5.9429e-01
240	7.4273e+01	330	1.4489e+01	420	5.2481e-01
245	5.7318e+01	335	1.3366e+01	425	4.6774e-01
250	4.3326e+01	340	1.2204e+01	430	4.2267e-01
255	3.3979e+01	345	1.1052e+01	435	3.8802e-01
260	2.9242e+01	350	9.8156e+00	440	3.5817e-01
265	3.0752e+01	355	8.5938e+00	445	3.3444e-01
270	3.5271e+01	360	7.3932e+00	450	3.1517e-01
275	3.9084e+01	365	6.2323e+00	455	2.9769e-01
280	4.0738e+01	370	5.1612e+00	460	2.8314e-01
285	3.9444e+01	375	4.1135e+00		
290	3.5481e+01	380	3.2112e+00		
295	3.0580e+01	385	2.4106e+00		
300	2.5982e+01	390	1.7643e+00		
305	2.2584e+01	395	1.3124e+00		

Table B.1: Specific absorption coefficient of lignin [30].

Wavelength (nm)	Absorption (cm^{-1})	Wavelength (nm)	Absorption (cm^{-1})	Wavelength (nm)	Absorption (cm^{-1})
355	6.5879e+01	475	1.0785e+03	595	1.7903e+02
360	2.1967e+02	480	1.0148e+03	600	1.6684e+02
365	2.9891e+02	485	9.6785e+02	605	1.5695e+02
370	2.3971e+02	490	9.2281e+02	610	1.4858e+02
375	4.5477e+02	495	8.5832e+02	615	1.4136e+02
380	4.1061e+02	500	7.9869e+02	620	1.3521e+02
385	6.0636e+02	505	7.4433e+02	625	1.2935e+02
390	6.6150e+02	510	7.0052e+02	630	1.2424e+02
395	8.5843e+02	515	6.5113e+02	635	1.1764e+02
400	1.1846e+03	520	5.9556e+02	640	1.1052e+02
405	1.3421e+03	525	5.5680e+02	645	1.0327e+02
410	1.3667e+03	530	5.0992e+02	650	9.7928e+01
415	1.6639e+03	535	4.7094e+02	655	9.1506e+01
420	1.5560e+03	540	4.3006e+02	660	8.6629e+01
425	1.6069e+03	545	4.0026e+02	665	8.1920e+01
430	1.5702e+03	550	3.6526e+02	670	7.7847e+01
435	1.5313e+03	555	3.3901e+02	675	7.3352e+01
440	1.6042e+03	560	3.0948e+02	680	6.9351e+01
445	1.4238e+03	565	2.8468e+02	685	6.6193e+01
450	1.3924e+03	570	2.6664e+02	690	6.2417e+01
455	1.3115e+03	575	2.4666e+02	695	5.9857e+01
460	1.2444e+03	580	2.2670e+02	700	5.6373e+01
465	1.1741e+03	585	2.0916e+02		

Table B.2: Absorption coefficient of orthoquinone.

Wavelength (nm)	Irradiance (cm^{-1})	Wavelength (nm)	Irradiance (cm^{-1})	Wavelength (nm)	Irradiance (cm^{-1})
355	1.4350e-01	475	3.0775e+00	595	2.8308e+00
360	1.6487e-01	480	3.0589e+00	600	2.9462e+00
365	2.8244e+00	485	6.1925e+00	605	2.0093e+00
370	2.7584e-01	490	6.1085e+00	610	2.2440e+01
375	1.7646e-01	495	4.2127e+00	615	1.1192e+01
380	2.4678e-01	500	2.9490e+00	620	4.5392e+00
385	2.0522e-01	505	2.5389e+00	625	5.1325e+00
390	1.9577e-01	510	2.7704e+00	630	5.5878e+00
395	2.3889e-01	515	2.8453e+00	635	1.2063e+00
400	4.2125e-01	520	2.5331e+00	640	7.9769e-01
405	1.1398e+01	525	2.1857e+00	645	8.3485e-01
410	1.4252e+00	530	1.9803e+00	650	1.7507e+00
415	1.4085e+00	535	2.6604e+00	655	9.8122e-01
420	1.9454e+00	540	1.5493e+01	660	7.9077e-01
425	2.6222e+00	545	2.3354e+01	665	7.2646e-01
430	3.3960e+00	550	1.1468e+01	670	6.1857e-01
435	2.1347e+01	555	2.8898e+00	675	5.3416e-01
440	4.9354e+00	560	1.3010e+00	680	6.5250e-01
445	4.5584e+00	565	8.6424e-01	685	6.8965e-01
450	4.5940e+00	570	6.6989e-01	690	6.6021e-01
455	4.4798e+00	575	2.1163e+00	695	5.3861e-01
460	4.1952e+00	580	5.3802e+00	700	2.6612e-01
465	3.8420e+00	585	5.7650e+00		

Table B.3: Irradiance of fluorescent lamp.

Wavelength (nm)	Absorption (cm^{-1})	Scattering (cm^{-1})	Wavelength (nm)	Absorption (cm^{-1})	Scattering (cm^{-1})
410	4.0694e-01	4.2533e-02	570	7.7950e-01	4.6079e-02
420	2.6498e-01	1.3046e-01	580	1.0562e+00	2.5450e-02
430	1.4023e-01	1.7327e-01	590	1.3293e+00	2.2081e-02
440	7.7600e-02	1.8568e-01	600	1.5726e+00	2.5800e-02
450	4.9244e-02	1.7311e-01	610	1.7527e+00	3.0485e-02
460	3.8121e-02	1.6914e-01	620	1.8978e+00	3.6283e-02
470	3.5056e-02	1.7676e-01	630	1.9968e+00	3.9482e-02
480	4.0021e-02	2.1276e-01	640	1.9836e+00	4.1340e-02
490	5.1992e-02	2.7341e-01	650	1.7792e+00	3.7530e-02
500	6.9069e-02	3.2351e-01	660	1.4927e+00	3.2888e-02
510	9.3470e-02	3.4451e-01	670	1.2454e+00	3.4628e-02
520	1.2826e-01	3.3243e-01	680	1.0208e+00	4.1333e-02
530	1.7817e-01	2.8670e-01	690	7.8013e-01	5.6279e-02
540	2.6972e-01	2.4078e-01	700	5.5836e-01	7.1760e-02
550	3.8328e-01	1.7622e-01			

Table B.4: Absorption and scattering coefficients of cyan pigment [104].

Wavelength (nm)	Absorption (cm^{-1})	Scattering (cm^{-1})	Wavelength (nm)	Absorption (cm^{-1})	Scattering (cm^{-1})
410	5.5363e-01	5.1229e-02	570	2.8309e+00	1.3623e-02
420	5.0631e-01	6.5070e-02	580	2.3338e+00	1.2997e-02
430	4.8738e-01	8.0534e-02	590	1.4297e+00	1.5387e-02
440	4.9685e-01	7.1836e-02	600	7.2082e-01	5.0025e-02
450	5.5363e-01	7.1151e-02	610	3.1514e-01	2.3907e-01
460	6.5773e-01	4.5555e-02	620	1.3063e-01	3.7314e-01
470	8.0473e-01	2.9332e-02	630	7.0972e-02	4.4895e-01
480	1.0076e+00	1.6009e-02	640	4.3462e-02	4.2438e-01
490	1.2852e+00	9.5168e-03	650	2.8556e-02	3.5230e-01
500	1.5741e+00	7.5707e-03	660	1.9255e-02	2.7470e-01
510	1.8836e+00	7.6787e-03	670	1.3526e-02	2.0708e-01
520	2.2467e+00	8.7527e-03	680	1.1196e-02	1.8081e-01
530	2.4748e+00	9.8367e-03	690	9.1630e-03	1.5324e-01
540	2.4842e+00	1.0842e-02	700	8.4276e-03	1.4676e-01
550	2.5126e+00	1.0568e-02			

Table B.5: Absorption and scattering coefficients of magenta pigment [104].

Wavelength (nm)	Absorption (cm^{-1})	Scattering (cm^{-1})	Wavelength (nm)	Absorption (cm^{-1})	Scattering (cm^{-1})
410	2.3180e+00	4.8748e-02	570	7.2296e-02	5.7754e-01
420	2.4972e+00	5.0175e-02	580	6.6235e-02	5.8622e-01
430	2.7142e+00	3.7553e-02	590	6.0697e-02	5.8127e-01
440	2.7470e+00	2.4510e-02	600	5.3831e-02	5.5378e-01
450	2.4385e+00	1.8783e-02	610	4.5184e-02	5.0611e-01
460	2.0281e+00	1.4391e-02	620	3.5940e-02	4.4870e-01
470	1.5940e+00	1.3073e-02	630	2.8280e-02	3.8562e-01
480	1.1647e+00	2.1740e-02	640	2.1195e-02	3.1768e-01
490	8.0631e-01	4.6170e-02	650	1.5110e-02	2.4446e-01
500	5.4890e-01	9.0699e-02	660	1.0121e-02	1.7530e-01
510	3.6435e-01	2.5128e-01	670	6.8509e-03	1.2438e-01
520	2.2426e-01	2.9643e-01	680	5.4778e-03	1.0200e-01
530	1.6085e-01	3.8303e-01	690	4.1366e-03	7.7027e-02
540	1.1899e-01	4.5795e-01	700	3.6314e-03	7.0541e-02
550	9.6393e-02	5.1243e-01			

Table B.6: Absorption and scattering coefficients of yellow pigment [104].

Index